FILM COOLING, HEAT TRANSFER AND AERODYNAMIC MEASUREMENTS IN A THREE STAGE RESEARCH GAS TURBINE

A Dissertation

by

ARUN SURYANARAYANAN

Submitted to the Office of Graduate Studies of
Texas A&M University
in partial fulfillment of the requirements for the degree of

DOCTOR OF PHILOSOPHY

May 2009

Major Subject: Mechanical Engineering

FILM COOLING, HEAT TRANSFER AND AERODYNAMIC MEASUREMENTS IN A THREE STAGE RESEARCH GAS TURBINE

A Dissertation

by

ARUN SURYANARAYANAN

Submitted to the Office of Graduate Studies of
Texas A&M University
in partial fulfillment of the requirements for the degree of

DOCTOR OF PHILOSOPHY

Approved by:

Chair of Committee,	M. T. Schobeiri
Committee Members,	Hamn C. Chen
	Je C. Han
	Sai C. Lau
Head of Department,	Dennis O' Neal

May 2009

Major Subject: Mechanical Engineering

ABSTRACT

Film Cooling, Heat Transfer and Aerodynamic Measurements in a Three Stage Research Gas Turbine.

(May 2009)

Arun Suryanarayanan, B.E., University Visvesvarya College of Engineering, Bangalore, India;

M.S., Texas A&M University

Chair of Advisory Committee: Dr. M.T. Schobeiri

The existing 3-stage turbine research facility at the Turbomachinery Performance and Flow Research Laboratory (TPFL), Texas A&M University, is re-designed and newly installed to enable coolant gas injection on the first stage rotor platform to study the effects of rotation on film cooling and heat transfer. Pressure and temperature sensitive paint techniques are used to measure film cooling effectiveness and heat transfer on the rotor platform respectively. Experiments are conducted at three turbine rotational speeds namely, 2400rpm, 2550rpm and 3000rpm. Interstage aerodynamic measurements with miniature five hole probes are also acquired at these speeds. The aerodynamic data characterizes the flow along the first stage rotor exit, second stage stator exit and second stage rotor exit. For each rotor speed, film cooling effectiveness is determined on the first stage rotor platform for upstream stator-rotor gap ejection, downstream discrete hole ejection and a combination of upstream gap and downstream hole ejection. Upstream coolant ejection experiments are conducted for coolant to mainstream mass flow ratios of MFR=0.5%, 1.0%, 1.5% and 2.0% and downstream discrete hole injection tests corresponding to average hole blowing ratios of M = 0.5, 0.75, 1.0, 1.25, 1.5, 1.75 and 2.0 for each turbine speed. To provide a complete picture of hub cooling under rotating conditions, experiments with simultaneous injection of coolant gas through upstream and downstream injection are conducted for an of MFR=1% and M_{holes}=0.75, 1.0 and 1.25 for the three turbine speeds. Heat transfer coefficients are determined on the rotor platform for similar upstream and downstream coolant injection. Rotation is found to significantly affect the distribution of coolant on the platform. The measured effectiveness magnitudes are lower than

that obtained with numerical simulations. Coolant streams from both upstream and downstream injection orient themselves towards the blade suction side. Passage vortex cuts-off the coolant film for the lower MFR for upstream injection. As the MFR increases, the passage vortex effects are diminished. Effectiveness was maximum when M_{holes} was closer to one as the coolant ejection velocity is approximately equal to the mainstream relative velocity for this blowing ratio. Heat transfer coefficient and film cooling effectiveness increase with increasing rotational speed for upstream rotor stator gap injection while for downstream hole injection the maximum effectiveness and heat transfer coefficients occur at the reference speed of 2550rpm.

DEDICATION

This work is dedicated to my grandparents, parents, Mr. A. Suryanarayanan and Mrs. Devi Suryanarayanan, and my sister, S. Anu Priya, who have been a source of unlimited moral support and encouragement.

ACKNOWLEDGMENTS

The author would like to express his sincere gratitude to Dr. Taher Schobeiri for his invaluable advice, guidance and motivation throughout the duration of the project. The time I have spent with him has been more than a learning experience. I wish to thank Dr. Je C. Han for the knowledge he has passed on to me in the years I have known him. I am thankful to Dr. Sai Lau and Dr. Hamn Ching Chen for being on my advisory committee. Special thanks to Mr. Eddie Denk for making my life at the turbolab easier with his timely and expert suggestions and also for allowing me the privilege to set up a secondary tool room in my test cell using tools from his shop. Jason Caswell, from the physics shop, has been a good friend and a savior whenever the electronics in my room thought it wise to work independently without my approval. My friends at the turbomachinery laboratory, Burak Ozturk, Ahmed Gamal, Adolfo Delgado, Sang Hyun Park and Hicham Chibli have been a lot of fun to be around and without them College Station would have been bland. I also wish to thank my other friends at the turbolab for their continued support through my work.

TABLE OF CONTENTS

Page

ABSTRACT iii

DEDICATION v

ACKNOWLEDGMENTS vi

TABLE OF CONTENTS vii

LIST OF TABLES x

LIST OF FIGURES xi

NOMENCLATURE xiv

1. INTRODUCTION 1

1.1 Turbine Aerodynamic Research 1
1.2 Turbine Film Cooling and Heat Transfer Research 5
1.2.1 Steady and Unsteady Heat Transfer and Film Cooling Research 6
1.2.2 Cascade Heat Transfer and Film Cooling –General-Research 9
1.2.3 Turbine Cascade-General Heat Transfer and Film Cooling Research on Turbine Platform 10
1.2.4 Rotating Rig Film Cooling and Heat Transfer - General Research 13
1.2.5 Heat Transfer and Film Cooling Research on Rotating Platform 16

2. RESEARCH PROGRAM AND OBJECTIVES 17

2.1 Film Cooling Effectiveness 17
2.2 Heat Transfer Measurements 18
2.3 Aerodynamics 18

3. EXPERIMENTAL FACILITY 19

3.1 Interstage Instrumentation 21
3.2 New Turbine Component Design 25

Page

4. EXPERIMENTAL PROCEDURE 30

4.1 Aerodynamic Measurement Theory and Analysis 30
4.2 Film Cooling Effectiveness Measurement Theory and Data Analysis 31
4.2.1 Data Acquisition Procedure for Film Cooling Effectiveness Measurements Using PSP Technique 35
4.3 Heat Transfer Coefficient Measurement Theory and Analysis 36
4.3.1 Data Acquisition Procedure for Heat Transfer Measurements Using TSP Technique 37

5. RESULTS AND DISCUSSION 40

5.1 Experimental Film Cooling Effectiveness Measurements 40
5.1.1 Film Cooling Effectiveness from Upstream Slot Injection 41
5.1.1.1 Upstream Injection at Reference Rotating Condition 41
5.1.1.2 Upstream Injection at Off-Reference Rotating Conditions 44
5.1.1.3 Different Turbine Rotating Speeds (Mass Flow Ratio Effect) 48
5.1.1.4 Pitchwise Averaged Film Cooling Effectiveness with Upstream Injection 48
5.1.2 Film Cooling Effectiveness from Discrete Film Cooling Holes 51
5.1.2.1 Reference Rotating Case 53
5.1.2.2 Effect of Rotation on Film Cooling 55
5.1.2.3 Pitchwise Average Film Cooling Effectiveness 58
5.1.3 Combined Upstream Stator-Rotor Gap Purge Flow Cooling and Downstream Discrete Hole Cooling 59
5.2 Experimental Heat Transfer Measurements 63
5.2.1 Heat Transfer from Upstream Slot Cooling 64
5.2.1.1 Upstream Injection at Reference Rotating Condition 64
5.2.1.2 Upstream Injection at Off-Reference Rotating Condition 65
5.2.1.3 Pitchwise Averaged Heat Transfer Coefficients with Upstream Injection 66
5.2.2 Heat Transfer due to Downstream Hole Cooling 69
5.2.2.1 Downstream Injection at Reference Rotating Condition 70
5.2.2.2 Downstream Injection at Lower Rotational Speeds 73
5.2.2.3 Pitchwise Averaged Heat Transfer Coefficients with Downstream Discrete Hole Injection 73
5.3 Aerodynamic Flow Measurements 75
5.3.1 Interstage Instrumentation 75
5.3.2 Aerodynamic Flow Measurement – Probe Set-up Instructions 75
5.3.3 Aerodynamic Flow Measurement – Results and Discussion 76

6. UNCERTAINTY ANALYSIS 85

6.1 Uncertainty Analysis for Aerodynamic Measurements Using 5-Hole Pitot Probes 85
6.2 Uncertainty Analysis for Film Cooling Effectiveness Measurements Using PSP 87

Page

6.3 Uncertainty Analysis for Heat Transfer Measurements Using TSP 88

7. SUMMARY AND CONCLUSIONS 89

7.1 Film Cooling Effectiveness Measurements Using PSP 89
7.1.1 Stator- Rotor Gap Coolant Injection 89
7.1.2 Downstream Discrete Hole Coolant Injection 90
7.1.3 Combined Upstream Stator-Rotor Gap and Downstream Discrete Hole Coolant Injection 90
7.2 Heat Transfer Coefficients Measurement Using TSP 91
7.3 Aerodynamic Measurements 91
7.4 Future Investigation 93

REFERENCES 94

APPENDIX A 104

APPENDIX B 115

APPENDIX C 125

APPENDIX D 129

APPENDIX E 150

APPENDIX F 163

APPENDIX G 167

APPENDIX H 172

VITA 173

LIST OF TABLES

Page

Table 1: Turbine dimensions and operating conditions..... 20

Table 2: Uncertainty analysis for the miniature 5-hole probes..... 86

LIST OF FIGURES

Page

Figure 1: Modern Cooled Gas Turbine Blade (from Han et al. [17]). 4

Figure 2: Secondary Flow through a Blade Passage (from Han et al. [17]). 6

Figure 3: Existing Turbine Research Facility, (Schobeiri et al. [1] and [2]). 19

Figure 4: Turbine Cross Section Showing T-ring Slots for Circumferential Interstage Aerodynamic Measurements, (Schobeiri et al. [1] and [2]). 21

Figure 5: Schematic of the 5 Hole Probe Adjustment Angle at Station 3, 4 and 5, (Schobeiri et al. [1] and [2]). 23

Figure 6: Section View of the Modified Stator-Rotor Turbine Assembly for Stator-Rotor Purge Flow and Platform Film Cooling. 24

Figure 7: Turbine Components with the 24 Channel Slip Ring and Upstream Stator-Rotor Gap Cavity. 25

Figure 8: Detailed Views of Stator-Rotor Gap and Downstream Discrete Holes. 26

Figure 9: Heater Element as Mounted on the Rotor Platform Blade Passage. 27

Figure 10: Insert Used to Mount Heater on the Rotor Platform. 28

Figure 11: Typical Pressure Sensitive Paint Calibration Setup and Calibration Curve. 32

Figure 12: Optical Components Setup for the Model Turbine and PSP. 34

Figure 13: Film Cooling Effectiveness Distribution on the Rotating Endwall for 2550rpm. 40

Figure 14: Velocity Triangles and Relative Inlet and Exit Flow Angles for Design and Off-Design Rotating Speeds. 43

Figure 15: Numerical Prediction of Endwall Static Pressure Distribution (kPa) along with Flow Pathlines, ([100] and [101]). 44

Figure 16: Film Cooling Effectiveness Distribution on the Rotating Endwall for 2400rpm. 45

Figure 17: Film Cooling Effectiveness Distribution on the Rotating Endwall for 3000rpm. 46

Figure 18: Pitchwise Averaged Film Cooling Effectiveness Distribution along Axial Chord for Different MFR (Mass Flow Ratio Effect). 47

Figure 19: Pitchwise Averaged Film Cooling Effectiveness Distribution along Axial Chord for Different Mass Flow Ratios (Turbine Rotation Effect). 49

Figure 20: Comparison of Pitchwise Average Effectiveness with a Correlation from Goldstein [40] for Different Speeds. 50

Page

Figure 21: Film Cooling Effectiveness Distribution from Downstream, Discrete Film Cooling Holes on the Rotating Endwall for 2550rpm. 52

Figure 22: Film Cooling Effectiveness Distribution from Downstream, Discrete Film Cooling Holes on the Rotating Endwall for 2400rpm. 54

Figure 23: Film Cooling Effectiveness Distribution from Downstream Discrete Film Cooling Holes on the Rotating Endwall for 3000rpm. 56

Figure 24: Pitchwise Averaged Film Cooling Effectiveness Distribution along Axial Chord for Different Turbine Rotating Speeds (Mass Flow Ratio Effect). 57

Figure 25: Pitchwise Averaged Film Cooling Effectiveness Distribution along Axial Chord for Different Hole Blowing Ratios (Rotation Effect). 58

Figure 26: Film Cooling Effectiveness for Combined Stator-Rotor Gap and Hole Coolant Injection, 2400rpm. 59

Figure 27: Film Cooling Effectiveness for Combined Stator-Rotor Gap and Hole Coolant Injection, 2550rpm. 60

Figure 28: Film Cooling Effectiveness for Combined Stator-Rotor Gap and Hole Coolant Injection, 3000rpm. 60

Figure 29: Pitchwise Averaged Film Cooling Effectiveness for Combined Upstream Slot and Downstream Discrete Hole Injection. 62

Figure 30: Heat Transfer Coefficient Distribution from Upstream Stator-Rotor Gap Coolant Injection on the Rotating Endwall for 2550rpm. 63

Figure 31: Heat Transfer Coefficient Distribution from Upstream Stator-Rotor Gap Coolant Injection on the Rotating Endwall for 2400rpm. 66

Figure 32: Pitchwise Averaged Heat Transfer Coefficient Distribution along Axial Chord for Different Turbine Rotating Speeds (Mass Flow Ratio Effect). 67

Figure 33: Pitchwise Averaged Heat Transfer Coefficient Distribution along Axial Chord for Different Mass Flow Ratios (Rotation Effect). 68

Figure 34: Heat Transfer Coefficient Distribution from Downstream Discrete Hole Coolant Injection on the Rotating Endwall for 2550rpm. 70

Figure 35: Heat Transfer Coefficient Distribution from Downstream Discrete Hole Coolant Injection on the Rotating Endwall for 2400rpm. 72

Figure 36: Pitchwise Averaged Film Cooling Effectiveness Distribution along Axial Chord for Different Turbine Rotating Speeds (Blowing Ratio Effect) 72

Figure 37: Pitchwise Averaged Heat Transfer Coefficient Distribution along Axial Chord for Different Turbine Rotating Speeds (Blowing Ratio Effect). 74

Page

Figure 38: Variation of Absolute Flow Angle, Alpha, and Meridional Flow Angle, Gamma, with Rotor Speed at the Stator-Rotor Gap Exit, MFR=1.00%. 76

Figure 39: Variation of Absolute Flow Velocity with Rotor Speed at the Stator-Rotor Gap Exit, MFR=1.00%. 77

Figure 40: Variation of Circumferential Flow Velocity with Rotor Speed at the Stator-Rotor Gap Exit, MFR=1.00%. 78

Figure 41: Variation of Absolute Flow Angle, Alpha, with MFR at the Stator-Rotor Gap Exit, 2550rpm. 78

Figure 42: Variation of Meridional Flow Angle, Gamma, with MFR at the Stator-Rotor Gap Exit, 2550rpm. 79

Figure 43: Variation of Non-Dimensionalized Circumferential Velocity, with MFR at the Stator-Rotor Gap Exit, 2550rpm. 80

Figure 44: Radial Distribution of Absolute Flow Velocity, 2550rpm. 81

Figure 45: Radial Distribution of Relative Flow Velocity, 2550rpm. 81

Figure 46: Radial Distribution of Total and Static Pressures, 2550rpm. 82

Figure 47: Contour Plots of Total Pressure Distribution, 2550rpm. 83

Figure 48: Contour Plot Distribution of Static Pressure Distribution, 2550rpm. 84

NOMENCLATURE

A_{heater}	Heater surface area
C	Oxygen concentration
C_x	Axial chord length of the rotor blade (4.16 cm)
D_h	Rotor diameter at blade hub (cm)
D_t	Rotor diameter at blade tip (cm)
$f(P_{ratio})$	Relation between intensity ratio and pressure ratio
h	Heat transfer coefficient (W/m^2- K)
i	Incidence flow angle change from design point (3000rpm) at the first stage rotor inlet
I	Pixel intensity for an image
I_{heater}	Heater current (Amperage)
K	Material thermal conductivity (W/m-K)
M_{holes}	Average blowing ratio ($=\rho_c V_c / \rho_m W_2$)
MFR	Mass flow ratio (% of mainstream core flow)
LE	Leading edge of the blade
M	Mach number
P	Pressure (Pa)
P1	Pressure reading from the first hole of the five hole Pitot probe, Pa
P2	Pressure reading from the second hole of the five hole Pitot probe, Pa
P3	Pressure reading from the third hole of the five hole Pitot probe, Pa
P4	Pressure reading from the fourth hole of the five hole Pitot probe, Pa
P5	Pressure reading from the fifth hole of the five hole Pitot probe, Pa
PS	Pressure side
PSP	Pressure sensitive paint
P_{O_2}	Partial pressure of oxygen

Q	Heat energy (W)
r	Degree of reaction ($=\Delta h''/(\Delta h' + \Delta h'')$)
R	Heater coil resistance (Ohms)
Re	Reynolds number
Ro	Rotation number at first stage ($=U_2/W_2$)
S	Normal stator-rotor gap width (= 2.3mm)
SS	Suction side
T	Temperature (°C)
T_m	Mainstream temperature (°C)
TSP	Temperature sensitive paint
V_c	Avg. velocity of coolant air from the stator-rotor gap (m/s)
U	Tangential average velocity (m/s)
V	Avg. absolute velocity (m/s)
V_{circ}	Circumferential velocity (m/s)
V_u	Tangential component of absolute velocity (m/s)
W	Relative average velocity of mainstream air (m/s)
w_n	Measurement uncertainty for n^{th} instrument
x	Axial distance from blade leading edge (cm)
α	Pitch angle (º)
α_v	Absolute velocity flow angle (º)
β_v	Relative velocity flow angle (º)
γ	Yaw angle (º)
γ_c	Lateral coolant hole orientation angle (º)
θ	Streamwise coolant hole orientation angle (º)
δ	Probe correction angle (º)

ΔP Static pressure difference on the platform across the pressure and suction surface of adjacent blades

ΔS Pitchwise incremental length on the platform across the pressure and suction surface of adjacent blades

ϕ 1st stage flow coefficient, $\phi = V_{ax}/U_3$

λ 1st stage load coefficient, $\lambda = \left(U_2 V_{u_2} + U_3 V_{u_3}\right) / U_3^2$

ε Emissivity

η Local film-cooling effectiveness

ρ_c Density of coolant air (kg/m^3)

ρ_m Density of mainstream air at first stage stator exit (kg/m^3) =1.01 kg/m^3

σ Stefan Boltzmann constant, 5.67 x 10^{-8} W/m^2- K^4

SUBSCRIPT

1 At first stage stator inlet

2 At first stage stator exit (rotor inlet)

3 At first stage rotor exit

4 At second stage stator exit

5 At second stage rotor exit

air mainstream air with air as coolant

aw adiabatic wall

ax axial

blk image without illumination (black)

c coolant

cond conduction

f local film temperature

h heater

i	initial value
in	supplied
ins	insulation
loss	lost
mix	mainstream air with nitrogen as coolant
m	central hole of the 5-hole probe
n	independent variable
N_2	mainstream air with nitrogen as coolant
rad	radiation
ref	reference image with no mainstream and coolant flow
sta	static
stl	stainless steel

1. INTRODUCTION

1.1 Turbine Aerodynamic Research

Aerodynamic measurement and analysis of gas turbines is a continually evolving field with newer and accurate findings emerging regularly due to better instrumentation and improved measurement techniques. The results of such analyses are oriented towards providing the design engineer with sufficient information to put forward an improved design that would facilitate higher machine efficiencies. One of the primary causes leading to the loss of efficiency in a turbomachine is the secondary flow occurring in the rotor tip and the hub region. The flow near the blade tip and hub generate vortice which induce drag forces that reduce the mainstream total pressure. Similarly, the low energy boundary layer flow and cross flow across the blade pressure and suction surfaces on the rotor hub, also influence the mainstream flow near the hub, slowing it down and increasing the losses. Reduction of losses due to secondary flow can result in major energy savings by improving system efficiency. The measurement of the secondary flow near the blade tip and on the rotor hub is complicated and difficult due to the 3-D nature of the flow. Several attempts have been made by researchers to measure and quantify the characteristics of secondary flow and their effects on the performance of turbines.

Schobeiri et al. [[1], [2], [3]] and Wright and Schobeiri [4] investigated steady and unsteady wake development and decay and their effects on the boundary layer transition and losses. Their experiments were conducted in a low pressure turbine cascade and along the concave surface of a constant curvature plate at zero pressure gradients. Ristic et al [5] listed out the features contributing to the generation of 3-D flow in turbines. He found blade and endwall surface boundary layers, shock boundary layer interaction, blade wake, horseshoe vortices near blade leading edge, tip leakage flow and the secondary flow contributed to the complexity of the flow in turbines. He provided detailed information on the three dimensional viscous flow phenomena to better understand the flow behaviour such as the origin, development of wakes, secondary flow and leakage flows. The study was based on velocity measurement

---

This dissertation follows the journal style of *ASME Journal of Turbomachinery.*

taken with a three dimensional Laser Doppler Velocimeter system. Also, it was found that the tip leakage flow affects the mainstream flow up to 10% of the blade length from the blade tip and is characterised by strong vortice distributions.

The research turbine facility used for the current work is described in detail by Schobeiri et al. [1], [2] and [3]. The research turbine has the flexibility and capability to deal with current aerodynamics, film cooling and heat transfer issues. The secondary flow and its impact on efficiency and performance of turbine components are described extensively by Lakshminarayana [6] and Schobeiri [7]. Denton [8] gave an overview of the effects of different flow mechanisms including the secondary flow on turbomachinery losses. The platform surface is characterized by a highly complex 3-D flow due to the viscous nature of the mainstream hot gases. A detailed model of the different types of vortices generated and the nature of the secondary flow on the platform surface has been put forth by several people in the past (Langston et al. [9] , Goldstein and Spores [10], Takeishi et al. [11], Sieverding et al. [12], Herzig et al. [13] and Wang et al. [14]). Every model in general acknowledges the existence of a saddle point in the region near the blade leading edge on the platform beyond which the flow separates to give rise to pressure and suction side vortice commonly referred to as the horse shoe vortex. The pressure side horse shoe vortex, under the influence of the differential pressures existing across the pressure and suction surface of adjacent blades, migrates towards the suction side and either attaches or flows over or under the suction side horse shoe vortex, depending on the driving parameters. This vortex is commonly referred to as the passage vortex and almost always is detrimental to attempts made at platform cooling as it tends to lift the coolant off the surface. Further, the existence of several other secondary flow vortices also makes providing uniform platform cooling a difficult task. All the above investigations were conducted on a cascade and the influence of rotation on the end wall flows and the subsequent effects on the coolant flow hasn't been investigated.

In a very recent paper, Reid et al. [15] presented an investigation into the effect of the chordwise inter-platform leakage flow between vane segments on turbine performance. Their tests showed that the leakage flow can have a significant impact on turbine performance, but they pointed out that below a threshold leakage fraction the efficiency loss does not rise with increasing leakage flow rate. Bindon [16] theorized

the mechanisms involved in the generation of losses in turbines due to secondary flows also using turbine cascades. An up to date summary of the existing literature dealing with the endwall aerodynamics, film cooling and heat transfer is also provided by Han et al.[17], Simon and Piggush [18]and Bogard and Thole[19].

Paniagua et al. [20] investigated the hub endwall cavity flow that exists due to small gaps between the stator and rotor disk. They found that though the volume of leakage flow injected through the gap is small, it has significant effect on the mainstream flow. The injection of leakage flow increases the static pressures at the stator exit by 6%. The interaction of flow and the mainstream flow reported in this paper is analogous to the interaction of coolant ejected and rotation influenced mainstream flow in the current work.

The mainstream flow along a gas turbine is influenced by the characteristics of the stages ahead of them. Urbassik et al. [21] conducted experiments to investigate the unsteady interaction between a high pressure turbine vane and rotor blade. The rotor blade was influenced by the flow potential as well as the shock propagating through it while the vane was affected by only the flow potential. Upstream vane wakes had little to no effect on the unsteadiness in the rotor blades.

Influence of blade leading edge geometry on endwall heat transfer and flow was studied by Han and Goldstein [22]. Aerodynamic losses are believed to be lower for optimum leading edge fillets. A naphthalene sublimation technique on fillet geometry is investigated to determine local heat transfer coefficients. A comparison of this result with a simple blade with no fillet is made and found that for the modified blade, the horse shoe vortex is not observed while the passage vortex is diminished or not seen depending on the fupstream turbulence intensities.

In a series of two papers, Praisner and Smith [23] and [24] investigated the characteristics of horseshoe vortex and their effects on endwall heat transfer. PIV and liquid crystal technique was used in conjunction with one another to simultaneously measure the endwall vortex flow and heat transfer coefficients respectively. All the features described by earlier researchers were seen clearly with the horseshoe vortex breaking of near the blade leading edge. Time averaged and mean heat transfer distribution on the endwall is presented for a turbulent flow created by a blunt body.

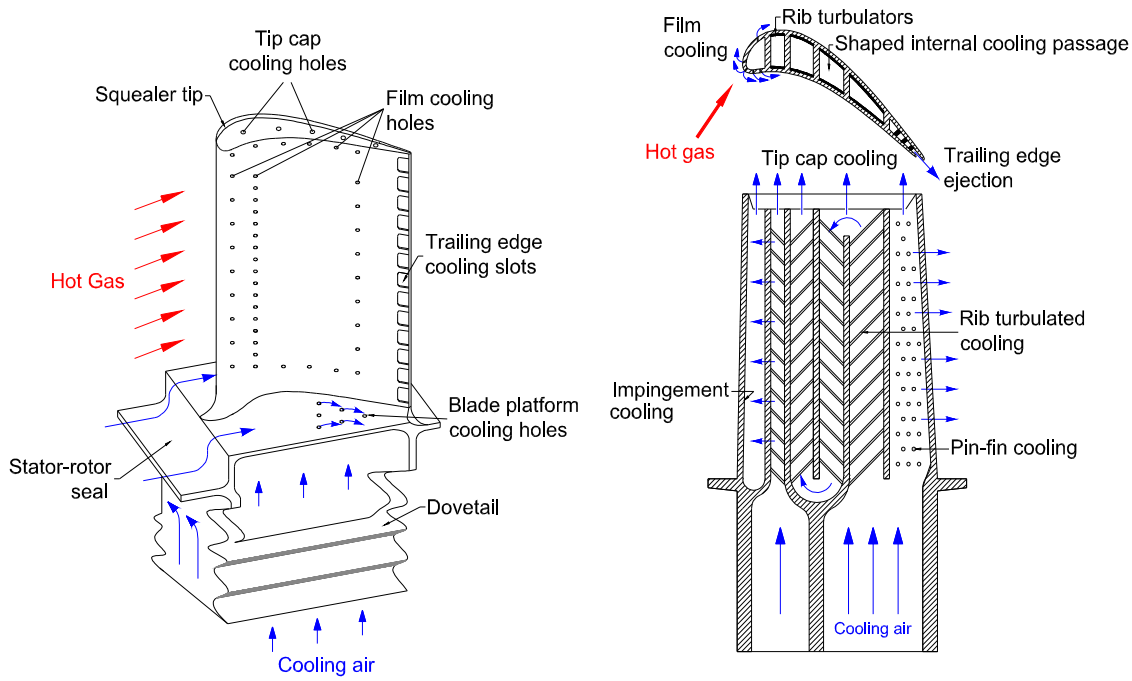

Figure 1: Modern Cooled Gas Turbine Blade (from Han et al. [17]).

Interaction of the leakage flow from the stator-rotor disk gap with mainstream flow and endwall heat transfer is also presented by Rehder and Dannhauer [25]. Experiments were performed on a contoured platform with representative engine conditions. Infra red cameras were used to measure temperatures while a 2-D PIV system allowed for flow measurements near the coolant ejection location. They observed that when coolant was injected perpendicular to the mainstream flow, the horseshoe vortex was substantially amplified and endwall heat transfer was also enhanced. For tangential leakage ejection, the vortex system was noticed to diminish. Recently, Piggush and Simon [26] studied the effects of endwall contouring and disk misalignment in a turbine cascade facility. A forward facing step is found to locally accelerate the leakage flow, thinning the boundary layers and enhancing the heat transfer on the endwall. On the contrary, the backward facing step increased the boundary layer thickness and decreased the endwall heat transfer. Similar studies to study the leakage flow effects on mainstream flow and endwall

heat transfer were performed by Reid et al. [27] and Leishman et al. [28]. All the investigations concerning the leakage flow are all performed on cascades and none of them take into account the fact that the leakage flow ejecting out of the disk space is also affected by the rotor rotation. A tangential velocity component which the leakage flow might acquire while leaving the disk space may substantially alter the flow pattern around the slot.

1.2 Turbine Film Cooling and Heat Transfer Research

The initial stages of the turbine are constantly exposed to high temperatures from gases exiting the combustion chamber. For a given aerodynamic efficiency, any increase in the turbine inlet temperature translates to an increase in the thermal efficiency and hence, the overall system efficiency. In pursuit of higher thermal efficiencies, gas turbines are operated at first stage inlet temperatures around 1500°C resulting in excessive thermal stresses on the turbine components. Continuous operation under high turbine inlet temperatures enhances the possibility of thermal failure of the hot gas path components. Also, the uniform temperature profile of the gases exiting the present day combustors further exposes the rotor platform to higher temperatures requiring effective thermal protection. The life of the turbine airfoils can be increased by implementing any of a variety of cooling techniques, as shown in Figure 1. Film cooling is an external cooling technique commonly used in conjunction with internal cooling to protect the turbine components from the mainstream hot gas. In film cooling, a portion of the coolant used for internal cooling is ejected through discrete holes or slots over the surface of the components that need thermal protection. The coolant thus ejected displaces the mainstream boundary layer creating a protective film on the surface of the exposed component. This isolates the hot mainstream gas from the metal surface and considerably decreases the magnitude of the temperatures the hot gas path components encounter. The location of the coolant holes, their geometry and the quantity of the coolant gases are critical in providing proper coolant film protection. In addition, the complex 3D flow (Figure 2) around the turbine blade can have adverse effects on the film coverage across the airfoils.

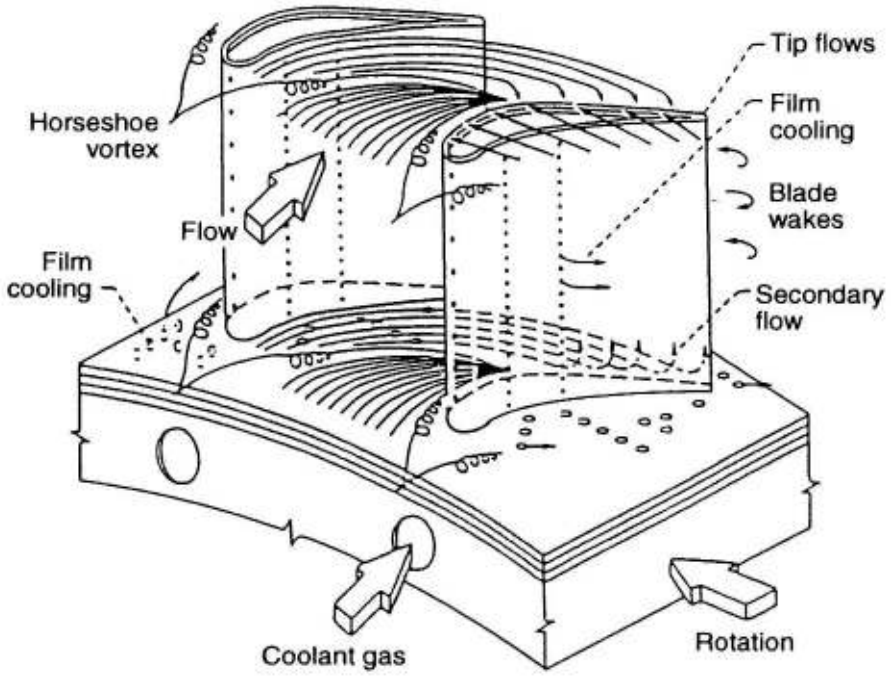

Figure 2: Secondary Flow through a Blade Passage (from Han et al. [17]).

1.2.1 Steady and Unsteady Heat Transfer and Film Cooling Research

Heat transfer on the hot gas path components are significantly affected by the nature of flow that passes through them. Insufficient knowledge as to their effects will often lead to under cooled components leading to thermal fatigue failures. Effects of upstream flow conditions on heat transfer have been a subject of investigation for several years. Priddy et al. [29] studied the effects of steady and unsteady flow conditions on heat transfer in a turbine blade using a cascade facility for a variety of upstream flow simulating actual conditions existing in a turbine. The steady state conditions were simulated using upstream girds while the unsteady flow conditions were obtained a squirrel cage. They found that any increase in the upstream turbulence caused a higher heat transfer coefficient near the blade leading edge. The pressure surface too showed enhanced heat transfer with higher turbulence. The also studied the effects of turbulence on flow transition and related heat transfer to it.

Martin and Brown [30] listed the factors influencing heat transfer on the pressure side of the turbine blade. It was suggested that the existence of Taylor-Goertler vortices and upstream turbulence had a significant effect on the blade pressure side heat transfer. Each of this parameter both separately or in concert caused the pressure side heat transfer to increase above average values. Yi Liu [31] predicted the aerodynamic and heat transfer performance of a highly loaded turbine vane taking into account the impact of upstream wake, shock waves and boundary layer. A modified Navier Stokes (N-S) equation was used to model the mainstream flow while a K-ε model accounted for the turbulence. A similar study was conducted by Thakur et al. [32] for a leading edge film cooling blade. The results of both the simulations in general matched fairly well with experiments. Any variations in the predicted data were attributed to the anisotropy of the system turbulence which could not be modelled more accurately.

Pasinato et al. [33] compared numerical predictions with experiments and attempted to quantify the flow field and heat transfer in a linear cascade platform. Coolant was injected through 3 discrete angled slots positioned upstream of the stator. The coolant injection was found to alter the flow patter on the platform, interacting with the horse shoe vortex and enhancing heat transfer. Total pressure measurements also were made to quantify any changes in aerodynamic losses associated with coolant injection. The numerical analysis over predicted the film cooling effectiveness compared to the experimental case. This is similar to that observed during the current investigation of coolant injection on rotating platform.

Schook et al. [34] measured heat transfer on flat plates at high Mach numbers using a Ludwieg tube set up. Turbulence was generated upstream by means of grids of different pitch and varied between 0.25% and 3.5%. Thin film technique was used to make temperature measurements of the test section. The experiments showed that the initiation of transition was substantially affected by increasing turbulence. The structure of turbulence itself was found had a more significant effect on transition than the turbulence. The Stanton numbers were reported to increase locally with increasing upstream turbulence.

A detailed experimental study was performed by Liu and Rodi [35] to experimentally determine the effects of wake induced unsteady flow on heat transfer in a linear turbine cascade. A squirrel cage apparatus was used to vary the upstream wake induced passing frequency between 0 and 240Hz. Their results showed that the boundary layer on the suction side remained laminar only for steady flow

condition. Under unsteady flow, the boundary layer was transitional and moved towards the leading edge for higher frequencies. The boundary layer on the pressure side remained laminar for all flow conditions. Any increase in turbulence translated to a higher heat transfer coefficient along the blade.

Al-Hamadi et al. [36] focused on the effects of free stream turbulence on film cooling effectiveness and heat transfer on turbine blades using a cascade facility. Turbulence intensity was varied between 0.43% and 17% using upstream turbulence grids. Similar research was conducted by Mehendale et al. [37] with air and CO_2 injection to study the density ratio effects along with mainstream turbulence. Several blowing ratios were also considered for the study. Turbulence intensity was varied between 0.7% and 17% using upstream grids. The results showed that in general heat transfer coefficient increased with increasing upstream turbulence and coolant blowing ratio.

Butler et al. [38]conducted a study to quantify the effects of turbulence intensity and length scale on turbine aerodynamics and heat transfer on a low pressure turbine blade. Turbulence intensities between 0.8% and 10% along with Reynolds numbers of 40000 to 80000 were considered for the experiments. Biplanar lattice grids positioned upstream of the test section generated the required turbulence intensity. Surface temperatures were measured using uniform heat flux liquid crystal technique. The results showed as the turbulence increased, suction side boundary layer moved upstream causing the heat transfer coefficients to increase locally. The stagnation location heat transfer also was enhanced for higher mainstream turbulence.

Han et al. [39] studied the influence of upstream Strouhal number and concluded that both Reynolds number and Strouhal number are important for calculation of unsteady flow heat transfer coefficients. Several parameters like the upstream rod diameter, the rod spacing and speed, mainstream velocities were considered for the study. Their results showed that the unsteady passing wake promotes boundary layer transition much earlier than for no wake cases and enhances the heat transfer coefficients on the suction surface. The passing wakes also tend to increase the heat transfer coefficient on the pressure side substantially.

Jenkins et al. [40] quantified the effects of mainstream turbulence and film cooling on a stator blade dispersion of a hot streak. Results from upstream turbulence magnitudes of 3.5% and 20% were compared

and found that the hot streak was diminished due to higher turbulence. A 75% reduction in the temperatures in the hot streak region was noticed with the introduction of coolant flow. Different combinations of coolant injections were also tested.

1.2.2 Cascade Heat Transfer and Film Cooling –General-Research

Results of heat transfer experiments rotor blades mounted in a transonic cascade was presented by Giel et al. [41]. Four different Reynolds numbers were considered along with three pressure ratios. The changing Reynolds number altered the flow on the suction surface by changing the location of the transition zone. Changing pressure ratio had little to no effect on the blade heat transfer. Changing the inlet flow angle affected the pressure gradients on the blade and in turn the location of the transition zone.

Nasir et al. [42] experimented with different tip gaps and squealer geometries on heat transfer on a high pressure turbine blade using a rotor blade on the cascade. Transient liquid crystal technique was used to measure the temperature distribution on the blade tip for two different blade tip gap to r=span ratio. The squealer tipped blade showed lower coolant crossing over from the pressure side to the suction side and the associated heat transfer also decreased.

A computational study was performed by Kohli and Bogard [43] to alter the contour of the suction side blade cooling hole to improve the film cooling effectiveness. The optimization method was tested on real scale model in a low wind tunnel and found the predictive method capable of designing blade contours. Brian and Langston modelled the leading edge heat transfer and analytically, experimentally and using computational methods. Ligrani and Hedlund [44] presented the results of experiments performed on a curved channel for laminar, transitional and turbulent flows. Heat transfer and flow structure were quantified using flow visualisation techniques and standard procedure used to measure heat transfer coefficients. Higher Nusselt numbers were seen for the concave section of the channel for different Dean numbers representing the upstream flow conditions.

Bernsdorf et al. [45] performed film cooling experiments on a flat plate to simulate the pressure side of a turbine blade. 3-D PIV measurements were made to quantify the flow field and two different hole geometries were considered. The observed the classic kidney vortex pair and the jet lift-off at higher

momentum flux ratios. The incoming boundary layer thickness is minimised by the presence of injected coolant and the effect is amplified with increasing blowing ratio, density ratio and hole angle.

1.2.3 Turbine Cascade-General Heat Transfer and Film Cooling Research on Turbine Platform

Platform film cooling effectiveness investigations have been predominantly performed using cascade vanes due to the inherent complexities in designing and instrumenting rotating systems. One of the earliest studies on platform film cooling was performed by Blair [46] using an upstream slot in a large scale turbine vane passage. Harasgama and Burton [47] conducted heat transfer and aerodynamic measurements in an annular cascade fit with vanes under representative engine flow conditions. Their results show that film cooling reduced the Nusselt numbers near the suction side by about 50% suggesting that the coolant was convected towards the suction side by the passage secondary flows. Friedrichs et al. [48] and [49] detailed the aerodynamic aspects of platform film cooling and the effectiveness distributions using the ammonia and diazo technique. The tests were performed in a large scale low-speed turbine cascade with four rows of film cooling holes along four axial stations on the platform. The presence of secondary flows was found to erode the coolant film near the surface necessitating a detailed investigation of the flow phenomenon in this region. The film cooling traces were observed to be pushed towards the suction side especially near the leading edge of the blade similar to that observed by Harasgama and Burton [47]. They also concluded that platform film cooling can increase aerodynamic losses due to the mixing of the coolant with the mainstream.

A review of heat transfer and cooling on a turbine nozzle platform has been done by Chyu [50]. Zhang and Jaiswal [51] investigated film cooling in a turbine nozzle endwall with two different upstream coolant hole geometries using pressure sensitive paint. Effects of coolant mass flow on the effectiveness and distribution of coolant gas were studied. Lower coolant mass flow was found to be less effective in counteracting the effects of secondary flow in the endwall region and hence led to lower film cooling effectiveness. Higher coolant-to-mainstream mass flow ratios gave a more uniform effectiveness distribution. Kost and Nicklas [52], Nicklas [53] and Kost and Mullaert [54]studied the effects of film cooling and heat transfer on the endwall of a linear cascade. The location of the upstream cooling slot with

respect to the blade leading edge was found to determine the effectiveness of film cooling. Slots positioned near the saddle point tended to reinforce the horse shoe vortex and the increased turbulence washed away the effects of the coolant fluid decreasing film effectiveness. For cooling the platforms upstream of the blade passage, slot ejection was found to be more useful than discrete holes. Film cooling through holes enhanced the heat transfer coefficients as compared to the no blowing cases.

Tests on film cooling effectiveness on contoured platforms were performed by Oke et al. [55], [56], [57] in a linear, low speed cascade. Coolant was injected through single and double slots upstream of the blades. Film cooling hole patterns on the platform with several holes along with slot injection were studied by Knost and Thole [58] in a low speed cascade with nozzle guide vanes. Patterns with film cooling holes along iso-Mach lines were found to give much better film coverage. The effect of a back facing step before coolant injection was studied by Zhang and Moon [59] to simulate realistic engine geometry conditions. They used PSP to determine the film cooling effectiveness and found that a back facing step caused an unstable boundary layer and damages film coverage. Component misalignment with a forward as well as a backward step, at the upstream injection slot and on the slashface gap, was investigated by Piggush and Simon [60]. They studied flow and loss characteristics associated with these features and noticed that blowing through the slashface gap has the most significant impact on the passage losses. Similar assembly features were also studied by Cardwell et al. [61].

Hada and Thole [62]computationally predicted the film cooling effectiveness with upstream and mid-passage slot on turbine endwall and also for the height difference between the upstream slot and the downstream endwall. Adiabatic film cooling effectiveness using wide banded thermochromic liquid crystals was measured on the turbine endwall nozzle vane cascade by Barigozzi et al. [63] for fan shaped holes with different area ratios. The secondary flow was suppressed for the smaller area ratios as the coolant exiting the holes had higher momentum to overcome the effects of the secondary flow, thus decreasing the secondary losses. As expected increase in hole area ratio ensured wider spread for the exiting coolant.

Transient liquid crystal technique was used by Nasir et al. [64] to measure film cooling through cylindrical holes on a flat plate with triangular tabs placed along different orientations upstream of the

coolant holes. Certain combinations of the coolant blowing ratio and the tab orientation produced higher effectiveness implying that the common denominator for higher effectiveness is the nature of flow around the hole. A similar research was performed by Yeun and Martinez-Botas [65] to study the effects of coolant hole orientation for L/D=4.0 and P/D=3 to 6 on effectiveness distribution on a flat plate. Several holes in in-line and staggered form with different angles were tested for different blowing ratios.

Large eddy simulations were performed by Rozati et al. [66] on blade leading edge film cooling. His models predicted that the adiabatic effectiveness decreased with turbulent jets while not affecting the heat transfer significantly. The predictions of turbulent coolant jet concurred with the experimental results only for spanwise averaged adiabatic film cooling effectiveness. Heat transfer coefficient data was not affected much and was closer to experimental values as they were influenced only by the turbulence around the coolant hole.

Thin film technique was used by Guo et al. [67] to measure turbine vane heat transfer and film cooling effectiveness. The free stream velocity was maintained at 13% to simulate close to actual engine conditions. Their experiments showed that fan shaped holes had higher effectiveness magnitudes on the blade surface as compared to cylindrical holes. Pressure surface showed a higher increase than the suction surface with the fan shaped holes. Garg et al. [68] again compared experimental measurements of Nusselt numbers with predicted values for a film cooled turbine blade. A 3-D N-S based program was found to reasonably predict heat transfer coefficients on the suction surface and on the turbine hub.

Endwall and blade heat and mass transfer in a linear cascade was numerically predicted by Papa et al. [69]. The blade profile selected for the modelling closely resembled a rotor blade though the predictions did not account for rotation. A Reynolds Averaged Navier Stoke's model along with a modified K- ω model was used to model the mainstream flow and turbulence respectively. The model was able to predict well the heat transfer coefficients on the endwall up to the location where the passage vortex combined with a leg of the horse shoe vortex. Beyond this zone, the predicted values were higher than those observed during experiments.

The PSP technique for film cooling effectiveness is based on mass transfer analogy and is free from heat conduction related errors frequently encountered with other heat transfer measurement techniques

measuring adiabatic effectiveness. A complete map of local film cooling effectiveness distribution on the rotor platform surface can be obtained rather than just a few discrete points obtained using heat flux gages or thermocouples. The results from this technique have been calibrated with other measurement techniques by Wright et al. [70] on a film cooled flat plate, Gao et al. [71] on a film cooled turbine blade leading edge model and Wright et al. [72] on a turbine cascade platform film cooling study. A detailed working methodology of PSP to measure film cooling effectiveness has been described in Wright et al. [92]. Since no heating is involved, errors arising from lateral heat conduction in the test surface are avoided resulting in a distinct and well-defined coolant trace. The results from this technique have also been successfully demonstrated by Ahn et al. [73]and Mhetras et al. [74] on blade tip film cooling.

Saumweber and Schulz [75] studied the interaction of two rows of coolant hole to quantify the performance of the downstream hole. He determined that the downstream film cooling is determined by the coolant parameters through the 2nd row and also the shape of the coolant holes themselves. Effectiveness is enhanced downstream of the 2nd row due to coolant ejection from the 1st row. Bons and McClain [76] investigated the effects of turbine component roughness and pressure gradients on heat transfer. Smooth surface heat transfer was found to be less sensitive to flow changes than surfaces with roughness. Roughness enhanced heat transfer irrespective of the pressure gradients though the magnitude of increase is smaller at higher pressure gradients. Rutledge et al. [77] also investigated the degradation performance of film cooling on a turbine vane suction side due to surface roughness. In general he found that roughness enhances heat transfer and the flux increased by 30% to 70% depending on the different tested cases.

1.2.4 Rotating Rig Film Cooling and Heat Transfer - General Research

Experimental studies available in open literature on film cooling and heat transfer on rotating turbine blades and their components are few and far between. The introduction of rotation increases the complexity of the heat transfer and film cooling measurements on any of the turbine hot gas components. The cooling designs available for these components are often a result of extrapolated data available from stationary cascades. This method, though functional can be further optimized with actual data from

rotating test rigs. This will enable the hot gas components to be cooled efficiently, increasing their life and also improving system performance by minimizing coolant usage. The primary issue with measuring data on a rotating facility is the difficulty in instrumenting the facility for all the necessary measurements and data acquisition.

Dring et al. [78] investigated film cooling performance in a low speed rotating facility with a film cooling hole positioned on both the pressure and suction sides of the blade. They used ammonia and Ozalid paper to qualitatively observe the coolant trace while the quantitative tests were conducted using thermocouples. Their results showed that the film coolant had only a small radial displacement, similar to flat plate results, on the suction side. On the pressure side, the film coolant trace had a large radial displacement toward the blade tip. Effectiveness distributions on the blade span for a rotating turbine blade were also provided by Takeishi et al. [79] and Abhari and Epstein [80] using gas chromatography and thin film heat flux gages respectively.

Garg [81] modeled a film cooled rotating blade to validate different turbulence models. He utilized Wilcox's K-ω, Coakley's q- ω and zero equation Baldwin Lomax methods to model the turbulence around the blade. A conclusive result couldn't be arrived at as each of the models was able to predict heat transfer accurately in different locations. Haldeman and Dunn [82] measured and predicted the heat transfer coefficients along different planes of a vane and a rotor blade on the endwall and blade tip. The effects of thermal barrier roughness was also quantified and the results simulated using the commercially available software called STAR-CD©. Ling et al. suggested a procedure to minimize lateral conduction effect in heat transfer experiments using liquid crystal techniques and then demonstrated it on systems with film cooling. A correction was used to accurately predict heat transfer data for transient measurements. This lateral conduction problem is negligible and can be completely omitted by the usage of TSP.

Recently, Ahn et al. [83] and [84] investigated the film cooling effectiveness on the leading edge of a rotating blade for two row and three row coolant injection on the leading edge at design and off-design rotating conditions. Off-design conditions were found to significantly alter the film coolant traces on the leading edge. The same experimental facility has been used in this paper with a new turbine rotor to allow for stator-rotor gap and downstream discrete hole cooling.

Lung Fu et al. [85] investigated the heat transfer in a 2-pass rectangular rotating channel to simulate internal cooling passages in a gas turbine blade. 45° and 90° roughened ribs were positioned along the rib walls close to the leading and trailing walls and heat exchange was determined for Reynolds number between 5000 and 40000. They found that rotation caused the heat transfer differential between the leading and the trailing walls to decrease for the second pass. Very few papers are available which characterize the flow in a ribbed internal channel. Miin Liou [86] used laser Doppler velocimetry to present results of flow in a ribbed rotating internal channel. Ribs were arranged at 45° to each other and were of square cross section. Correlations between rib roughness and rotation and their effects on Nusselt number distributions were presented. The rotation affected the development of the flow regime and delayed the evolution of fully developed flow within the channel.

Lacovides et al. [87] presented the results of experiments performed to study impingement cooling in a rotating semi-cylindrical passage. Rotation was found to decrease heat transfer, minimising the magnitudes of the primary and secondary peaks that existed close to the injection point and mid way between two injection locations for stationary case. LDA and PIV tests of the flow show that rotation accelerates the spreading of the coolant and thereby decreasing its effectiveness.

Wright et al. [88] investigated the effects of rotation on heat transfer for a ribbed rectangular channel. Two different combinations of ribs were studied for a channel aspect ratio of 4:1. The rotation number was varied between 0 and 0.15 for a range of Reynolds numbers. It was found that the discrete V and W ribs had the optimum thermal performance for minimum pressure loss. Heat transfer was enhanced for the narrow channel along the leading and trailing walls.

Vortex or latticework cooling effectiveness measurements were made by Acharya et al. [89]. For the channel they studied no significant enhancement in Nusselt numbers were observed due to rotation except at lower Reynolds numbers. Latticework cooling was found to be as effective as the conventional rib turbulated internal cooling. Effects of high rotation numbers on fluid flow and heat transfer in a curved duct was investigated by Sleiti and Kapat [90]. Their simulation results based on Reynolds stress model showed that the averaged Nusslet number of all the four walls of the channel at high rotational numbers was similar to that observed for low rotational numbers, increasing linearly with increasing rotation

numbers. Increasing the coolant density decreased the heat transfer as compared to the lower rotational number cases.

1.2.5 Heat Transfer and Film Cooling Research on Rotating Platform

Blair [91] studied the heat transfer on the pressure and suction sides as well as on the hub platform surface for a rotating turbine model. Enhanced heat transfer was observed on the platform due to the secondary flow effects. The effects of coolant swirl of film on mainstream flow and thereby heat transfer in a rotating cavity was investigated by Karabay et al. [92]. They predicted that when the coolant moment ratio is zero, the ratio of coolant tangential velocity to the rotor tangential velocity is a critical value and the Nusselt number under those conditions is minimal for coolant injection.

As can be seen, the literature for rotating turbine heat transfer and film cooling is scarce and designers have limited information when it comes to optimising cooling for rotating components. The dearth of material is even more for the rotating platform case which has hardly been dealt with previously. In view of this, the following section offers details as to the scope and objectives of the current investigation.

2. RESEARCH PROGRAM AND OBJECTIVES

There is very limited experimental data available for rotating heat transfer and film cooling in the literature for gas turbines. Further, the information regarding heat transfer and film cooling on the turbine platform under rotating conditions is few and far between. Therefore, there is a need to study the detailed turbine platform heat transfer and film cooling under engine representative flow and rotating conditions. This investigation attempts to provide the designers with reliable data for improving the cooling performance and thermal efficiency of gas turbines by optimising coolant distribution on the rotating platform. In addition, detailed measurements of the mainstream flow upstream of the rotor platform under study will be gathered to quantify the nature of coolant flow and understand the influence of mainstream flow on coolant distribution on the platform surface. With a better understanding of the flow physics and heat transfer distributions on the rotating blade platforms, it will be possible to reduce the amount of air extracted from the compressor for the purpose of turbine blade cooling. Improving the platform cooling would allow for increase in rotor inlet temperatures and thereby enhancing the system thermal performance. To meet the above stated objectives, the following aerodynamics, film cooling effectiveness and heat transfer results were performed:

2.1 Film Cooling Effectiveness

- To study rotational effects on stator-rotor gap coolant injection the following cases were studied on the rotor platform:
    - MFR = 0.5%, 1.0%, 1.50% and 2.0%
    - Rotational speeds = 2400rpm, 2550rpm and 3000rpm
- To study rotational effects on downstream discrete hole coolant injection the following cases were investigated on the rotor platform:
    - M_{hole} = 0.5, 0.75, 1.00, 1.25, 1.50 and 2.00

  - Rotational speeds = 2400rpm, 2550rpm and 300rpm

- Combined upstream stator-rotor gap and downstream discrete hole coolant injection were studied for the rotor platform for the following cases:
  - MFR = 1.00%
  - M_{hole} = 0.75, 1.00 and 1.25
  - Rotational speeds = 2400rpm, 2550rpm and 3000rpm

2.2 Heat Transfer Measurement

- To study rotational effects on stator-rotor gap coolant injection the following cases were studied on the rotor platform:
  - MFR = 0.5%, 1.0%, 1.50% and 2.0%
  - Rotational speeds = 2400rpm and 2550rpm
- To study rotational effects on downstream discrete hole coolant injection the following cases were investigated on the rotor platform:
  - M_{hole} = 0.0, 0.75, 1.00 and 1.25
  - Rotational speeds = 2400rpm and 2550rpm

2.3 Aerodynamics

- Aerodynamic measurements were performed at station 2 along the stator-rotor gap plane for MFR for
  - MFR = 1% and varying the rotor speeds between 2200 and 2550rpm at intervals of 50rpm
  - 2550rpm and MFR of 0, 0.25%, 0.50%, 1% and 1.5%
- Circumferential and radial interstage aerodynamic measurements were performed at stations 3, 4 and 5 at reference rotor speed of 2550rpm.

3. EXPERIMENTAL FACILITY

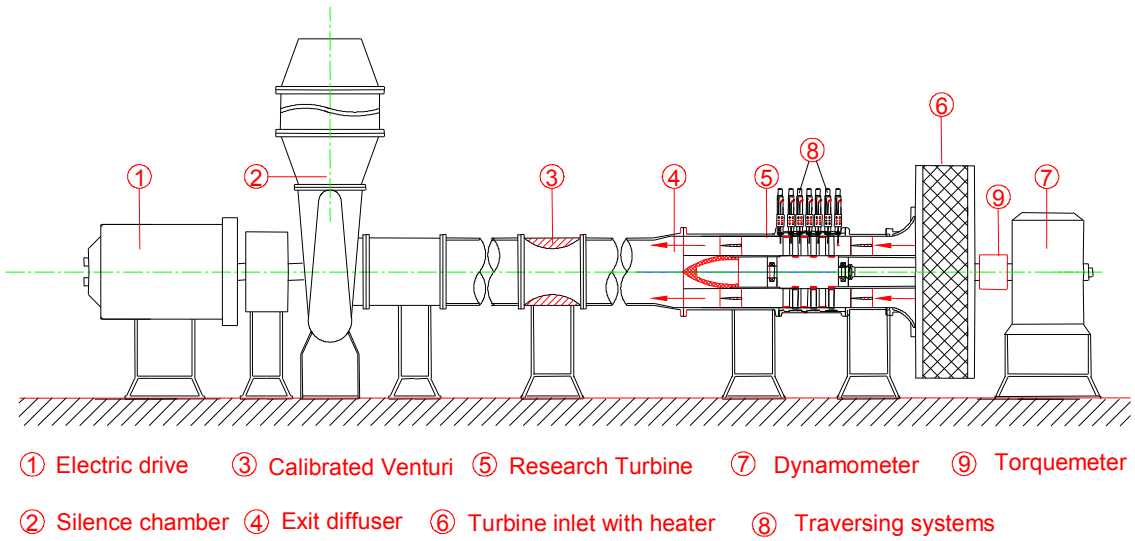

Figure 3: Existing Turbine Research Facility, (Schobeiri et al. [1] and [2]).

The experimental investigations have been carried out in a three-stage turbine research facility at the Turbomachinery Performance and Flow Research Laboratory of Texas A&M University. The turbine is the core component of the *TPFL*-research facility designed by Schobeiri et al. [1] in 1997 to address aerodynamics, efficiency, performance and heat transfer issues of high pressure (HP), intermediate pressure (IP), and low pressure (LP) turbine components. Detailed aerodynamic, efficiency, loss and performance measurements were carried out to verify and document the efficiency and performance of a high efficiency 3-D, bowed blading [1]. To compare the results of the investigations reported in [1] with those for 2-D cylindrical blades, detailed aerodynamic measurements were conducted and summarized in the subsequent reports [2]and [3].

The overall layout of the test facility is shown in Figure 3. It consists of a 300HP electric motor connected to a frequency controller which drives the compressor component. A three-stage centrifugal

compressor supplies air with a maximum pressure difference of 55kPa and a volume flow rate of $4m^3/s$. The compressor operates in suction mode and its pressure and volume flow rate can be varied by a frequency controller operating between 0 to 66Hz. A pipe with a transition piece connects the compressor to a Venturi mass flow meter used to measure the mass flow through the turbine component. The exit diffuser serves as a smooth transition piece between the turbine component and the Venturi, which is used for mass flow measurement. The three-stage turbine has an automated data acquisition system for detailed flow measurement at each blade row location. The turbine inlet has an integrated heater that prevents condensation of water from humid air expanding through the turbine during the test. The turbine shaft is connected through a flexible coupling with one end of a high precision torque meter that has a maximum rotational speed of 8500rpm and a maximum torque rating of 677.9N-m. The other end of the torque meter is coupled via a second flexible coupling with an eddy current low inertia dynamometer with a maximum power capacity of 150kW and a maximum torque of 500Nm.

Table 1: Turbine dimensions and operating conditions.

Stage no., N	3	Mass flow	3.728 kg/s
D_t	685.8mm	D_h	558.8mm
Reference speed	2550 rpm	Speed range	2400 to 3000 rpm
Inlet pressure	101.356 kPa	Exit pressure	71.708 kPa
Blade height	63.5 mm	Power	80-110 kW
Blade no.	Stator 1 = 56	Stator 2 = 52	Stator 3 = 48
Blade no.	Rotor 1 = 46	Rotor 2 = 40	Rotor 3 = 44
α_{v2}	19°	ϕ	0.353
β_{v3}	161°	λ	1.0
α_3	110°	r	0.5

3.1 Interstage Instrumentation

The turbine component shown in Figure 3 is a three-stage air turbine with the dimensions and operating conditions specified in Table 1. To achieve a high degree of versatility, the turbine was designed with a casing that incorporates stator rings. It also incorporates three T-rings for sealing the three 90º circumferential traversing slots, as seen in Figure 4.

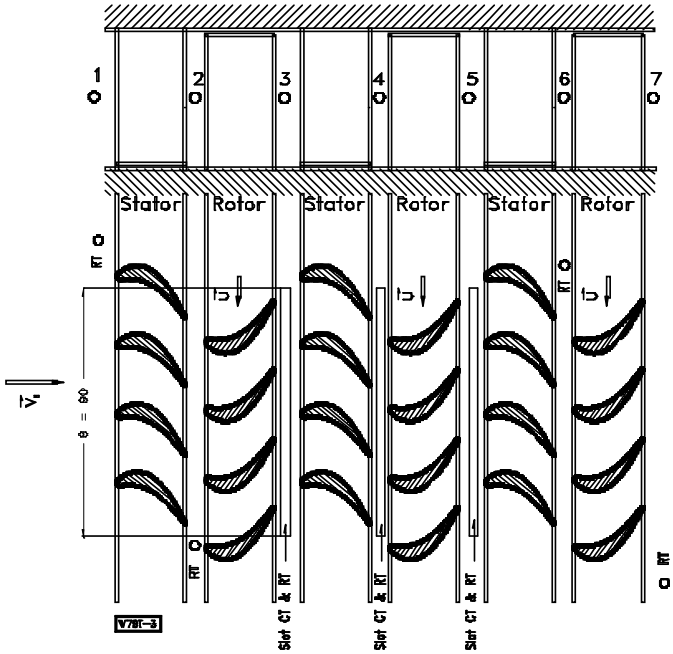

Figure 4: Turbine Cross Section Showing T-ring Slots for Circumferential Interstage Aerodynamic Measurements, (Schobeiri et al. [1] and [2]).

The sealed T-rings move circumferentially inside the slots and effectively prevent the leakage of mainstream mass flow through the slots. As shown in Fig. 3, three five-hole probes are mounted on three traversing systems with decoder and encoder for accurate probe positioning. The traverse in the radial

direction spans from 1mm below the hub diameter to 1mm above the blade tip. Each of the radial and circumferential traverses also has individual stepper motors which allow for accurate alignment of the probes to the direction of flow near the rotor hub and tip during actual data acquisition. The controllers to these stepper motors are connected to the same aerodynamic data acquisition computer through COM ports where the control program to rotate the motors, provided by IMS, is also available. The required operational commands and procedure for the controller is provided extensively in the user manual for the controllers. These three stepper motors along with the three radial and one circumferential traverse make up the high precision 7-axes probe traverse system used in the interstage aerodynamics measurement.

For the performance instrumentation, combined total pressure, total temperature rakes are used upstream of the first stator row and downstream of the last rotor row. At the inlet, the rakes were located radially at 45°, 135^0, 225°, and 315°. Each rake consists of 4 total pressure and 3 total temperature probes that are equidistantly distributed in the radial direction. The total pressure probes are of the Pitot tube types, and the total temperature probes are calibrated J-type thermocouples. To reduce the wake thickness originating from the trailing edge of the inlet rakes, the rakes are shaped aerodynamically with a round leading edge and a sharp trailing edge.

The exit rakes are located radially with the same spacing as the inlet rakes, but offset to them in order to prevent the interference with the inlet rake wakes. Wall static pressure taps are arranged at the top and bottom half of the main casing and on the T-rings (Figure 4), as well as on the stator rings. In addition, total temperature and pressure probes are mounted on the leading edge stagnation points of two diametrically opposed stator blades of the second and third stator rows. The turbine facility has the capability of radially traversing the flow field at stations 1 through 7 and circumferentially and or radially traversing at stations 3, 4, and 5. The data from the traversing is used to generate the total and static pressure contours, velocity components, flow angles and the span wise distribution of total pressure loss coefficients and the efficiency for each row. Three L-shaped five-hole Pitot probes were used for this purpose. The first and the third probes were installed at stations 3 and 5 and were calibrated at low subsonic Mach number (M = 0.1), while the second one installed at station 4 was calibrated taking into account any small compressibility effects due to the moderate subsonic Mach number of M = 0.3.

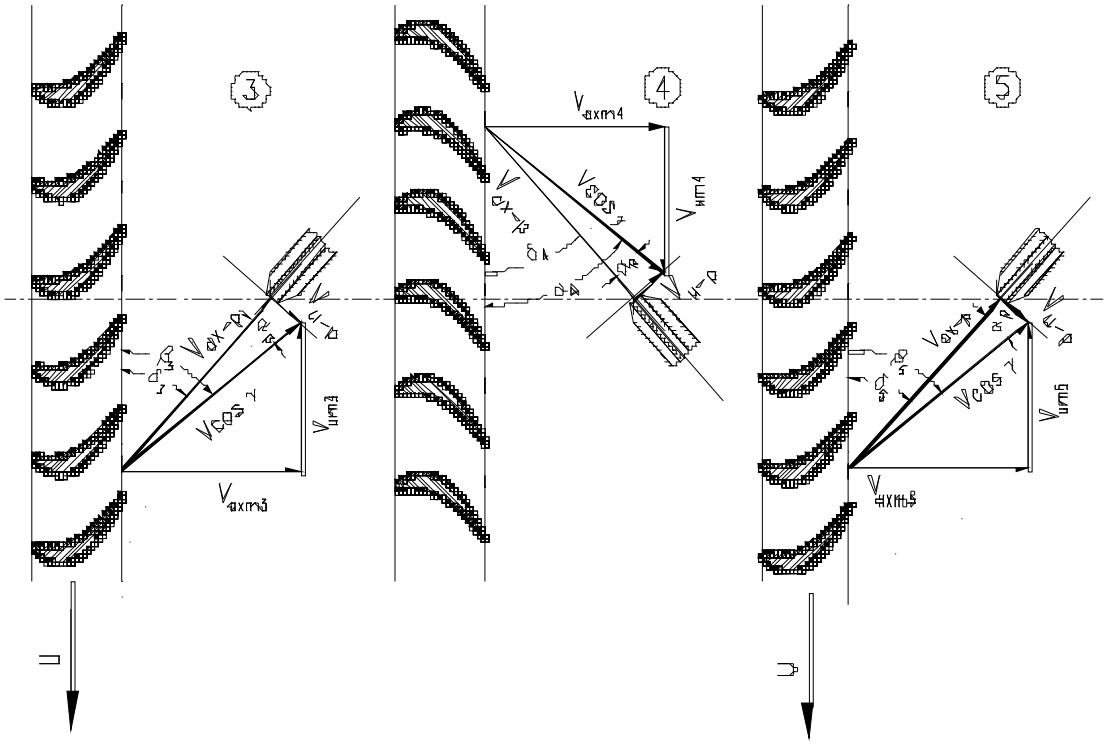

Figure 5: Schematic of the 5 Hole Probe Adjustment Angle at Station 3, 4 and 5, (Schobeiri et al. [1] and [2]).

Five-hole probes are independently calibrated in a fully automated calibration facility. Each probe is placed in an angular indexing mechanism and is pitched and yawed through the range of angles (-20^0 to 20^0 in pitch and -20^0 to 20^0 in yaw) in 1^0 increments. The calibration facility probe indexing mechanism uses two stepper motors that are computer controlled to achieve a very fine angle resolution. A computer algorithm called TURBOPROBE, which creates a user-specified grid of pitch and yaw angles, is used to control these stepper motors. The same program also records the pressures from the PSI- 9016 pressure scanner and stores the pressures from the five-hole probe with the corresponding pitch and yaw angles and the calibration nozzle total pressure into a data file. This data file is then used to create the calibration surfaces for the specific probes that are later used to determine the velocity components and vectors at

stations 3, 4, and 5 of the turbine. Further information if necessary can be found in [2] and Sharef Abdel Fatteh [93]. The absolute and relative flow angles and velocity components of the turbine rows are calculated by implementing the probe adjustment angle for each of the three probes at stations 3, 4 and 5 respectively (Figure 5).

To determine the film cooling effectiveness under rotating conditions for leading edge film cooling (Ahn et al. [80], [84]), the turbine rotor was modified to integrate the coolant loop into the downstream section of the hollow turbine shaft and into the cylindrical hub cavity. The same rotor was not compatible for the platform cooling experiments needed for the current investigation hence, a new rotor with the ability to provide cooling on the rotor platform surface was designed, manufactured and installed. Further information regarding the instrumentation and test facility is provided by [93].

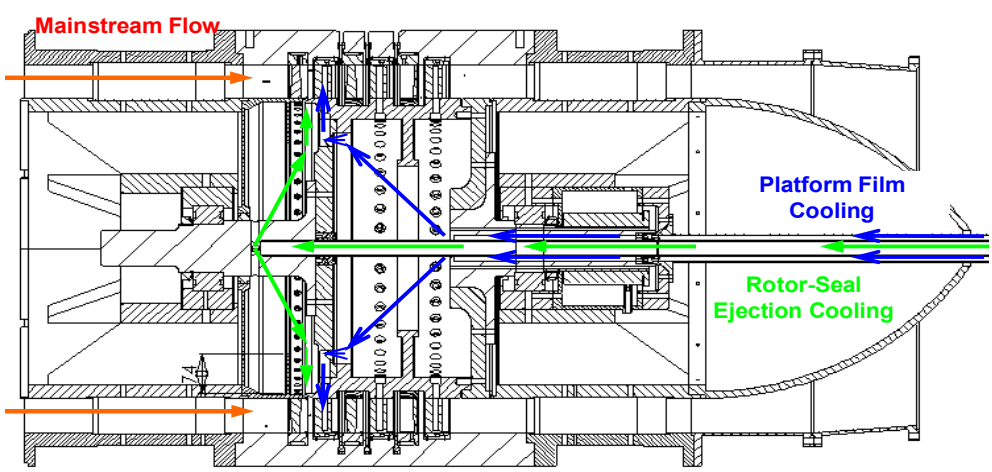

Figure 6: Section View of the Modified Stator-Rotor Turbine Assembly for Stator-Rotor Purge Flow and Platform Film Cooling.

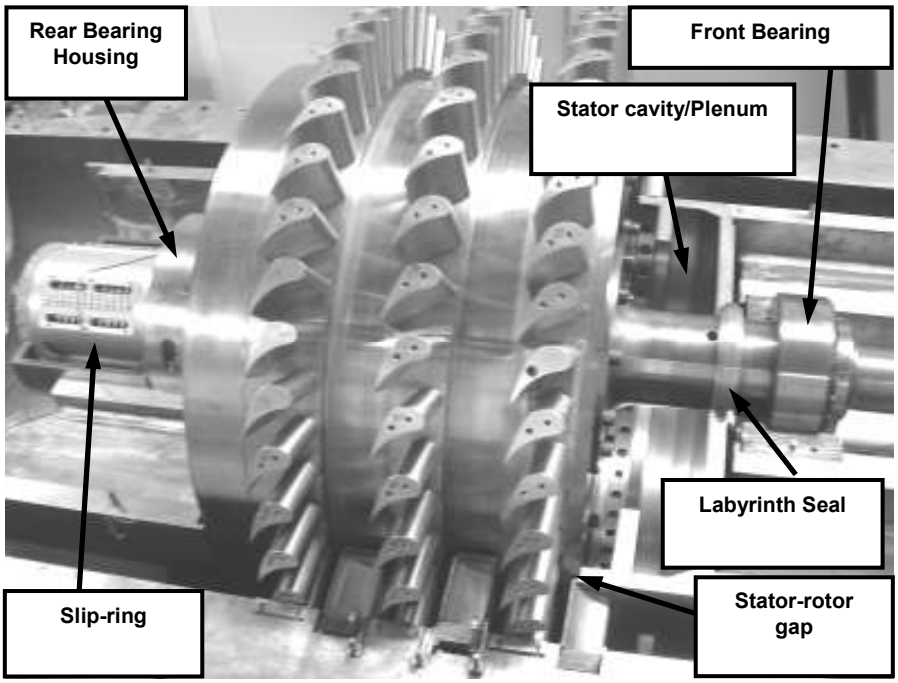

Figure 7: Turbine Components with the 24-Channel Slip Ring and Upstream Stator-Rotor Gap Cavity.

3.2 New Turbine Component Design

A completely new advanced three-stage turbine component as shown in Figure 6 and Figure 7 was designed to replace the one discussed in [[1], [2], [3]] and [[80], [84]]. In addition to the tasks performed by the old rotor, the new one was designed to operate at high speeds of 8500rpm close to the transonic range. The first critical speed for vibration for the new rotor at its natural frequency occurs at 6500rpm. Two independently controlled, concentric coolant loops provide the necessary mass flow for film cooling experiments. The outer loop supplies coolant for film cooling experiments in the blade passage section close through discrete coolant holes. The inner loop ejects coolant from a circumferential gap between the first stage stator and rotor and provides platform cooling near the blade leading edge. A concentric jet exits this circumferential gap at an angle of 25° into the mainstream (Fig. 8). The maximum normal gap width is

designed to be 3mm. However, it can be decreased to up to 0.5mm by translating the entire rotor towards the front bearing. For the current study it was set to 2.3mm.

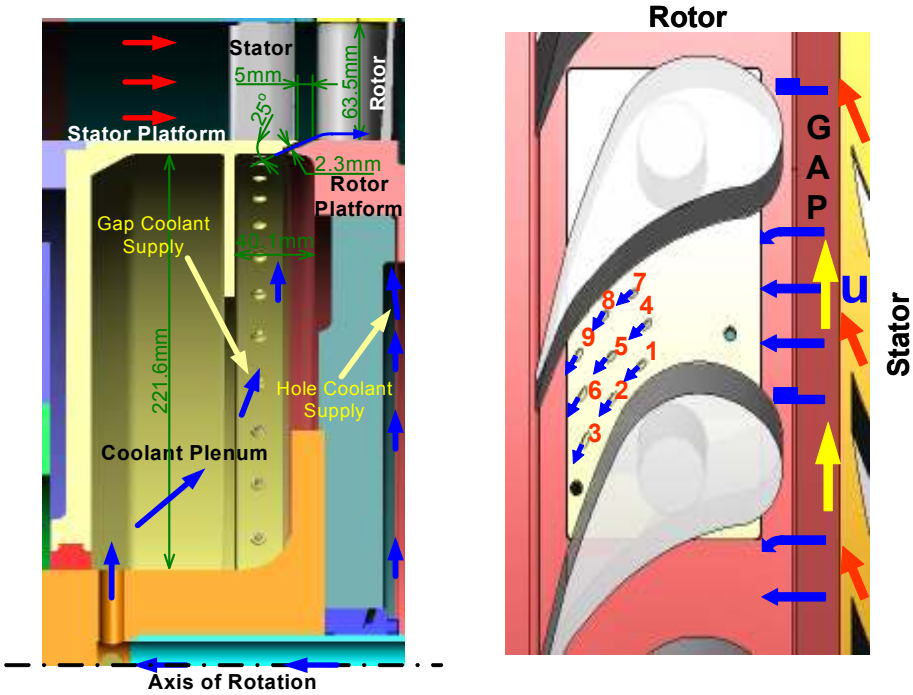

Figure 8: Detailed Views of Stator-Rotor Gap and Downstream Discrete Holes.

The axial stator-rotor gap for the first stage was measured at 5mm. Similar to the optimization of the trailing edge slot ejection described in detail by Schobeiri [94] and Schobeiri and Pappu [95], the reduction of slot width is instrumental in establishing an optimum ejection ratio while keeping the cooling mass flow constant. Figure 8 also shows the detailed view of the downstream discrete holes. Nine holes of Ø1mm were machined at complex angles (as shown in Table 2 on p. 86) mid-way through the blade passage to enable cooling in the endwall passage zone left uncovered by the upstream injection. A printed circuit board constant flux heater (Figure 9) designed to match the profile of the rotor blade passage was

also mounted on the first stage rotor platform for conducting heat transfer measurements. Due to design constraints, the heater element begins about 3mm downstream of the blade leading edge and extends downstream up to 70% of the suction surface. Though this heater set-up does not cover the entire platform of the blade passage, the effects of coolant ejection through upstream gap and downstream holes can be clearly seen and is found sufficient to quantify the effects of rotation on platform heat transfer. The downstream discrete holes are also machined on to the heater corresponding to the holes already on the rotor platform. The insert using which the heater is assembled on the rotor hub is shown in (Figure 10). Three thermocouples each are mounted near the leading edge and the trailing edge underneath the heater, the insulation and the metal insert to calculate heat loss due to conduction during heat transfer experiments. Other thermocouples located around the rotor passage monitor the mainstream and coolant temperatures.

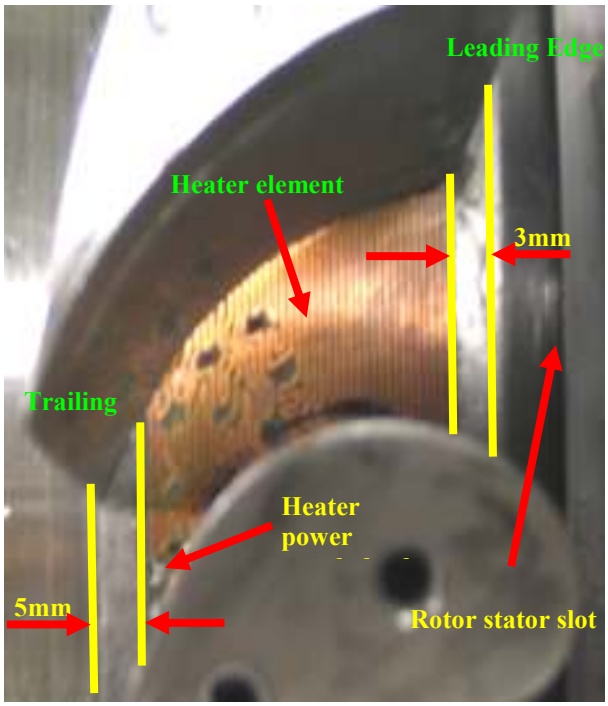

Figure 9: Heater Element as Mounted on the Rotor Platform Blade Passage.

The blades attached to the new rotor were taken from the rotor described in [[1], [2], [3]] and also used in [[80], [84]]. They are typical HP-turbine blades used in steam turbines characterized by a relatively thick leading edge portion. This particular blade design allows reducing the total pressure losses due to the adverse off-design incidence changes caused by part-load operation. Thus, these blades are not characteristic of power generation or aircraft gas turbines. Although the blade geometry does not represent typical gas turbine blade geometry, it provides the basic features to extract information relevant to gas turbine design community. These features are (a) stator-rotor unsteady interaction, (b) blade and platform rotation and consequent exposure of the platform boundary layer to centrifugal and coriolis forces, and (c) the flow acceleration. Except for the last feature (c), none of the above features can be simulated in a cascade investigation.

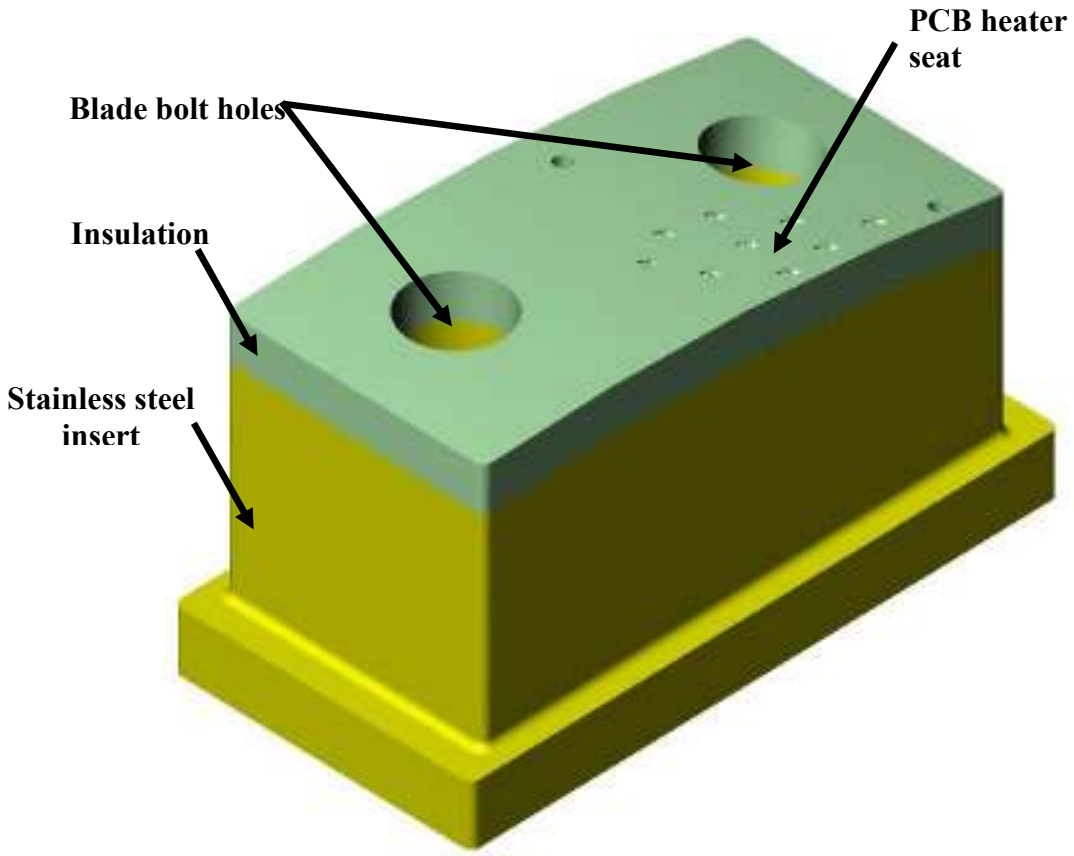

Figure 10: Insert Used to Mount Heater on the Rotor Platform.

To ensure that minimal coolant escapes through the rotary-stationary interfaces, the internal and external loops were sealed with labyrinths. The teeth spacing and the tip clearance were taken using the design instructions detailed by Schobeiri [7]. A 24-channel slip-ring is mounted to the rear of the shaft to transfer temperature data from thermocouples from the rotating frame to the data acquisition system and also to power the heater used for the heat transfer measurements.

4. EXPERIMENTAL PROCEDURE

4.1 Aerodynamic Measurement Theory and Analysis

Interstage aerodynamic measurements are performed along the first stage rotor exit, second stage stator exit and third stage rotor exit using miniature 5-hole probes. The circumferential and radial traverse facility enables comprehensive data acquisition at these locations. To reduce the error in measurements near the blade tip and hub where the flow is highly complex, additional stepper motor controls are provided to allow for accurate adjustment of the miniature 5-hole probes in line with the mainstream flow. Five hole probes are calibrated in order to be able to correlate the measured pressures with flow velocity and direction. The calibration is highly dependent on flow velocity and therefore the three probes to be used are calibrated at velocities similar to those encountered within the engine as seen from previous tests by [1]. As mentioned earlier, the probes are calibrated at Mach numbers of 0.1 and 0.3 in a calibration facility using a non-nulling technique. From this calibration data, five probe coefficients are calculated using the method suggested by Rubner and Bohn. These coefficients are then plotted against the probe pitch and yaw angles to obtain the following functions:

$$\alpha = f_1 \, [(P_3-P_1)/(P_m-P)] \tag{1}$$

$$\gamma = f_2 \, [(P_2-P_4)/(P_m-P)] \tag{2}$$

$$[(P_m-P)/(P_t-P)] = f_3(\alpha, \gamma) \tag{3}$$

$$[(P_m-P_3)/(P_t-P)] = f_4(\alpha, \gamma) \tag{4}$$

$$[(P_m-P_1)/(P_t-P)] = f_5(\alpha, \gamma) \tag{5}$$

The calibration of the 5 hole probe is complete once these functions relating the five probe pressures, the total and static pressures with the flow angles are determined. These calibration functions replace the previously employed calibration functions based on Morrison et al. [96] in the aerodynamic data analysis program of Schobeiri et al. [1]. An iterative procedure, assuming $P_i = 0.8\ P_m$, is then used to determine the actual pressures and flow angles in the research turbine. Thus, by measuring the pressures within the turbine using a 5-hole Pitot probe, the unknown velocity field in machine coordinates can be determined using the calibration functions and the procedure described in [1], [2] and [93].

4.2 Film Cooling Effectiveness Measurement Theory and Data Analysis

Data for film cooling effectiveness was obtained by using the PSP technique. PSP is a photo-luminescent material which emits light when excited, with emitted light intensity inversely proportional to the partial pressure of oxygen. This light intensity can be recorded using a CCD camera and can then be calibrated against the partial pressure of oxygen. Details of using PSP for pressure measurement are given in McLachlan and Bell [97]. The image intensity obtained from PSP by the camera during data acquisition is normalized with a reference image intensity taken under no-flow conditions. Background noise in the optical setup is removed by subtracting the image intensities with the image intensity obtained under no-flow conditions without excitation. The resulting intensity ratio can be converted to pressure ratio using the previously determined calibration curve and can be expressed as:

$$\frac{I_{ref} - I_{blk}}{I - I_{blk}} = f\left(\frac{\left(P_{O_2}\right)_{air}}{\left(P_{O_2}\right)_{ref}}\right) = f\left(P_{ratio}\right) \tag{6}$$

where I denotes the intensity obtained for each pixel and $f\,(P_{ratio})$ is the relation between intensity ratio and pressure ratio obtained after calibrating the PSP.

Calibration for PSP was performed using a vacuum chamber at several known pressures varying from 0 to 1atm with intensity recorded for each pressure setting. The same optical setup was chosen for calibration as well as for data acquisition during the experiments. A schematic of the calibration setup is shown in Figure 11.

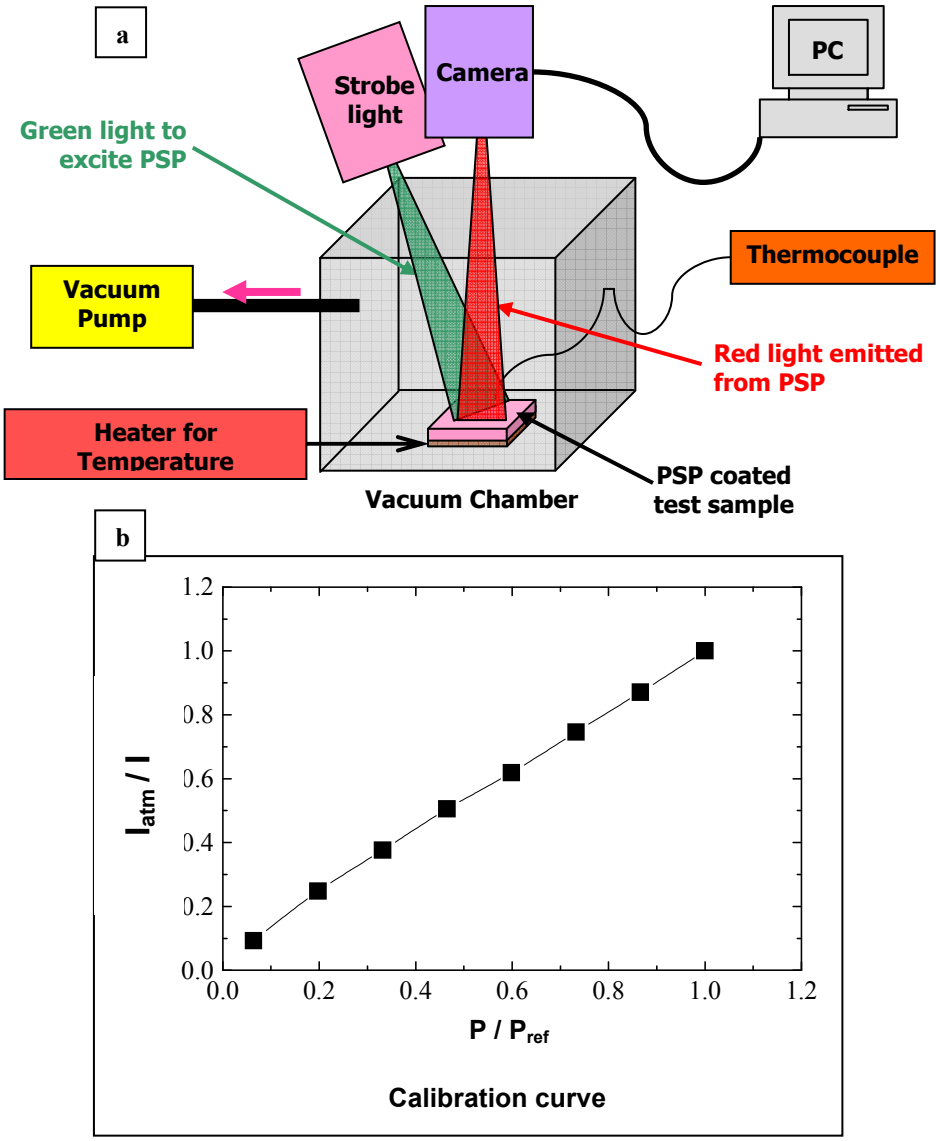

Figure 11: Typical Pressure Sensitive Paint Calibration Setup and Calibration Curve.

(a) PSP Calibration Setup.
(b) PSP Calibration Curve.

PSP is sensitive to temperature with higher temperatures resulting in lower emitted light intensities. Hence, the paint was also calibrated for temperature. It was observed that if the emitted light intensity at a certain temperature was normalized with the reference image intensity taken at the same temperature, the temperature sensitivity can be removed. Hence, during data acquisition, the reference image was acquired immediately after the experiment was completed to avoid errors related to temperature variation. Reference images were acquired after the rotor came to a halt and the temperature change from loaded to stationary condition was small enough to disregard its effect on PSP measurement. Flow and surface temperatures were monitored by a thermocouple placed 2mm above the surface close to the suction side and by another thermocouple placed underneath the platform surface respectively. The thermocouples were wired through a slip-ring and connected to a digital readout. To obtain film cooling effectiveness, air and nitrogen were used alternately as coolant. Nitrogen which can be assumed to have the same molecular weight as that of air displaces the oxygen molecules on the surface causing a change in the emitted light intensity from PSP. By noting the difference in partial pressure between the air and nitrogen injection cases, the film cooling effectiveness can be determined using the following equation.

$$\eta = \frac{C_{mix} - C_{air}}{C_{N_2} - C_{air}} = \frac{C_{air} - C_{mix}}{C_{air}} = \frac{\left(P_{O_2}\right)_{air} - \left(P_{O_2}\right)_{mix}}{\left(P_{O_2}\right)_{air}} \quad as \quad C \; \alpha \; P_{O_2} \tag{7}$$

where C_{air}, C_{mix} and C_{N2} are the oxygen concentrations of mainstream air, air/nitrogen mixture and nitrogen on the test surface respectively. The definition of adiabatic film cooling effectiveness is

$$\eta = \frac{T_f - T_m}{T_c - T_m} \tag{8}$$

The accuracy of the PSP technique for measuring film-cooling effectiveness has been compared by Wright et al. [92] on a flat plate with compound angled ejection holes using several measurement techniques such as steady and transient liquid crystal, IR camera and using a foil heater with thermocouples. Results were obtained for a range of blowing ratios and show consistency with each other. Wright et al. [92] found that IR, TSP as well as PSP gave effectiveness results within 15% of each other. Larger uncertainties for heat transfer techniques such as IR and TSP methods were observed due to lateral conduction in the flat plate.

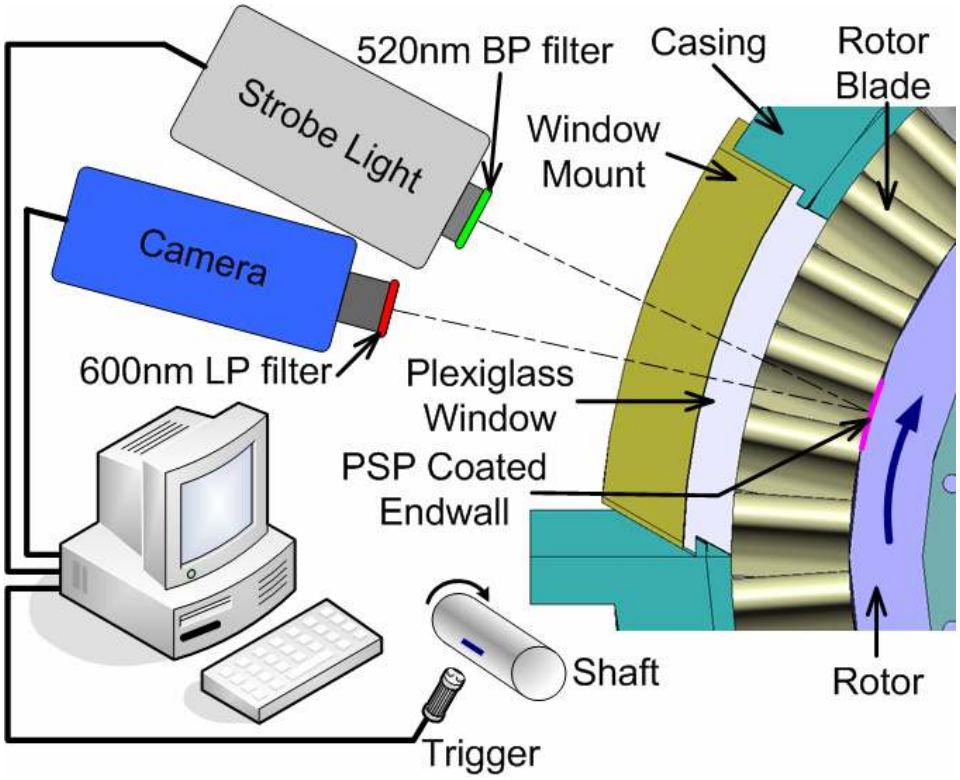

Figure 12: Optical Components Setup for the Model Turbine and PSP.

4.2.1 Data Acquisition Procedure for Film Cooling Effectiveness Measurements Using PSP Technique

The platform passage under investigation was layered with PSP using an air brush. This coated surface was excited using the strobe light fitted with a narrow bandpass interference filter with an optical wavelength of 520nm. Upon excitation from this green light, the PSP coated surface emitted red light with a wavelength higher than 600nm. A 12-bit scientific grade CCD camera (High speed Sensicam with CCD temperature maintained at –15°C using 2-stage Peltier cooler) was used to record images and was fitted with a 35mm lens and a 600nm longpass filter. The filters were chosen to prevent overlap between the wavelength ranges such that the camera blocked the reflected light from the illumination source and measured only the emitted light from the PSP. A schematic of the optical components setup used in data acquisition is depicted in Figure 12. The camera and the strobe light were triggered simultaneously by an optical sensor at a specific angular location on the shaft corresponding to the area of interest for every rotation. By detecting the same angular position, the camera was able to view the same region of interest every time, making it possible to average the image intensities without blurring the information. A minimum exposure time of 16μs was used for image capture from the camera. Estimated rotor movement during image capture at 2550rpm, for 16μs exposure time was 1.15mm. A total of 200 TIF images were captured for each experiment with air and nitrogen being injected separately and the pixel intensity recorded for both cases. A MATLAB® code given in appendix D was used to average the images and convert the digital images into intensity values. A binning of 4 was used on the camera to provide optimum pixel resolution and sufficient emitted intensity by the PSP and TSP to acquire quality data. This corresponded to approximately 0.69mm per pixel on the rotor platform. Further, a FORTRAN code (Appendix D) was used to convert these pixel intensities into pressure using the calibration curve and then into film cooling effectiveness based on equation (7). The coolant flow rate was set using a rotameter based on prior calculation for the desired mass flow ratio. The coolant was heated to the same temperature as mainstream air (46°C) before injection through the coolant loops using external heaters. Uncertainty

calculations were performed for a confidence level of 95% and are based on the uncertainty analysis method of Coleman and Steele [56].

4.3 Heat Transfer Coefficient Measurement Theory and Analysis

Like PSP, temperature sensitive paint (TSP) is also comprised of luminescent molecules suspended in a polymer binder. However, the photophysical process associated with TSP is thermal quenching, rather than oxygen quenching. Unlike with PSP, the polymer binder is not oxygen permeable. Therefore, the luminescence intensity of the TSP is related only to temperature, and is not a function of pressure (unlike the reverse relationship observed with PSP). Like PSP, the luminescent molecules in the TSP must be excited with the absorption of a photon. The molecules return to their ground state with the emission of the photon at a longer wavelength. Increasing the temperature of the luminescent molecules triggers their return to ground state (releasing the photon through a radiationless process) [92]. Temperature of the surface on which it is coated determines the number of molecules returning to ground state causing variations in emitted light intensity at different temperatures. Therefore, the emission intensity from molecules at elevated temperatures is lower than the emission of molecules at relatively lower temperatures. This photophysical process wherein the luminescent molecules emit light based on the surrounding temperature is known as thermal quenching.

Similar to the use of PSP, a data image, a reference image and a black image are acquired for the TSP measurements. Typically, the reference condition is set at the room temperature at which the experiments are performed. However, for cryogenic applications the reference temperature may be much lower. With the reference condition, and the black image used to eliminate the background noise from the optical components, the emission intensities are related to the surface temperature as shown in Equation 9.

$$\frac{I(T) - I_{blk}}{I(T)_{ref} - I_{blk}} = f(T) \tag{9}$$

TSP is calibrated to determine the relationship between the emission intensity and the surface temperature. Calibration is performed using a heated copper block with a thermocouple attached to

monitor the specimen temperature. The copper block is coated with the TSP and positioned between the same excitation light and CCD camera used to acquire temperature data on the experimental facility. The paint is calibrated for a temperature range of 24ºC to 75ºC corresponding with the temperatures observed in the experimental facility and used for PSP experiments. Emission intensities are recorded (coupled with black images) at pre-determined temperatures and a correlation between intensity and temperature is identified. The TSP calibration curve is shown in appendix H along with the MATLAB® program used for converting images into intensities. A simple EXCEL® spreadsheet can be used to plot the calibration curve of intensities against temperature.

4.3.1 Data Acquisition Procedure for Heat Transfer Measurements Using TSP Technique

The experimental setup used for temperature measurements is similar to the one used for the PSP technique. For this study, TSP is used to measure the steady state surface temperature. The heater fixed to the platform, heats the rotor platform surface by supplying the surface with uniform heat flux. A digital power supply is used to supply power to the heater coils through the slip-ring. Care must be taken to ensure that the heater is powered up only when there is air flow over it. Supply power should not exceed the power rating of the heater which in this case was 16W. For acquiring temperature data, the filters on the camera are changed accordingly as recommended by the TSP supplier. For minimum error during temperature measurements using TSP, the temperature difference between the heater surface and mainstream flow was maintained between 10ºC to 20ºC.

During the actual film cooling experiment with heated platform, three images are acquired: black image (no flow, no excitation light), reference image (no flow, with excitation light), and air image (mainstream and coolant flows, with excitation light). Similar set of pictures are taken again but with zero power supplied to the heater to determine the adiabatic wall temperatures under cooling. The reference image must be acquired at the same temperature of the reference image measured during calibration. With a temperature being recorded at every pixel in the viewing window, detailed distributions of the temperature and heat transfer coefficients can be obtained on the rotor platform.

As the film coolant mixes with the mainstream temperature variations are created on the platform. This variation is noted by the change in emitted intensity from the TSP by the high speed camera used for PSP measurements. Once again the coolant and the mainstream flow temperatures are maintained the same using upstream heaters. From the measured platform surface temperatures, adiabatic wall temperatures and power input to the heater, the heat transfer coefficient on the platform can be determined from Equation 10.

$$h = \frac{Q''_{in} - Q''_{loss}}{T - T_{aw}} \tag{10}$$

where T is the platform surface temperature and T_{aw} is adiabatic wall temperature, both obtained from TSP measurements. Q''_{in} is the heat flux provided by the heater element. Q" losses to the surroundings and is defined as:

$$Q''_{loss} = Q''_{rad} + Q''_{cond} \tag{11}$$

where Q''_{loss} is the heat loss due to conduction through the insulation and the stainless steel insert and Q''_{rad} is the radiation heat flux emitted from the endwall surface. Q''_{cond} is the heat flux lost through conduction. Q''_{in}, Q''_{cond} and Q''_{rad} are defined as follows:

$$Q''_{in} = (I_{heater}^{2} * R) / (A_{heater}) \tag{12}$$

$$Q''_{rad} = \varepsilon\sigma\,(T^4 - T_{\infty}^{4}) \tag{13}$$

$$Q''_{cond} = K\,(T - T_{insulation}) \tag{14}$$

where, R is the resistance of the heater coil (R=1.4 Ω) and I_{heater} (~2.4 Amps) is the current passing through it. A_{heater} is the total surface area of the flow passage on the platform between two adjacent rotor blades. For the radiation term, ε is the emissivity of the TSP (provided by the manufacturer as 0.50) and σ is the Stefan-Boltzmann constant. Conduction effects from the heater to its mount are minimal as the mount is

made of bakelite which has a very low thermal conductivity. Data acquisition and calibration for TSP is similar to PSP except that the filter on the camera is changed to a 570nm long pass filter. For TSP as the light intensity emitted by the paint on excitation is higher than TSP, the exposure time of the camera was decreased (to 10μs) to eliminate any possible blurring of image in that small time period. The rotor spins about 0.75mm in that time span of camera exposure. The binning on the camera was again set to 4 bits.

5. RESULTS AND DISCUSSION

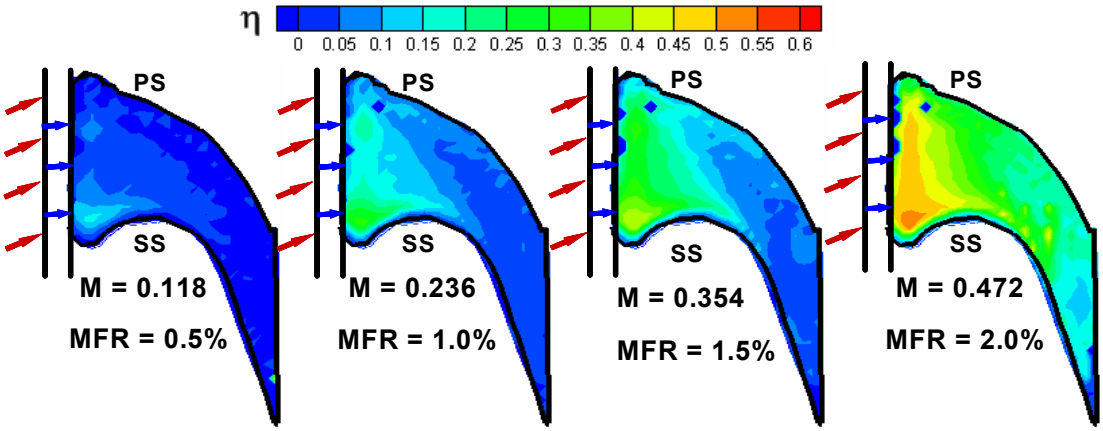

Figure 13: Film Cooling Effectiveness Distribution on the Rotating Endwall for 2550rpm.

5.1 Experimental Film Cooling Effectiveness Measurements

Significant modifications were required to the existing turbine research facility to meet the research objectives of the project. The existing facility was incapable of studying the effect of coolant ejection through the rotor platform and hence a new rotor capable of the same was installed. Therefore, the project began with the design of a new rotor platform. As shown in Figure 6, modifications of the facility allow two coolant flows to be controlled independently: ejection flow and film cooling flow. Figure 8 shows detailed views of the modified rotor platform. The turbine housing was also modified to include an optical window for data acquisition on the rotor platform. As described previously, both an excitation light and camera are needed to capture images of the area of interest using pressure and temperature sensitive paints. For every blowing ratio, an image of the platform was collected with air as coolant and also nitrogen as coolant. A reference and a black image were collected immediately after the experiments were

concluded and the film cooling effectiveness calculated after processing the data through the MATLAB® and FORTRAN programs provided in appendix D.

5.1.1 Film Cooling Effectiveness from Upstream Slot Injection

5.1.1.1 Upstream Injection at Reference Rotating Condition

Film cooling effectiveness measurements were performed for four coolant-to-mainstream mass flow ratios of 0.5%, 1.0%, 1.5% and 2.0%. Film cooling data was also obtained for three rotational speeds, 2550rpm (reference condition), 3000 and 2400rpm. Total mass flow in the engine was 3.73 kg/s and was ensured to be the same for all three rotor speeds by adjusting the blower frequency through the frequency controller. Blowing ratios for each rotating speed differ slightly as the relative mainstream velocity at the rotor inlet changes with the rotating speed.

Variation of rotational speed performed in the [42, 43] showed that the location of the leading edge stagnation line, which yielded symmetric spreading of coolant on the suction and pressure surfaces of the leading edge was at an rpm of 2550. This rotational speed was chosen as the reference rotating condition for the current investigation. The effectiveness results obtained with PSP measurements for the reference rotating condition of 2550rpm are plotted in Figure 13. The figure shows the contour plots for all four mass flow ratios tested. The contour plots also show the location of the stator-rotor slot upstream of the passage and the path of the mainstream and coolant flow. The effectiveness in the slot, as the coolant escapes through it, could not be recorded completely as the plexiglass window through which the rotor platform is observer is not wide enough.

Higher mass flow ratios result in coolant injection with higher momentum. As this momentum increases, it can be observed that the spread of the coolant as well as the effectiveness magnitudes are higher. The injected coolant is at the same density as the mainstream i.e. the coolant to mainstream density ratio is one. Hence, the injected coolant velocity is higher for higher mass flow ratios. At lower blowing ratios, the low momentum coolant is not capable of penetrating into the highly vortical secondary flow region on hub platform. It mixes with the main flow where its kinetic energy dissipates, making only a

marginal contribution to effectiveness improvement. For the lowest mass flow ratio (MFR = 0.5%), the maximum effectiveness magnitude is less than 0.2.

As the mass flow ratio increases, the coolant injection velocity increases due to which the coolant can penetrate the complex secondary flows in the passage resulting in higher effectiveness on the platform. For the highest mass flow ratio of 2%, a region of high effectiveness can be observed near the entrance of the blade passage. The effectiveness from the gap to the beginning of this high effectiveness region is slightly lower. This indicates that the coolant probably detaches itself from the surface as it exits from the gap and then reattaches as it is pushed by the mainstream towards the surface which is marked by the high effectiveness spot (at around 15% of axial chord). Effectiveness magnitudes as high as 0.6 can be observed near this reattachment spot. Smaller reattachment spots can be observed for MFR = 1.5% too. Thus, as the mass flow ratio increases, the effectiveness magnitude and its spread become larger. The same phenomenon has been recorded by several researchers mentioned earlier with studies for slot film cooling on stationary, flat as well as curved platforms. Common to all blowing ratios investigated is that the suction surface is the location of inception of the effectiveness. Major parameters instrumental in making the suction surface the inception location are: (a) the platform secondary flow, (b) the Coanda effect that helps the injected coolant attach on the suction surface and (c) the coolant injection angle.

The coolant distribution on the platform is predominantly governed by its flow characteristics. A strong pressure gradient exists within the passage from the pressure to the suction side with the static pressure near the pressure side being much higher due to lower mainstream velocities and blade curvature. The coolant traces show slightly higher effectiveness magnitudes towards the suction side near the leading edge. More coolant gets diverted away from the higher pressure stagnation region on the leading edge of the blade and finds its way towards the suction side. Effectiveness magnitudes on the pressure side begin to fade away rapidly as the coolant travels along the axial chord. As the passage vortex moves towards the suction side while gaining strength, it entrains the mainstream on the platform surface damaging the coolant film which results in a sharp drop in effectiveness magnitudes. This sudden drop gives a good indication of the path traced by the passage vortex. Similar coolant spread profiles affected by secondary

flows can be observed for stationary platform cooling through slots akin to the current design in turbine as well as vane cascades in the tests conducted by Blair [20].

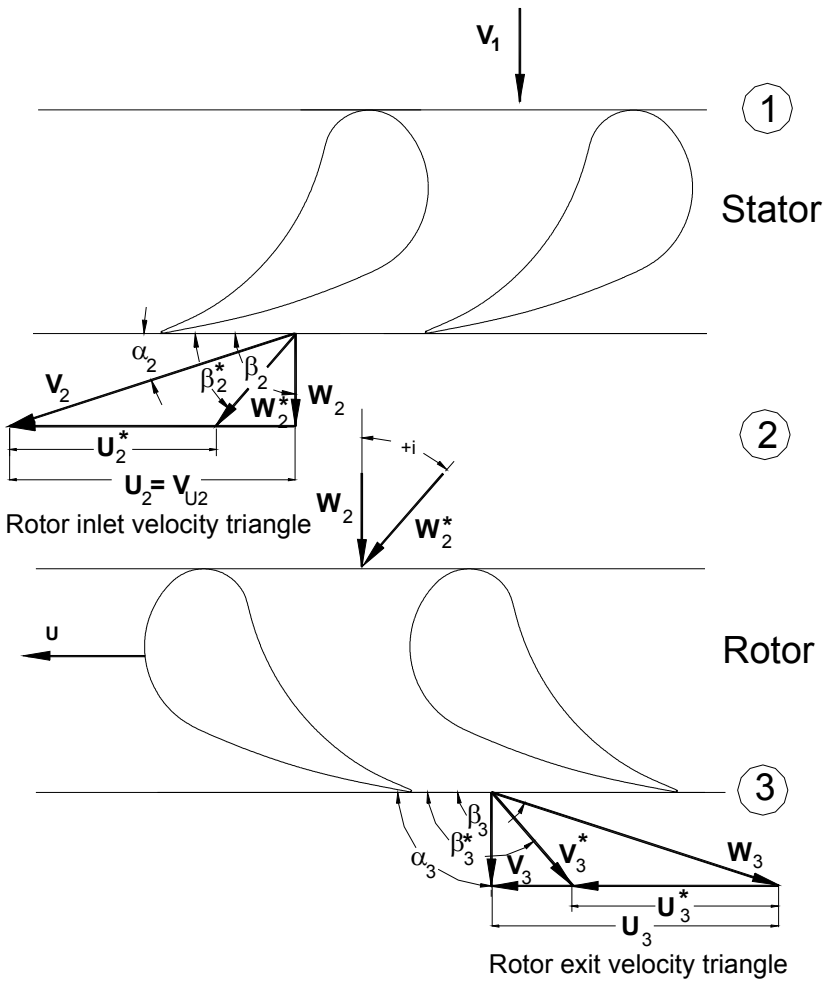

Figure 14: Velocity Triangles and Relative Inlet and Exit Flow Angles for Design and Off-Design Rotating Speeds.

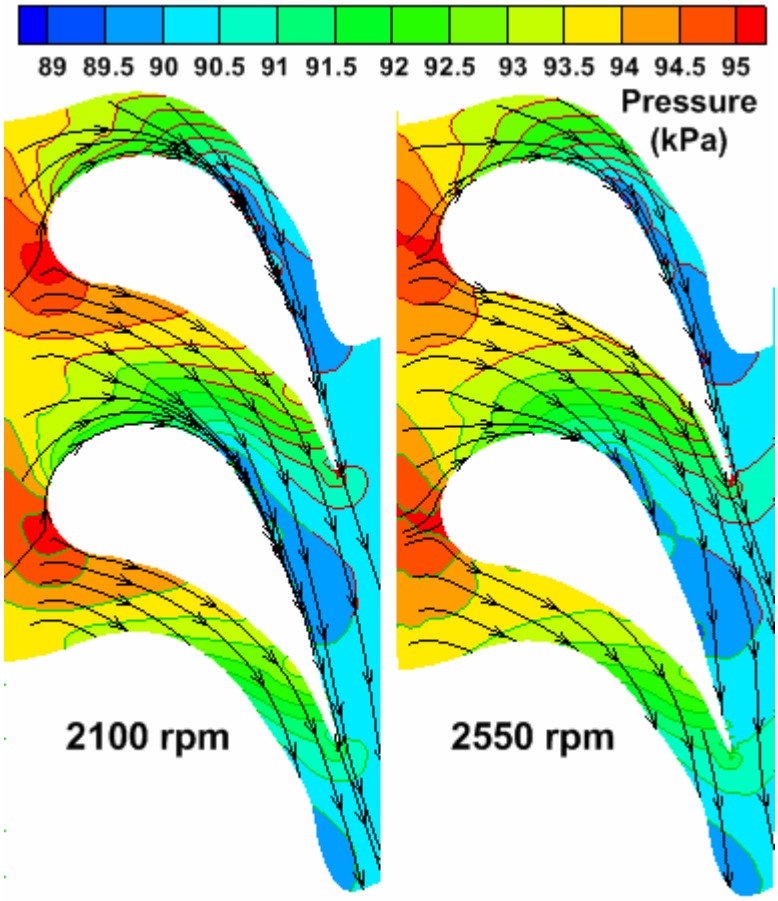

Figure 15: Numerical Prediction of Endwall Static Pressure Distribution (kPa) along with Flow Pathlines, ([100] and [101]).

5.1.1.2 Upstream Injection at Off-Reference Rotating Conditions

At rotational speeds lower than the reference speed, the blade flow deflection becomes larger leading to higher specific stage load coefficient and the stagnation region moves towards the pressure side as the flow incidence angle increases as sketched in Figure 14. At progressively lower rotating speeds, the stagnation line will further move towards the blade pressure side resulting in a higher pressure zone owing to higher flow deflection. The pressure gradient on the platform from the pressure to the suction side gets

affected by this shift in the stagnation region due to larger flow incidence angles. Figure 15 shows the numerical predictions of local static pressures on the platform surface with flow pathlines for 2550rpm and 2100rpm. These numerical predictions were performed using the CFD code, FLUENT for the same geometry and flow conditions. About 1.1 million cells were used to grid 1.5 stages of the turbine. A sliding mesh was used to simulate rotation. A Reynolds stress model with a non-equilibrium wall function was used to solve the Reynolds Averaged Navier-Stokes equations. From the figure, the movement of the stagnation region towards the pressure side for lower rotational speed can be easily discerned. Lower pressure at lower rotating speeds can be observed near the suction side. Figure 15 also shows the mainstream pathlines near the platform surface. The pathlines for 2100rpm appear to converge together as the flow gets pushed to the suction side.

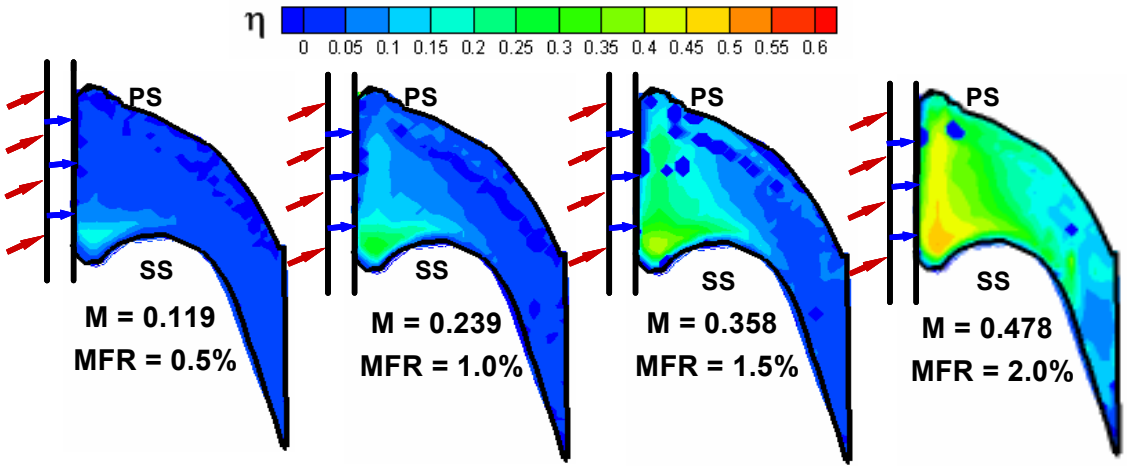

Figure 16: Film Cooling Effectiveness Distribution on the Rotating Endwall for 2400rpm.

The larger gradients in the platform static pressure distribution for lower rotating speeds cause significant movement of the coolant film on the platform surface when it comes from the stator-rotor gap. The local mass flow of coolant from stator-rotor gap depends on the pressure difference between the

plenum and the mainstream static pressure. A higher pressure region near the blade pressure side close to the leading edge at lower rotating speeds will result in a smaller pressure difference across the as compared to reference condition. This will promote non-uniform coolant distribution from the stator-rotor gap with the coolant traces re-orienting themselves towards the suction side of the platform. This phenomenon can be clearly observed from data taken for 2400rpm as shown in Figure 16. Both figures include contour plots for 4 different mass flow ratios. More coolant appears to come out from near the suction side of the platform where the pressure difference across the platform from inlet to outlet is larger with the 2400rpm showing large non-uniformity. Thus, the coolant film distribution and hence film cooling effectiveness strongly depends on the pressure distribution on the platform surface. As the blowing ratio increases, the traces get stronger due to the increase in the coolant momentum.

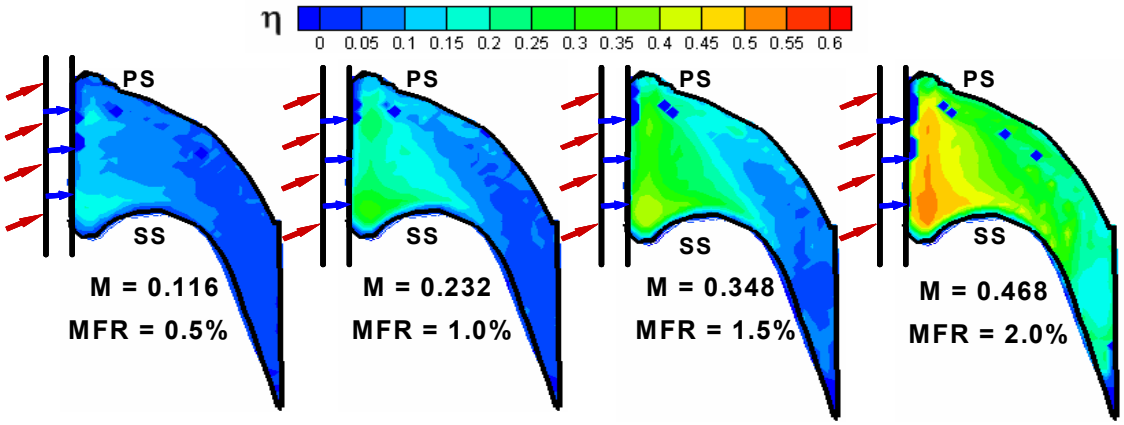

Figure 17: Film Cooling Effectiveness Distribution on the Rotating Endwall for 3000rpm.

Comparing Figure 16 at 2400rpm with Figure 13 at 2550rpm (reference speed), it is observed that the effectiveness magnitudes progressively decrease with lower rpm for the same mass flow ratio. This may be a result of stronger horseshoe vortices close to the suction side owing to the shift in the flow incidence angle at lower rpm. Very low effectiveness levels can be discerned for the lowest blowing ratio, MFR = 0.5% for 2400rpm as compared to other rpm's. Coolant traces can only be observed locally near the

suction side of the blade. The coolant spread for MFR = 2.0% is appreciably larger and some reattachment of coolant can also be observed for 2400rpm similar to that observed for 2550rpm. Effectiveness traces on the suction side though are more visible than that for 2550rpm. Some coolant traces can even be observed close to the trailing edge near the suction side for higher mass flow ratios. For both reference and lower rotating speeds, the region downstream of the throat remains uncooled. Weak traces can be observed in this region for 2550rpm for MFR = 2.0% near the throat. This region experiences much higher velocities from the accelerating mainstream flow resulting in high local heat transfer coefficients. The secondary flow vortices in the passage erode the coolant film before it reaches the throat.

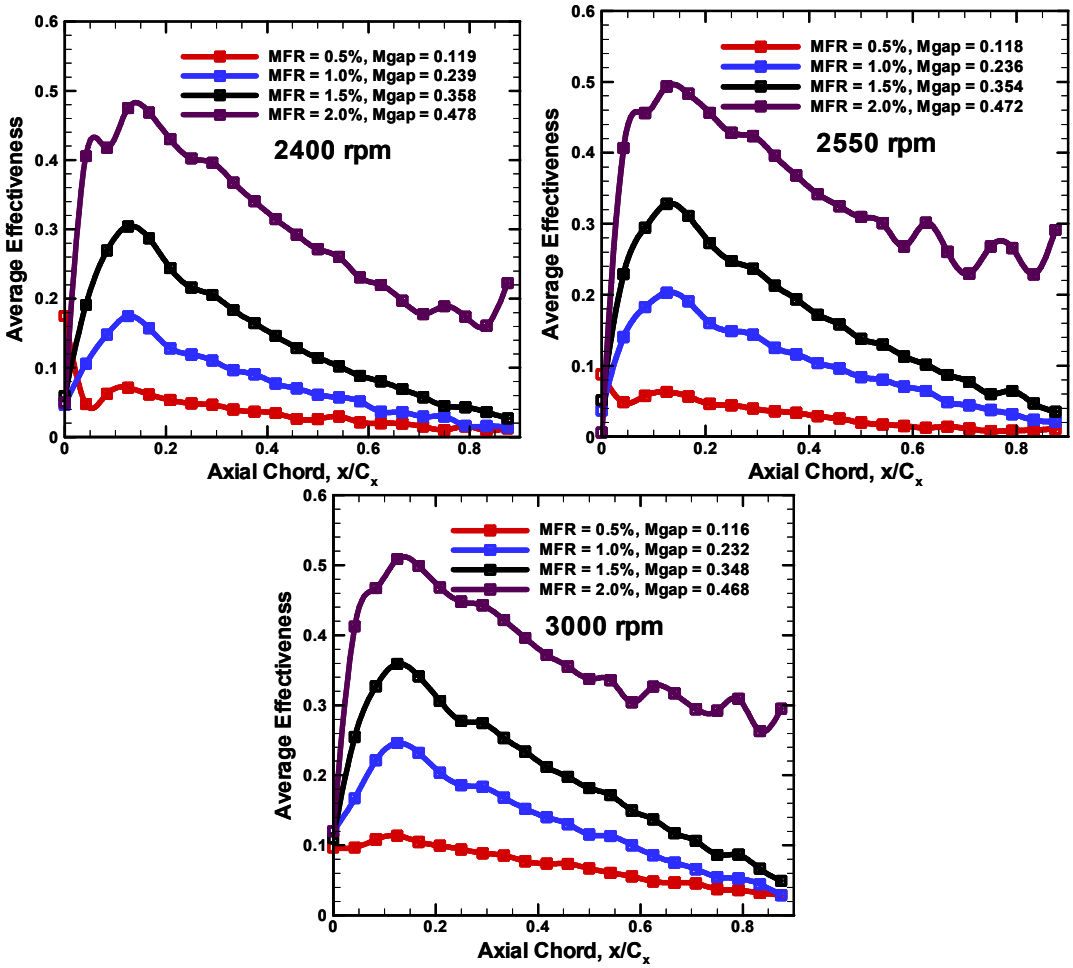

Figure 18: Pitchwise Averaged Film Cooling Effectiveness Distribution along Axial Chord for Different MFR (Mass Flow Ratio Effect).

Figure 17 shows the measured film cooling effectiveness on the rotating platform operating at 3000rpm. Although the film cooling effectiveness measured at 3000rpm varies from that measured at 2550rpm, the variation is less for the higher rotational speed than the lower rotational speeds. Increasing the coolant flow rate increases the coolant coverage area on the rotating platform. As the flow rate increases to 2%, the coolant covers almost the entire passage; whereas at the other rotational speeds, the pressure side of the passage and the trailing edge region were left unprotected.

5.1.1.3 Different Turbine Rotating Speeds (Mass Flow Ratio Effect)

In addition to the effect on static pressure distribution and film cooling due to inlet flow incidence angle change with rotational speed, rotation may also affect the coolant flow as it exits the stator-rotor gap. The disk cavity is bound by two walls, stator endwall and the rotor platform. The enclosed coolant mass in the disk cavity will rotate with a certain frequency due to the cavity wall shear stress. High shear stresses, caused by relative motion in the circumferential gap, may introduce some swirl in the coolant flow as it exits. Hence, a tangential component may exist in the coolant flow as it exits the stator-rotor slot. This may cause some additional spreading of the coolant which cannot be achieved for film cooling studies in stationary cascades. This might also explain the larger coolant spread with increasing rotational speeds due to a larger tangential velocity component in the coolant as it exits the slot. The determination of the swirl angle as well as the measurement of this tangential velocity component was not the subject of the current investigation. However, these are items of high importance along with the inter-stage measurements.

5.1.1.4 Pitchwise Averaged Film Cooling Effectiveness with Upstream Injection

The film cooling effectiveness results were averaged along the pitchwise direction and the averaged data for all coolant-to-mainstream mass flow ratios and rotational speeds are presented in Figure 18 along the axial chord. For a given rotor speed, increase in effectiveness magnitudes with increasing mass flow ratio can be clearly observed from this plot. The averaged plots show a sharp decrease in effectiveness

magnitude along the axial chord as indicated earlier with the region beyond x/C_x = 0.6 remaining mostly uncooled with mean effectiveness magnitudes below 0.1. The spikes occurring as a result of coolant jet reattachment at MFR = 2.0% for 2550rpm, 2000rpm, and 3000rpm can also be observed. The decrease in effectiveness with lower rotational speeds can also be discerned.

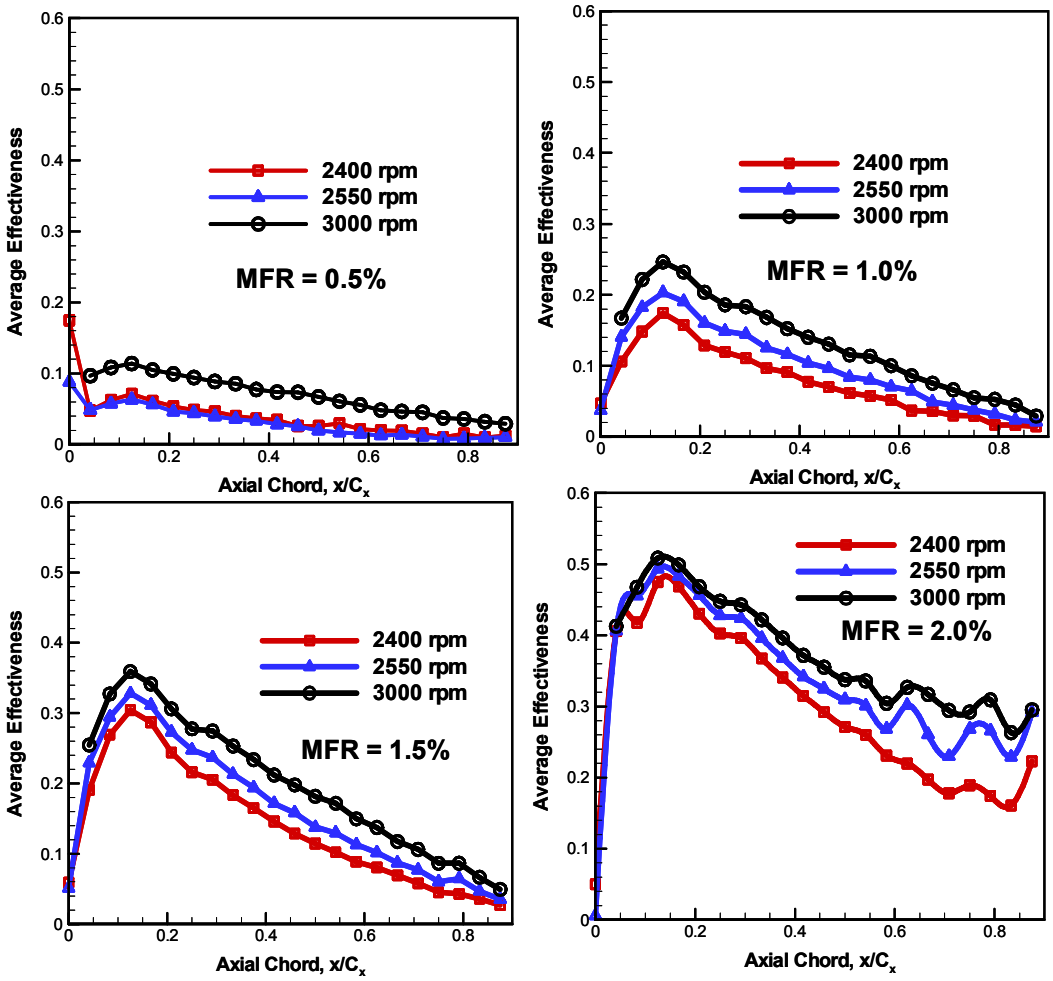

Figure 19: Pitchwise Averaged Film Cooling Effectiveness Distribution along Axial Chord for Different Mass Flow Ratios (Turbine Rotation Effect).

Figure 19 shows the same pitchwise averaged film cooling effectiveness results plotted for the four different coolant-to-mainstream mass flow ratios. The impact of turbine rotational speeds on film cooling effectiveness can be clearly perceived from this plot. As rpm increases, the effectiveness magnitudes increase for the same mass flow ratio. Figure 20 shows the average film cooling effectiveness plotted with *x/MS* as the abscissa. The figure compares the data with a correlation from Goldstein [98] for an equivalent two-dimensional slot on a flat stationary surface as given in Eq. 15.

$$\overline{\eta} = \left(1 + 0.249 \cdot \left(x/M_{gap}S\right)^{0.8}\right)^{-1} \tag{15}$$

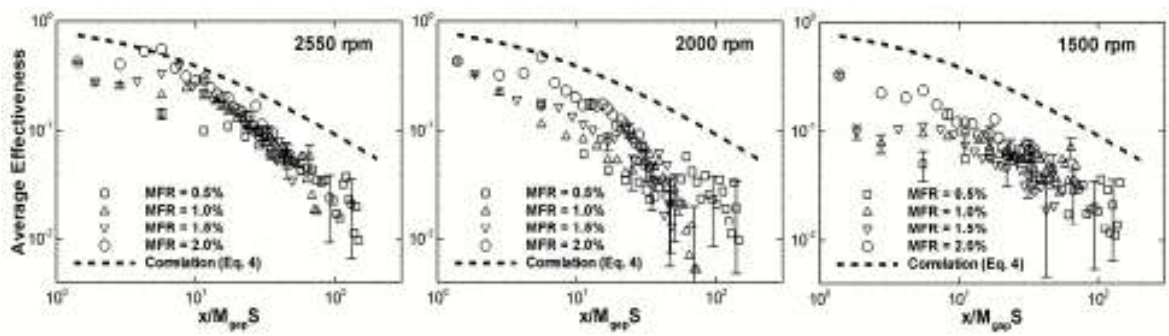

Figure 20: Comparison of Pitchwise Average Effectiveness with a Correlation from Goldstein [40] for Different Speeds.

This correlation works well for *x/MS* > 10, where the flow regime is more two-dimensional. For *x/MS* < 10, the 3-dimensional flow regime due to mixing of the coolant jet with mainstream results in lower effectiveness than that predicted by the correlation. When compared to current data, for reference rotating condition, it shows relatively good comparison with the correlation at *x/MS* = 10 but decays rapidly due to the destructive action of the passage vortex on the coolant film. For lower rotating speeds than reference, more non-uniform pitchwise effectiveness distribution lowers the average effectiveness value with the data for 2400rpm showing the largest deviation from the correlation. The results of these experiments were

published in Suryanarayanan et al [99] and the equivalent numerical prediction was performed by Yang et al [100].

5.1.2 Film Cooling Effectiveness from Discrete Film Cooling Holes

As shown from the previous experiments, the coolant from the stator-rotor seal can adequately protect the upstream half of the blade platform. However, much of the pressure side of the passage, as well as the downstream half of the platform is unprotected and thus left exposed to the hot mainstream gas. Taking this into account, nine discrete holes were machined onto the rotating platform, as shown in Figure 8. The film cooling effectiveness can be measured on the rotating platform with PSP. The blowing ratio for the coolant through the discrete film hole is varied from M_{holes} = 0.5 – 2.0 at intervals of 0.25, based on the relative velocity of the mainstream flow at the rotor exit (station 3). In addition, the rotational speed of the turbine is varied to investigate the effect of rotation at reference and off-reference conditions over a range of blowing ratios. For this set of experiments, the upstream slot coolant injection is completely shut-off and effectiveness is measured on the platform with coolant flowing through only the discrete film cooling holes.

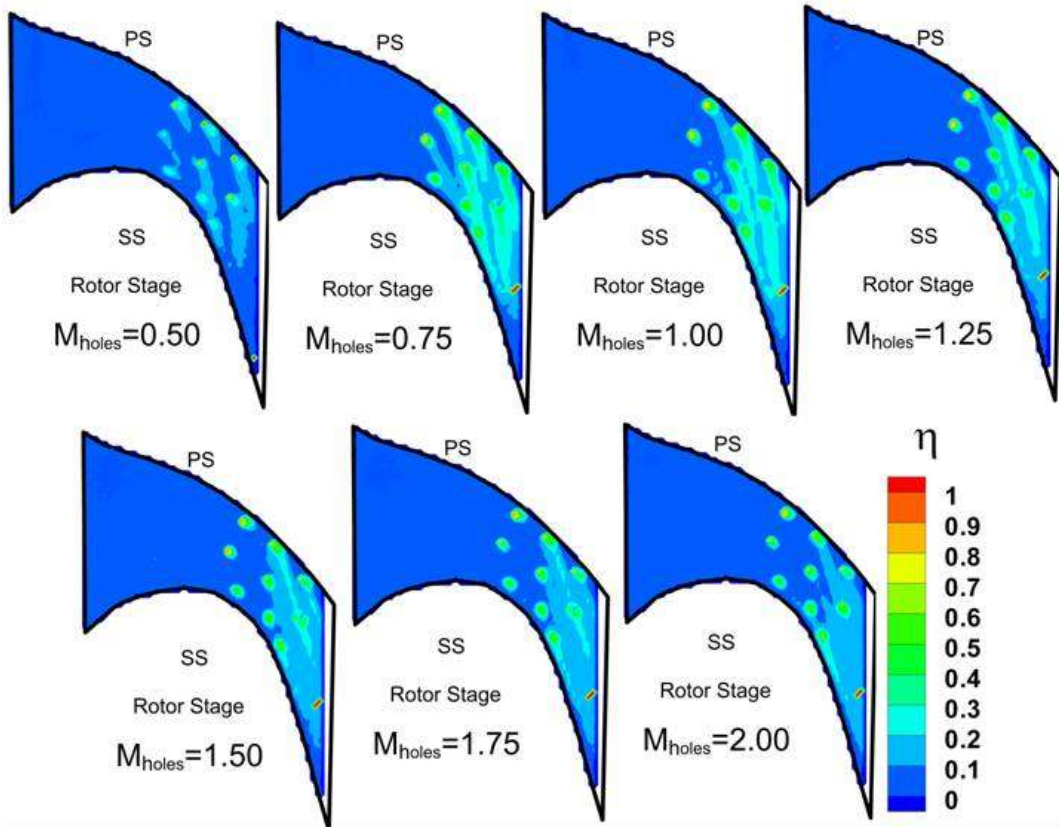

Figure 21: Film Cooling Effectiveness Distribution from Downstream, Discrete Film Cooling Holes on the Rotating Endwall for 2550rpm.

This section presents the results obtained from the film cooling experiments performed on the first stage rotor platform for downstream discrete hole coolant injection. Experiments were conducted at three rotational speeds, 2400rpm, 2550rpm and 3000rpm, with the average film hole blowing ratios of M_{holes}=0.5, 0.75, 1.00, 1.25, 1.50, 1.75 and 2.00. The Reynolds number based on the rotor axial chord length and the exit velocity was around 200,000 and the pressure ratio was 1.12 for the first stage. The rotation numbers corresponding to 3000rpm, 2550rpm and 2400rpm are 0.23, 0.19 and 0.18 respectively. Film cooling effectiveness was calculated by applying the calibration curves to the intensity fluctuation captured by the camera between air and nitrogen injection. Overall it is found that film cooling

effectiveness is maximum as we approach an approximate average blowing ratio of M_{holes}=1.00 for all three rotational speeds. The reference rotational speed of 2550rpm has the maximum effectiveness amongst all rotational speeds for all blowing ratios. Platform cooling using simultaneous upstream slot and downstream discrete hole injection yielded results similar to the individual blowing cases with little to no effects due to synchronized coolant ejection for MFR=1% and M_{holes}=0.75, 1.00 and 1.25.

5.1.2.1 Reference Rotating Case

Film cooling results on the effects of rotational speed performed Ahn (42, 43) showed that the location of the leading edge stagnation line, which yielded symmetric spreading of coolant on the suction and pressure surfaces of the leading edge was at a rotational speed of 2550. This rotational speed was chosen as the reference rotating condition for the current investigation. Figure 21 shows film cooling effectiveness on the rotor platform for downstream hole film cooling for the reference speed, 2550rpm, and all the blowing ratios. As expected film cooling effectiveness is maximum near the coolant hole exit. As we proceed downstream of the holes, effectiveness magnitude diminishes as the coolant mixes with the mainstream flow. Peak effectiveness values occur as we approach M_{holes}=1 and is approximately equal to η=0.70 exactly where the coolant ejects out of the holes. Effectiveness values and film distribution begin to decrease below and above M_{holes}=0.75 and 1.25 respectively. M_{holes} in this range provide good film cooling protection on the platform covering most of the downstream passage surface. The contribution of each hole towards effective film coverage also varies depending on its location on the platform surface.

Since coolant density is assumed to be the same as that of the mainstream, M_{holes} is dependent only on the exit velocity of the coolant gas. For M_{holes}=1.00, the velocity of the coolant ejecting out of the individual holes is approximately the same as that of the mainstream relative velocity at the first stage rotor exit. As the coolant flow velocity approaches the mainstream relative velocity, it appears that the ejected coolant has just the right momentum to adhere to the platform surface displacing the mainstream boundary layer and minimizing the effects of the secondary flows. This allows the coolant to provide better film coverage and higher effectiveness magnitudes as minimal coolant is dissipated into the

mainstream flow before providing any protection. At M_{holes} lower than 0.75, the coolant quantity for film cooling is small and is incapable of providing any effective protection on the platform surface. The lower momentum prevents the coolant from penetrating the boundary layer on the platform surface, hindering the development of an effective thermal barrier. The low momentum coolant tends to get carried away by the higher momentum mainstream flow decreasing the effectiveness. On the contrary, the ejected coolant for M_{holes} higher than 1.25, possess larger momentum and have a tendency to lift-off as they leave the coolant holes. The high velocity coolant merges with the mainstream immediately having little time to shield the platform surface. This effect of coolant mass on film effectiveness is similar to that seen by Zhang and Jaiswal [51] with their experiments on a linear cascade.

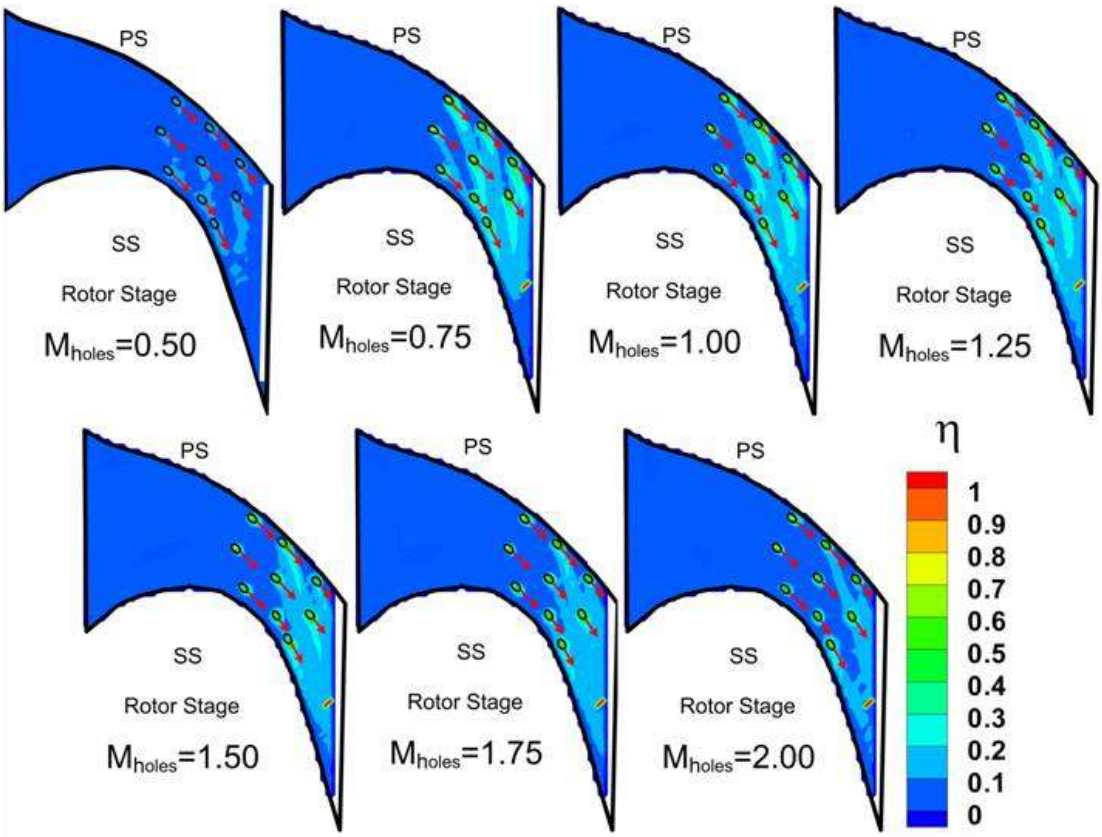

Figure 22: Film Cooling Effectiveness Distribution from Downstream, Discrete Film Cooling Holes on the Rotating Endwall for 2400rpm.

The coolant distribution on the platform is predominantly governed by the mainstream and secondary flow characteristics. The secondary flow generated by the pressure differential between neighbouring blades influence the behaviour of coolant gas in their path and significantly affects the capability of the coolant to offer uniform thermal protection. The coolant under the effects of the secondary flow is drawn towards the suction surface leading to better protection near the suction surface. This movement of the coolant to the suction side under the influence of the platform secondary flow has also been documented by researchers experimenting with cascades. The higher tangential velocity of the coolant jet under rotation also increases the migration of the coolant from the pressure side to the suction side on the platform. Interestingly, the holes 1 and 4 (Figure 8) show lower effectiveness and coolant coverage compared to the other holes. It is believed that these two holes lie in the path of the passage vortex and hence the coolant ejected through them is immediately dissipated into the mainstream. It can be deduced that providing protection closer to the suction surface is relatively easier due to the tendency of the coolant to flow towards the suction surface.

5.1.2.2 Effect of Rotation on Film Cooling

At rotational speeds lower than the reference speed, the blade flow deflection becomes larger leading to higher specific stage load coefficient and the stagnation region moves towards the pressure side as the flow incidence angle increases as sketched in Figure 14. Similarly, higher rotational speeds lead to negative incidence angle and cause the stagnation region to move towards the suction side. The pressure gradient on the platform across the pressure and suction side is affected by the change of the incidence angle based on the rotational speed change. This will alter the location of formation and the strength of the passage vortex and other secondary vortice which affect platform film cooling. Figure 22 and Figure 23 show the film cooling effectiveness distribution for off-reference rotational speeds of 2400rpm and 3000rpm. The figures contain contour plots for all the blowing ratios with the arrows depicting the geometric orientation of the coolant holes on the platform. Under no mainstream flow, the coolant exiting the holes is assumed to follow the arrow direction.

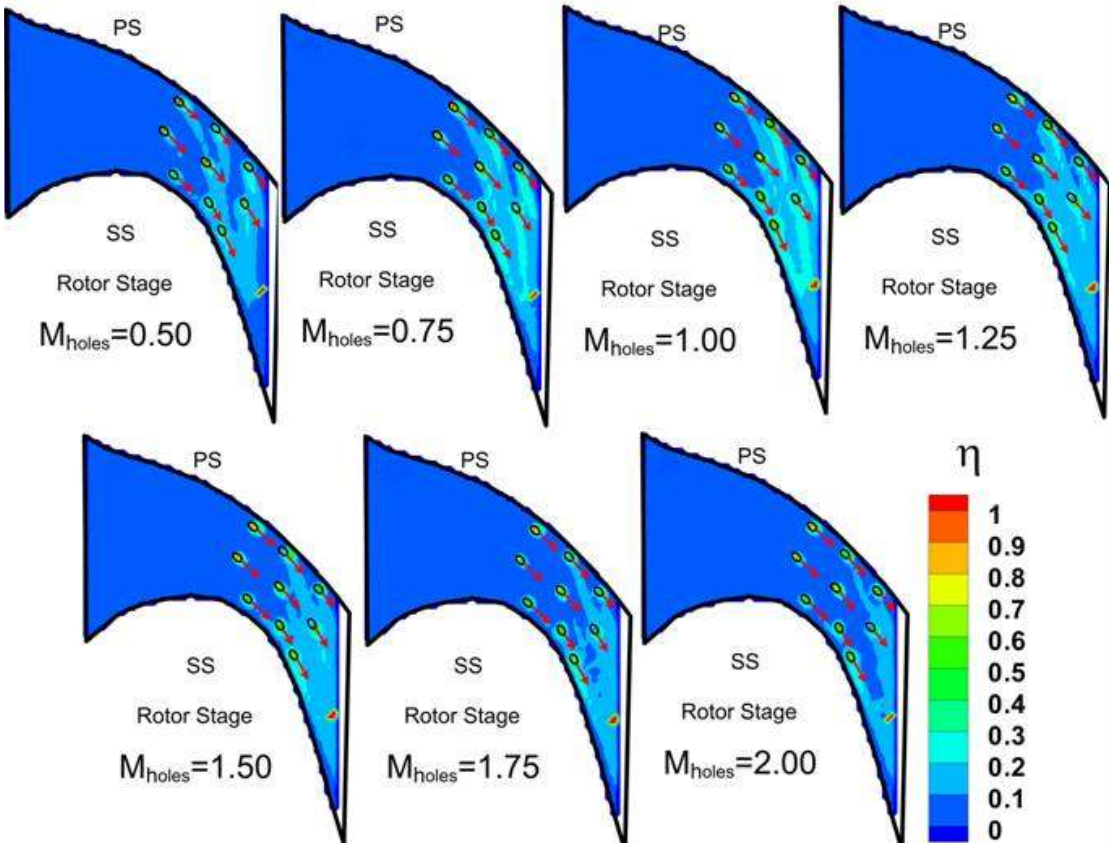

Figure 23: Film Cooling Effectiveness Distribution from Downstream Discrete Film Cooling Holes on the Rotating Endwall for 3000rpm.

Overall, it is seen that the effectiveness values for off-reference speeds are lower when compared to the reference speed. Reference speed of 2550rpm has larger areas of the platform with higher film cooling effectiveness though the peak effectiveness lies in the same range as the off-reference speeds. Blowing ratios below 0.75 and above 1.25 provide minimal protection to the platform surface irrespective of the rotational speeds. The coolant traces once again follow the cross flow from the pressure side to the suction side.

Maximum effectiveness for 2400rpm occurs between M_{holes}=1.00 and 1.25 and for 3000rpm it is between M_{holes}=0.75 and 1.00. The effectiveness magnitudes for both cases show a peak value of approximately η=0.70 close to the coolant hole exit. Varying the rotational speed over or under the reference speed affects the coolant distribution on the platform surface with the higher rotational speed showing the lowest coolant coverage. At rotational speeds lower than the reference speed and for same blowing ratio, the coolant mass ejected through the holes is smaller and hence has a lower relative velocity than the reference case. Similarly at higher rotational speeds the coolant ejecting out of the holes has a higher relative velocity due to the higher coolant mass necessary to maintain the same blowing ratio. This causes the M_{holes} =1.00 and 1.25 (higher coolant flow mass) to have a better effectiveness at 2400rpm than the lower blowing ratios while at 2550rpm and 3000rpm, the best film protection is between M_{holes} =0.75 and 1.00 which has the ejected coolant mass comparable to M_{holes} =1.00 and 1.25 at 2400rpm.

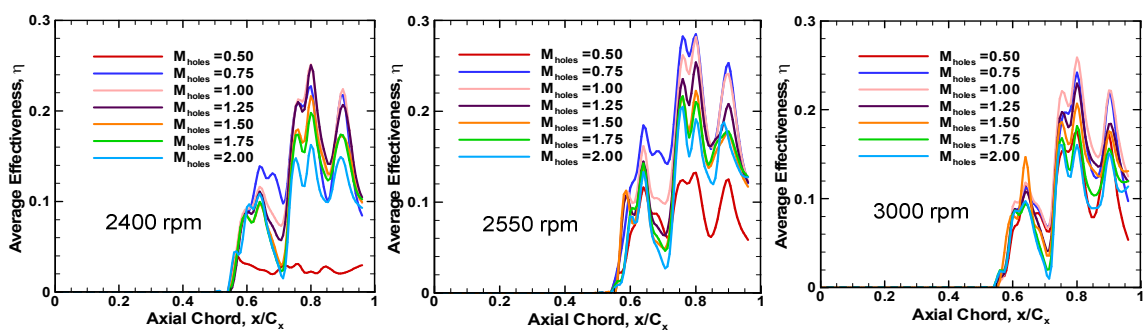

Figure 24: Pitchwise Averaged Film Cooling Effectiveness Distribution along Axial Chord for Different Turbine Rotating Speeds (Mass Flow Ratio Effect).

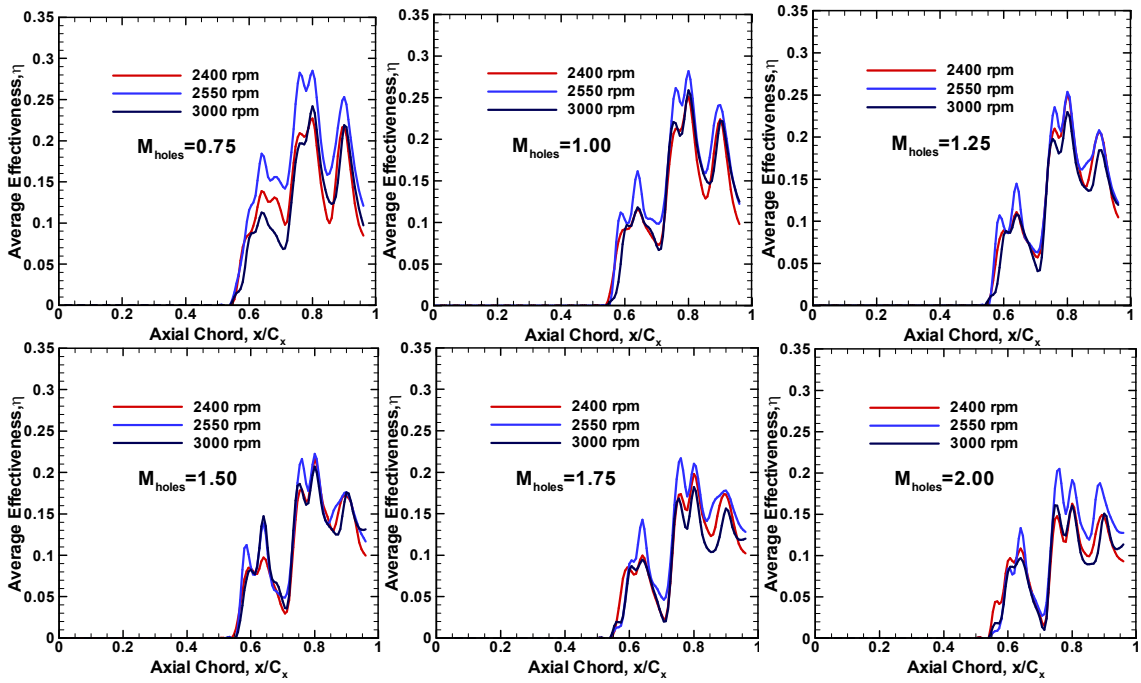

Figure 25: Pitchwise Averaged Film Cooling Effectiveness Distribution along Axial Chord for Different Hole Blowing Ratios (Rotation Effect).

5.1.2.3 Pitchwise Average Film Cooling Effectiveness

The film cooling effectiveness data obtained for the three rotational speeds and all the blowing ratios are averaged pitchwise and plotted along the axial chord (Figure 24) to study the effects of individual blowing ratios. The peaks on the plot represent the location of the holes on the platform in the axial direction. The holes are positioned to provide cooling to approximately 50% of the passageway. It is clearly seen that the effectiveness values are maximum for M_{holes}=0.75 to 1.25 for all three rotational speeds. For 2400rpm, M_{holes}= 1.00 and 1.25 have higher effectiveness as the coolant velocity and in turn the ejected coolant quantity is higher at these blowing ratios. Similarly, 2550rpm and 3000rpm have higher effectiveness magnitudes between M_{holes}= 0.75 and 1.00. At these blowing ratios the coolant

velocity and hence the coolant mass effectively suppress the effects of the secondary flow leading to better coolant distribution on the platform surface. Increase in rotational speed causes the coolant exit velocity to increase for the same blowing ratio. To quantify the effects of rotation on film cooling effectiveness, the pitchwise averaged film cooling effectiveness was plotted along the axial chord for different rotational speeds but same blowing ratio (Figure 25). It is obvious from the plot that for the same blowing ratio, film cooling effectiveness is maximum for the reference speed of 2550rpm. The effectiveness magnitudes decrease on either side of the reference speed with 2400rpm having slightly higher values than 3000rpm as the flow conditions prevailing on the platform for 2400rpm are much closer to the reference speed.

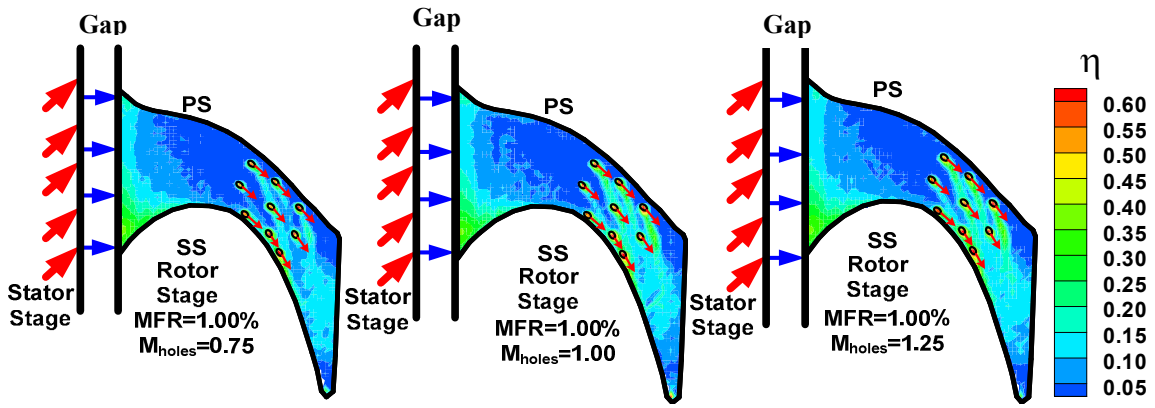

Figure 26: Film Cooling Effectiveness for Combined Stator-Rotor Gap and Hole Coolant Injection, 2400rpm.

5.1.3 Combined Upstream Stator-Rotor Gap Purge Flow Cooling and Downstream Discrete Hole Cooling

A combined platform cooling case involving coolant ejection through upstream stator-rotor annular slot presented in a recent study by Suryanarayanan et al. [99] and downstream discrete holes was examined for 2400rpm, 2550rpm and 3000rpm to understand the interaction between the two methods of cooling under rotation.

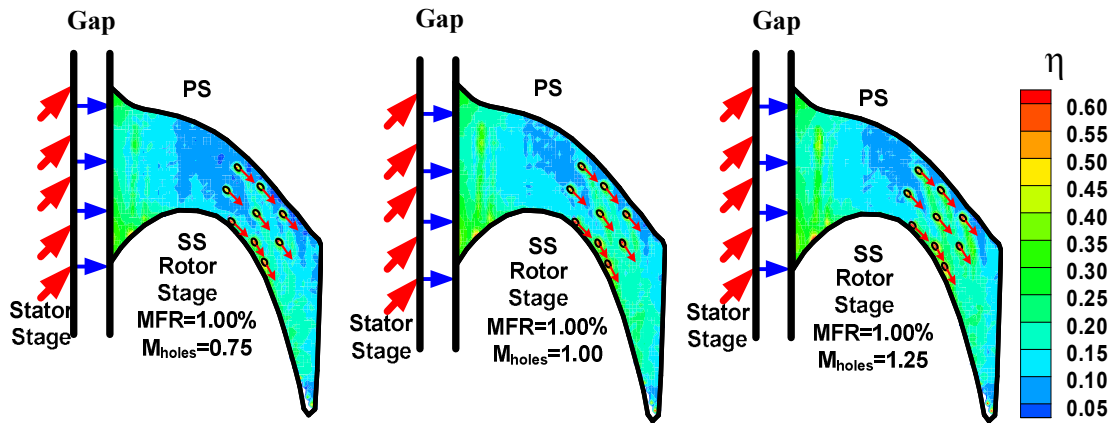

Figure 27: Film Cooling Effectiveness for Combined Stator-Rotor Gap and Hole Coolant Injection, 2550rpm.

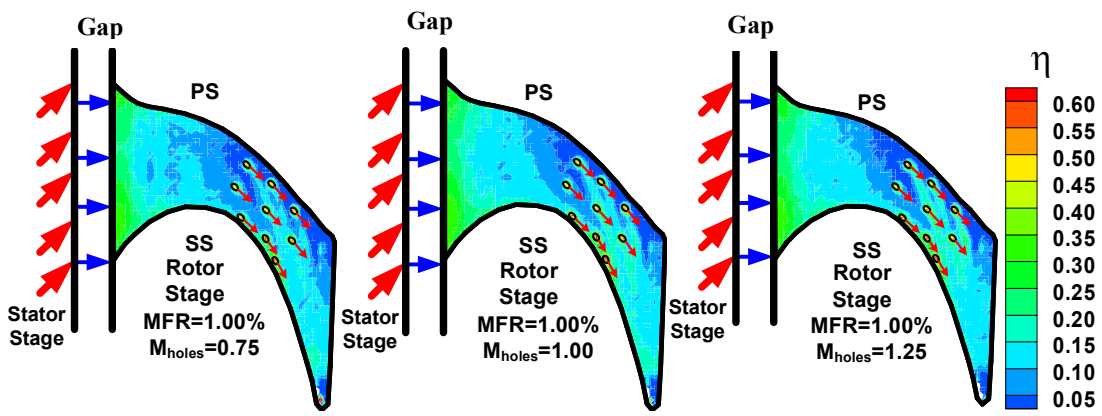

Figure 28: Film Cooling Effectiveness for Combined Stator-Rotor Gap and Hole Coolant Injection, 3000rpm.

It is expected that the coolant ejected out of the slot will cover the platform front portion while the holes will provide protection in the downstream region. For the upstream blowing a coolant to mainstream mass flow ratio of 1% was considered as it was found to cover most of the upstream platform surface at all rotational speeds by Suryanarayanan et al. [99]. For the downstream hole blowing, M_{holes}= 0.75, 1.00 and 1.25 were chosen as they provided the maximum film cooling benefits. Film cooling effectiveness data

was acquired using PSP technique with coolant supplied simultaneously through both the loops. Temperatures of both the coolant loops were maintained the same as the mainstream flow to eliminate any temperature effects. Figure 26, Figure 27 and Figure 28 show the film cooling effectiveness for the combined coolant ejection case for all three turbine rotational speeds. Red and blue arrows depict the mainstream and stator-rotor gap coolant flow respectively. The figures also show the relative location of the stator-rotor upstream gap with respect to the blade leading edge. The coolant supplied through the stator-rotor gap as expected provides fairly good coverage in the upstream region though the distribution in the pitchwise direction is not uniform near the blade leading edge. Coolant concentration near the suction side (SS) is greater than near the pressure side (PS) for all rotational speeds. The pressure gradient that persists between the pressure and suction surface of the blade tends to draw most of the coolant towards the suction side. At 2400rpm, a strong vortex on the platform near the leading edge pressure side depletes any coolant supplied in this region and leads to lower effectiveness magnitudes. As the rotational speed is increased, the position of stagnation point on the leading edge changes. This movement of the stagnation point from the pressure surface leading edge for the lower rotational speed to the suction surface for the higher rpm's causes the pressure gradient ($\Delta P/\Delta S$) across the platform between the suction side and the pressure side to decrease leading to a much more uniform static pressure distribution on the platform surface. This reduction in the spanwise pressure gradient reduces the strength of the horse shoe vortex and allows for the spreading of the purge flow coolant on the platform surface leading to higher effectiveness.

Also, the coolant exiting the gap, as it travels from the disk cavity into the rotating frame, undergoes a swirl due to the high shear associated with relative motion in the circumferential gap. This might cause some further spreading of the coolant on the platform surface for the higher rotor speeds. A little downstream of the leading edge near the pressure surface on the platform, the effect of upstream coolant ejection is drastically reduced as the passage vortex detaches from the pressure side and travels across the platform to merge with the suction side horse shoe vortex, diminishing the coolant coverage on the platform surface closer to the blade pressure side. These results are comparable to that obtained for the individual rotor frequencies discussed earlier at the same MFR. The downstream hole blowing follows the

trend seen in individual hole blowing cases discussed earlier. Reference rotation speed has the best spread and effectiveness magnitudes. Pitchwise averaged film cooling effectiveness for the combined case is as shown in Figure 29. The results for the combined case reflects data for the individual blowing cases put together and gives a comprehensive view of the appropriate upstream slot blowing MFR, average hole blowing ratio and location of the coolant holes to provide appropriate coolant coverage for each rotational speed. The zero in the axial chord direction for the combined case corresponds to an x/C_x=0.18 to 0.2 in the experiments with just the upstream gap injection. This was done due to geometric constraints on the data acquisition plexiglass window while attempting to capture both upstream and downstream effects simultaneously.

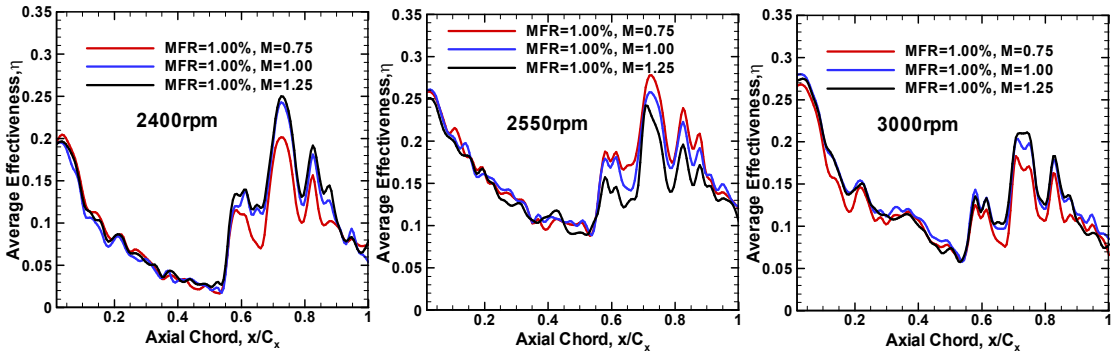

Figure 29: Pitchwise Averaged Film Cooling Effectiveness for Combined Upstream Slot and Downstream Discrete Hole Injection.

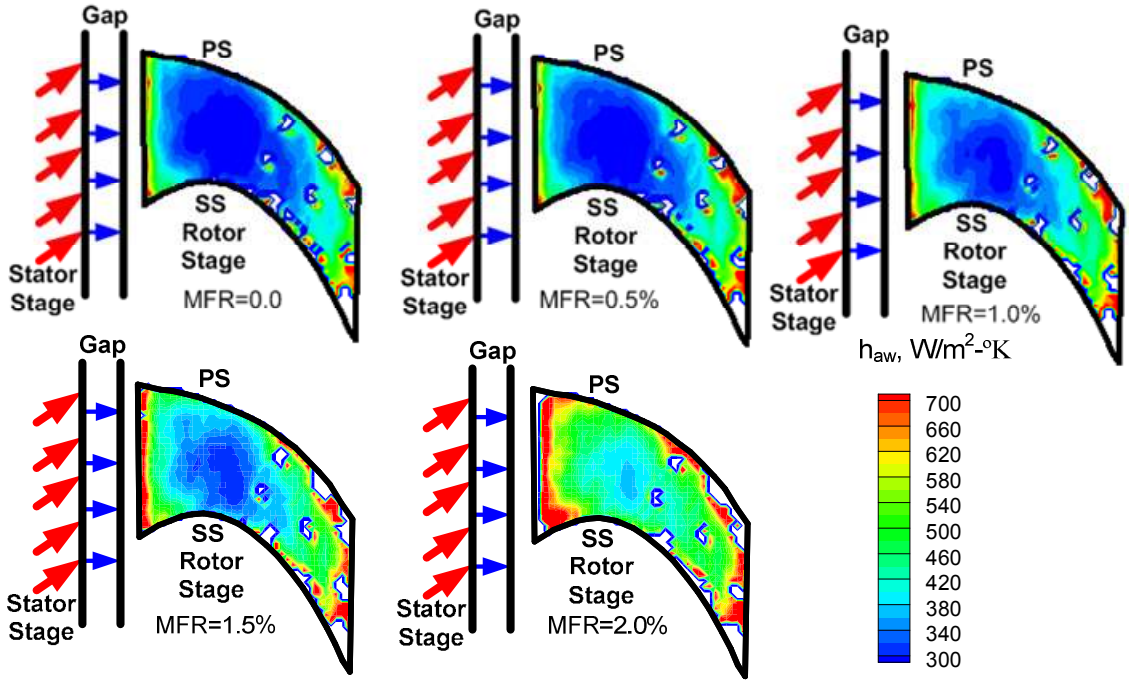

Figure 30: Heat Transfer Coefficient Distribution from Upstream Stator-Rotor Gap Coolant Injection on the Rotating Endwall for 2550rpm.

5.2 Experimental Heat Transfer Measurements

As the final step towards the completion of the project heat transfer measurements were performed on the rotor platform for upstream stator-rotor gap coolant injection at the reference speed of 2550rpm and off-design frequency of 2400rpm. Four different upstream stator-rotor gap coolant to mainstream mass flow ratio were considered to see the effects of rotation on heat transfer distribution due to coolant injection. To allow for heat transfer measurements, a constant flux printed circuit board heater matching the rotor blade passage profile was installed on the rotor platform. An external power supply provided a constant source of power supply to the heater through the slip ring. Thermocouples mounted at different locations on the platform monitored the operating conditions during experiments and allowed for the calculation of heat loss due to conduction and radiation. TSP technique used to measure the surface

temperatures facilitates acquisition of high resolution data and there and provides an accurate picture of the coolant flow and its interaction with the mainstream flow under centrifugal and coriolis forces.

5.2.1 Heat Transfer from Upstream Slot Cooling

5.2.1.1 Upstream Injection at Reference Rotating Condition

Figure 30 shows the heat transfer coefficient distribution on the rotor platform for at the reference rotor frequency of 2550rpm and coolant to mainstream mass flow ratios of 0%, 0.5%, 1.0%, 1.5% and 2.0%. In general it is seen that increasing the coolant to mainstream mass flow ratio increases the heat transfer on the rotor platform. The distribution of the heat transfer coefficients along the rotor platform is similar to that seen in stationary cascades. The suction side has a higher flow velocity and hence, higher rate of heat transfer in the region close to the leading edge. The passage mid-section experiences the least heat transfer and is represented by the smaller heat transfer coefficient values. As we proceed towards the trailing edge, the flow accelerates and the heat transfer coefficients increase in magnitude. Also, the rate of heat transfer is amplified by the presence of holes intended for future heat transfer measurements with discrete hole coolant injection. The holes act as hurdles to the flow and cause additional turbulence and enhance heat transfer.

MFR=0% is the reference case where the heat transfer coefficients on the platform are determined with just the mainstream flow. Close to the blade leading edge the heat transfer coefficient is approximately uniform across the platform though a small region near the leading edge on the suction surface shows a higher rate of heat transfer compared to the pressure side. The magnitude of heat transfer coefficient varies between 500 to 700 W/m^2-K in the entrance region as will be later evidenced more clearly in the chordwise averaged plot. The higher magnitude of 'h' near the passage inlet is due to a combination of factors like the rotation leading to differential pressures on the platform and coolant injection. The scale of 200-500 W/m^2-K is used to provide a platform for comparison with off-design rotor frequency. A region of low heat transfer coefficient (in the range of 200-300 W/m^2-K) is seen to exist just near the blade mid-section. Once the coolant injection is started, the heat transfer rate near the leading

edge and across the platform increases. Injection of the coolant increases the momentum of flow close to the platform and the ensuing higher turbulence causes the rise in heat transfer rates. As evidenced from previous film cooling effectiveness measurements for gap injection, the coverage of coolant on the platform is seen to increase with increase in coolant mass. This coolant coverage on the platform causes a mixing of the flow in the boundary layer region over a larger area. As a result the heat transfer rates near the platform mid-section is also higher than the reference MFR=0.0% case. At lower MFR, the coolant does not possess sufficient velocity and hence, the momentum necessary to disrupt the existing boundary layer. The turbulence levels are therefore smaller leading to lower heat transfer rates and smaller area of influence. At MFR=2%, the effects of coolant are observed further downstream of the leading edge manifesting as increase in heat transfer coefficients. This distribution matches with the coolant distribution seen in the film cooling effectiveness measurements where increase in MFR resulted in more of the platform coming under the coolants protection. Increasing the coolant mass provides better film cooling effectiveness but also increases 'h'. An informed decision should be made by the designer to balance film protection and coolant usage to minimize efficiency losses and at the same time provide optimum protection.

5.2.1.2 Upstream Injection at Off-Reference Rotating Condition

At frequencies lower than the reference speed, the flow angles of the mainstream flow are significantly different than the same for reference speeds causing the movement of the stagnation point on the blade leading edge more towards the pressure side (Figure 14). The suction surface pressures decrease further and the pressure differential between the pressure side and the suction side increases. The higher static pressures near the pressure surface leads to uneven coolant coverage of the platform with more of the coolant being oriented towards the low pressure area near the suction side as compared to that seen for the reference speed. Hence, the 'h' magnitudes in the leading edge suction surface are lower than at reference speed. At a lower rotational frequency, the coolant film has lower total energy and is unable to disturb the boundary layer. Figure 31 shows the heat transfer coefficient distribution on the rotor platform

for the off reference rotor frequency of 2400rpm and MFR between 0% and 2%. The heat transfer coefficient distribution for 2400rpm is similar to 2550rpm except that the magnitudes are lower and the effect of coolant on the platform surface is also restricted in the chordwise direction. For both the speeds, the platform region beyond 50% of the blade chordwise length show little to no effect due to upstream coolant injection. Regions of discontinuity observed beyond the passage mid-section are due to the presence of coolant holes and the turbulence they add to the mainstream flow.

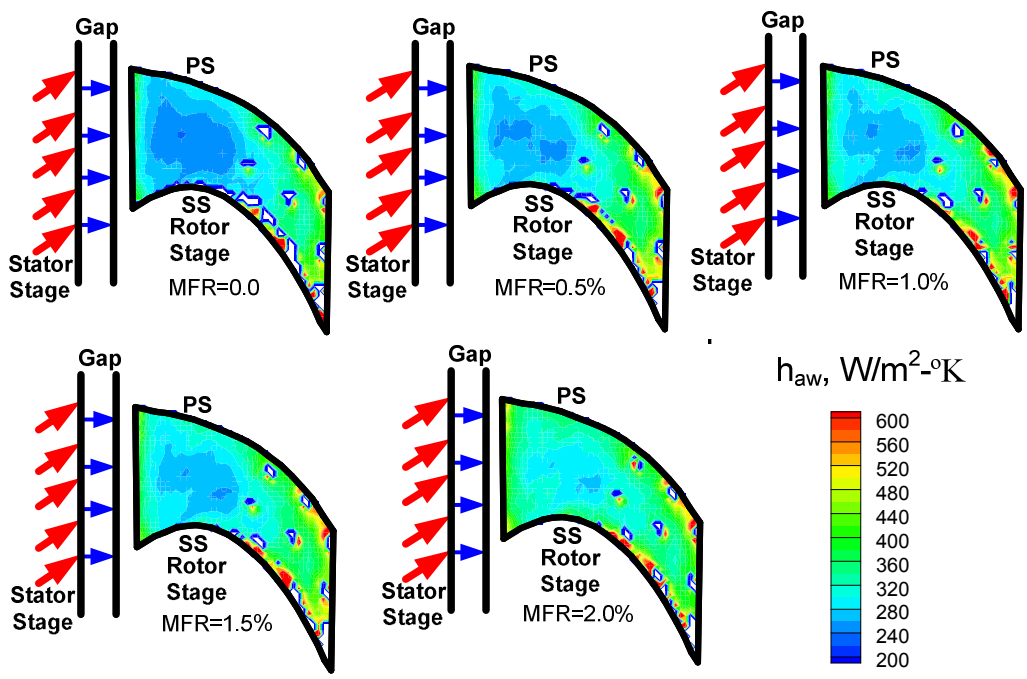

Figure 31: Heat Transfer Coefficient Distribution from Upstream Stator-Rotor Gap Coolant Injection on the Rotating Endwall for 2400rpm.

5.2.1.3 Pitchwise Averaged Heat Transfer Coefficients with Upstream Injection

To understand the effects of MFR on platform heat transfer, the heat transfer coefficients were averaged along the pitchwise direction for each of the coolant mass flow ratios and plotted as shown in Figure 32. Increase in MFR leads to higher heat transfer coefficients for both the reference and off

reference rotor frequencies. Maximum heat transfer is seen to occur very close to the leading edge which in turn is near the coolant injection slot. A 20-25% increase in heat transfer is observed by increasing the MFR from 0% to 2%. As we proceed from the leading edge to the trailing edge, a sharp drop in heat transfer coefficient is seen for all MFRs as the coolant begins to dissipate into the mainstream at about 35-40% in the chordwise direction and only a small change in 'h' is seen beyond this fall. As we approach the throat region the mainstream flow is accelerated and 'h' increases and is accentuated by the disturbance the coolant holes cause to the mainstream flow, though in this region the 'h' values remain almost the same for all the MFR indicating that the upstream coolant injection for MFR=0.5% to 2.0% has little to no effect here.

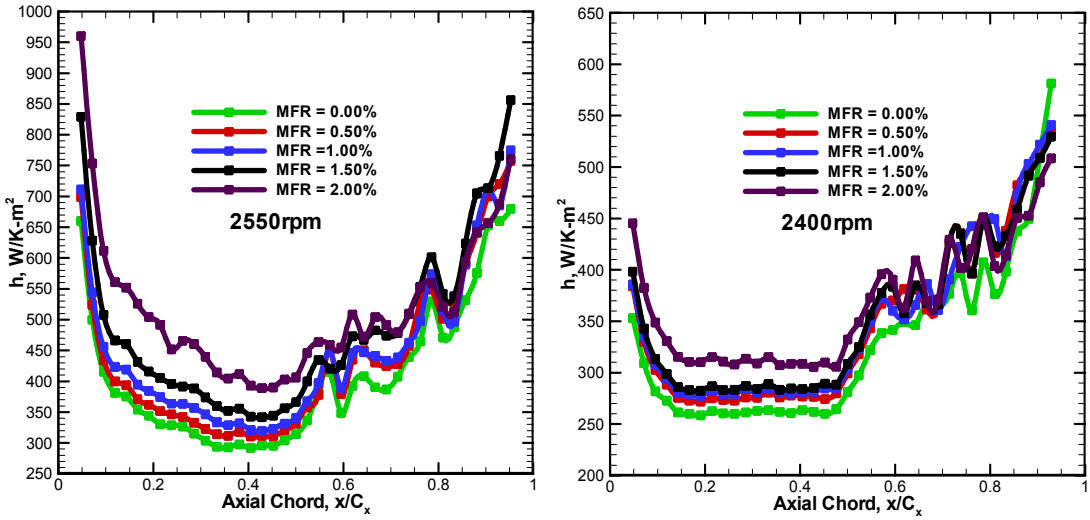

Figure 32: Pitchwise Averaged Heat Transfer Coefficient Distribution along Axial Chord for Different Turbine Rotating Speeds (Mass Flow Ratio Effect).

Figure 33 shows the effects of rotation on the pitchwise averaged heat transfer coefficients for MFR between 0% and 2.00%. The higher momentum of the mainstream flow combined with that of the coolant at the higher rotational frequency enhances the heat transfer on the platform for coolant all mass flow

rates. Thus it can be deduced that increasing the rotor speed has an amplifying effect on the platform heat transfer.

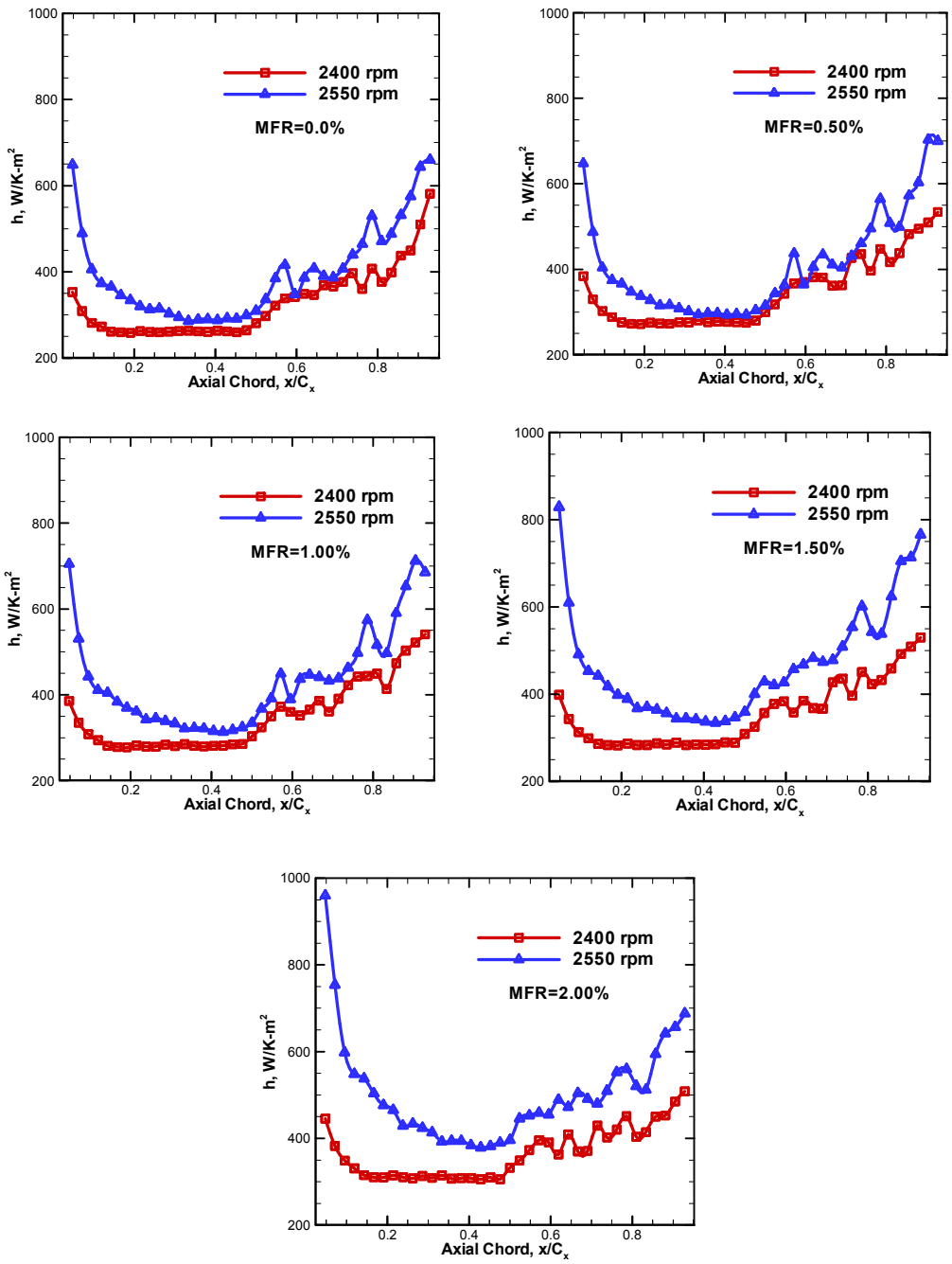

Figure 33: Pitchwise Averaged Heat Transfer Coefficient Distribution along Axial Chord for Different Mass Flow Ratios (Rotation Effect).

Comparing the experimental (Suryanarayanan et al [99]) and the numerically predicted (Yang et al [101]) heat transfer results, it is observed that the magnitude of the heat transfer coefficient is lower in the predictions. On the contrary for the similar case, the effectiveness is higher for the predicted results. It can be deduced that in the experimental case the injected coolant mixes more rapidly with the mainstream flow than in the predictions; thereby, decreasing the effectiveness magnitudes and increasing mixing leading to higher heat transfer coefficients. Further, it is also noted that any increase in rotational frequency appears to decrease the heat transfer coefficient distribution on the rotor platform in the predicted results as against an increase seen in the experimental data.

5.2.2 Heat Transfer due to Downstream Hole Cooling

Heat transfer measurements were also performed for downstream discrete hole coolant ejection on the rotor platform surface for 2400rpm and 2550rpm and average blowing ratios of M=0.75, 1.00 and 1.25 as the film cooling effectiveness was found to be optimum for these blowing ratios. Heat losses are calculated using the thermocouples placed underneath the heater and insert at different locations along the leading and trailing edges. Since, the temperature differential between the thermocouples between the heater and insulation in the leading and trailing edge varied by a small value (~2.5ºC), it can be assumed that the heat loss along the rotor passage is approximately uniform and hence, using either set of thermocouples for heat transfer calculation is appropriate. As for earlier gap injection, the temperature differential between the rotor platform surface and the coolant and mainstream flow was maintained between 10ºC and 15ºC to minimize measurement errors while using TSP for temperature measurements. The same experimental set up with similar camera exposure settings and image acquisition rates were used for the hole injection experiments.

The results indicate that heat transfer coefficient is the highest when the blowing ratio is closer to one for both the rotational speeds. The coolant trace orients towards the suction surface though the amount of deflection and a relative comparison with a stationary platform for similar case is unavailable in open literature. Rotation appears to affect the heat transfer between the platform and mainstream flow with the highest magnitudes seen for the reference speed of 2550rpm. The upstream ‘h’ values are commensurate

with the no injection case observed at MFR=0% with rotor-stator slot injection.

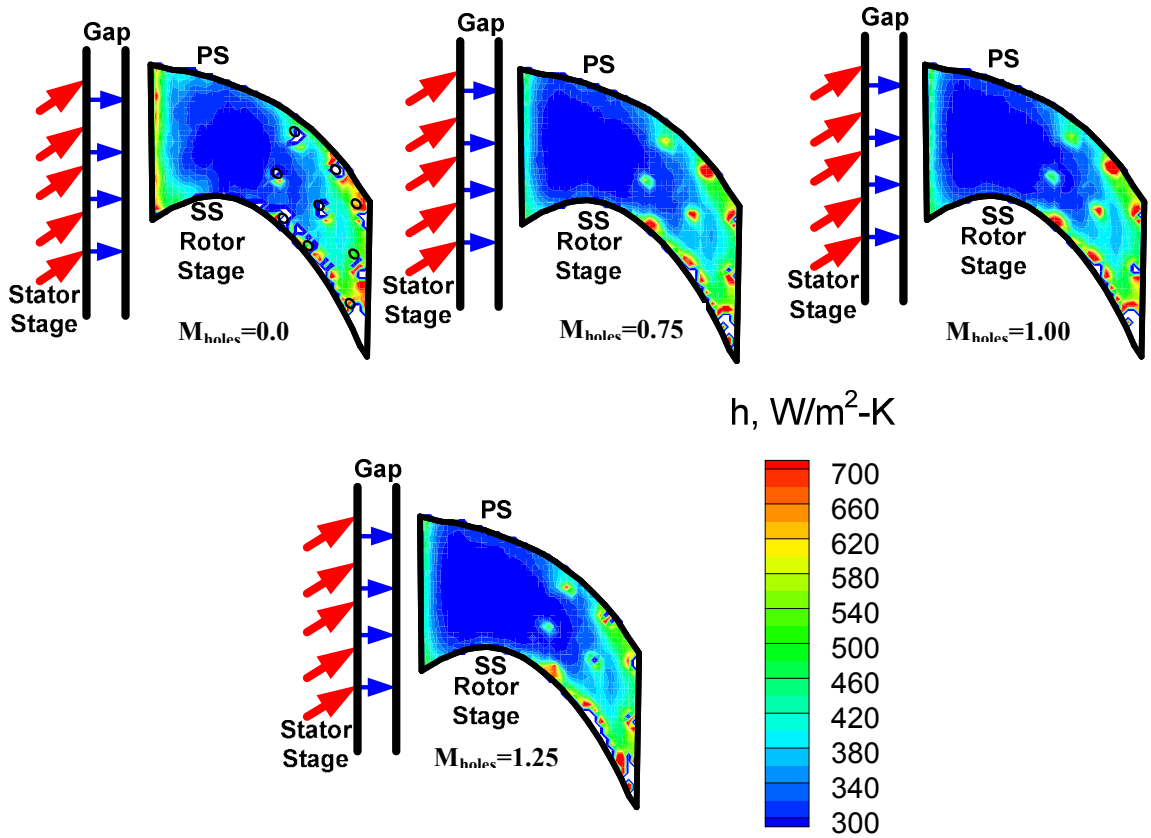

Figure 34: Heat Transfer Coefficient Distribution from Downstream Discrete Hole Coolant Injection on the Rotating Endwall for 2550rpm.

5.2.2.1 Downstream Injection at Reference Rotating Condition

Heat transfer coefficient distribution on the rotor platform for downstream discrete hole coolant injection at the reference speed of 2550rpm and the three blowing ratios are shown in Figure 34. The maximum heat transfer occurs near the hole entrance where the injected coolant meets the mainstream flow. As we proceed further downstream of the hole, the magnitude of 'h' decreases as the interaction of the coolant with the mainstream decreases and the coolant dissipates into the mainstream, away from the

platform surface. Maximum 'h' values in the range of 700W/m^2-K are encountered exactly where the coolant exits the holes. The effect of coolant injected through each hole on platform heat transfer varies depending on their location in the flow passage. The central hole in the first column is affected by the passage vortex and the coolant ejecting out of it is immediately mixed with the mainstream flow. Coolant path manifests clearly as increase in heat transfer when compared with the zero blowing condition. Coolant is observed to migrate from the pressure surface to the suction surface on account of the pressure differential existing on the platform and also due to the tangential velocity component due to rotation.

As noted earlier in the film cooling experiments, the density ratio of the mainstream flow and coolant is equal to one implying that the blowing ratio is simply the result of difference in the coolant injection velocity. At reference speed for M=1.00, the coolant has approximately the same relative velocity of the mainstream flow. Under these circumstances the coolant provides optimum protection to the platform but due to the modification of the mainstream flow on the platform, the magnitude of heat transfer increases from the no blow condition. This effect is clearly seen for all blowing ratios which show an increase in heat transfer as compared to the M=0.0 case. At M=0.75, the coolant mass does not have sufficient momentum to alter the flow as much as the M=1.00 and hence the heat transfer magnitudes are lower. Heat transfer also decreases as the blowing ratio is increased as the coolant mixes with the mainstream flow as soon as it is injected and the flow near the platform surface is minimally affected. The quality of data near the holes and near the blade root and hub intersection is also greatly influenced by the unavoidable non-uniformity in the supplied heat flux. High heat transfer coefficient near the leading edge and very close to the trailing edge is also in part to the flow disturbance caused by the heater edge while mounted on the rotor platform. Though this is maintained as minimal as possible during assembly, the minute edge will influence the flow and in turn the heat transfer in that region. Data close to the trailing edge suction side is also affected by the presence of heater power input terminals and appears as non uniform heat transfer coefficient distribution.

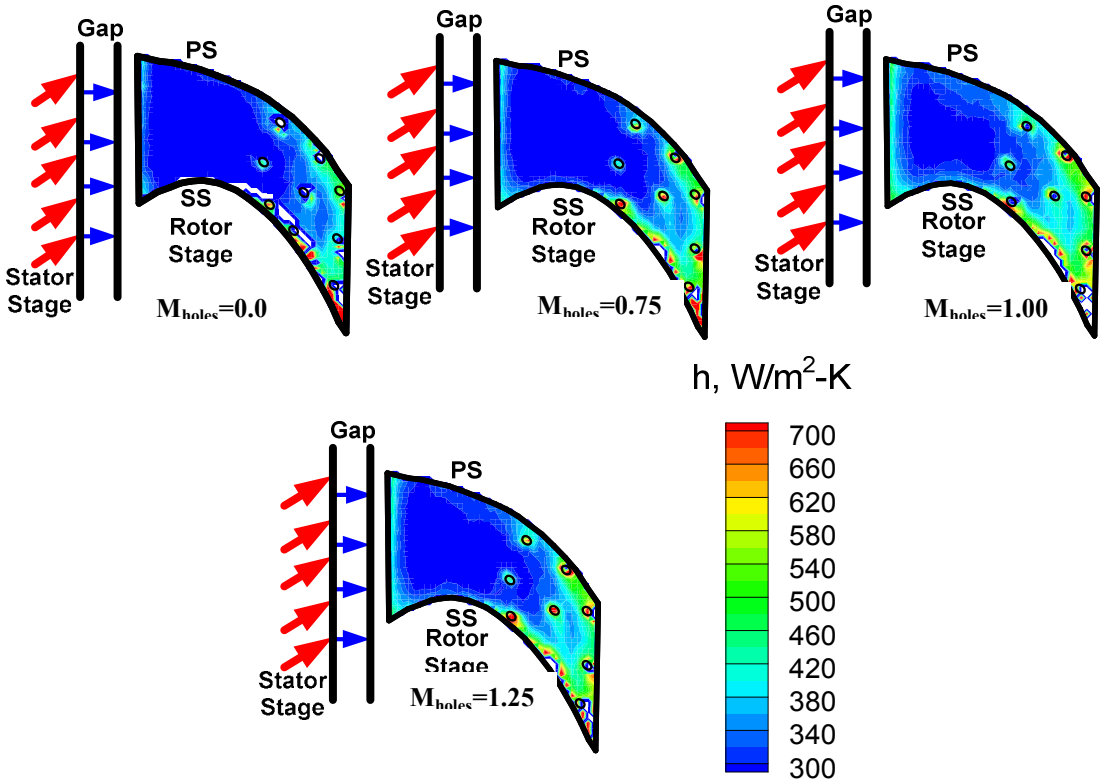

Figure 35: Heat Transfer Coefficient Distribution from Downstream Discrete Hole Coolant Injection on the Rotating Endwall for 2400rpm.

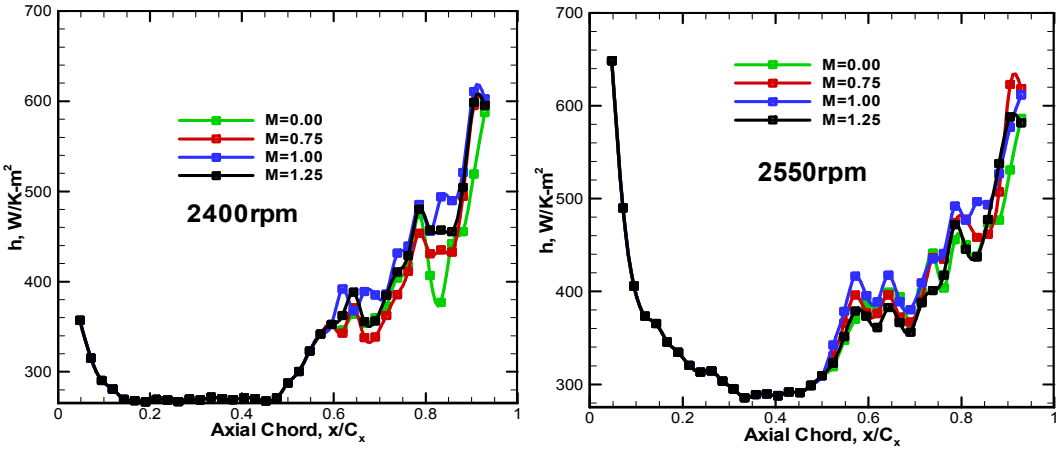

Figure 36: Pitchwise Averaged Film Cooling Effectiveness Distribution along Axial Chord for Different Turbine Rotating Speeds (Blowing Ratio Effect).

5.2.2.2 Downstream Injection at Lower Rotational Speeds

At lower rotational speeds than the reference, the stagnation location on the blade leading edge moves to the pressure side and alters the flow accordingly in the downstream region. Coolant injection which is mainly influenced by the mainstream flow will change depending on the angle of mainstream flow as it enters blade passage. Figure 35 shows the contour plot of the rotor platform heat transfer coefficient for a rotational speed of 2400rpm and blowing ratios of M=0, 0.75, 1.0 and 1.25. The coolant flow and distribution patterns are observed to be similar to that for the reference rotating case though the magnitudes are considerably lower and in the range of 450 to 550 W/m^2-K at most locations. Blowing ratio of M=1.25 has better coolant spread and higher heat transfer as higher coolant mass has a greater momentum approaching that at M=1.00 at the reference speed. This allows it to affect the mainstream flow more than at M=0.75. On the contrary at M=0.75, the lower coolant mass is incapable of penetrating the platform boundary layer leading to lower minimal flow alteration and lower heat transfer rates. The coolant once again migrates from the pressure to the suction surface. The central hole in column two is influenced to the minimum by the variations in heat flux supplied by the heater and hence the coolant trace is distinct and clear.

5.2.2.3 Pitchwise Averaged Heat Transfer Coefficients with Downstream Discrete Hole Injection

Figure 36 shows the pitchwise averaged heat transfer coefficients for all the blowing ratios at 2400rpm and 2550rpm. This figure assists in understanding the effects of blowing ratio at the two rotational speeds better by augmenting the earlier discussion for contour plots. For both the rotational speeds it is observed that there is an optimum coolant velocity or coolant mass that offers higher heat transfers. For 2400rpm, that blowing ratio appears to fall between M=1.00 and 1.25 while for the reference speed it is closer to M=1.00. From previous film cooling studies, it is observed that the best platform protection is obtained under these conditions where the coolant has a higher film cooling effectiveness and better spread on the platform surface though any injection accentuates the heat transfer coefficients. The effects of rotation on heat transfer coefficients due to hole injection for different blowing ratios is shown

in Figure 37. Observing the plot for M=0.0 itself clearly suggests that rotation amplifies the magnitude of heat transfer coefficients on the rotor platform and the same carries over to the coolant injection case. The 'h' values are lower for the lower rotational speed as the tangential velocity of mainstream as well as coolant flow is smaller than the higher reference speed.

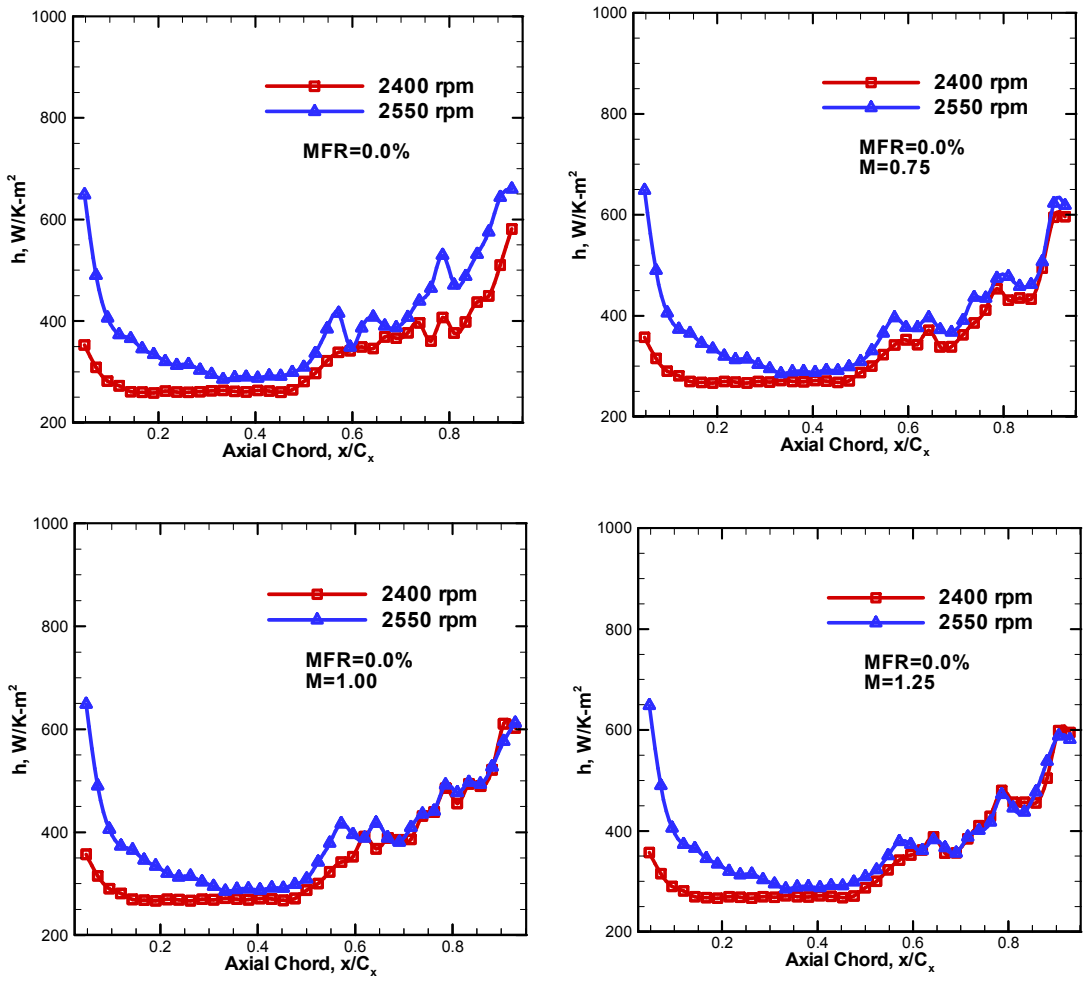

Figure 37: Pitchwise Averaged Heat Transfer Coefficient Distribution along Axial Chord for Different Turbine Rotating Speeds (Blowing Ratio Effect).

5.3 Aerodynamic Flow Measurements

5.3.1 Interstage Instrumentation

To achieve a high degree of versatility, the turbine facility has provision for radial aerodynamic measurements at inlet and exit of each blade row and circumferential measurements at first stage rotor exit, second stage stator and rotor exits. The turbine was designed with three T-rings for sealing the three 90° circumferential traverse slots used for aerodynamic measurements. The sealed T-rings move circumferentially inside these slots and effectively prevent the leakage of mass flow through them. Five-hole probes can be mounted on each of the three traversing systems which have stepper motors with encoders for accurate probe positioning. Three traversing systems have in all seven axes between them: 3 axes for radial traverse, 1 axis for circumferential traverse and 3 axes for actively aligning the probes, whenever the flow angle is out of the calibration range. This is particularly necessary when the probe is close to the hub or tip. The traverse in the radial direction spans from 1mm below the hub diameter to 1mm above the blade tip.

5.3.2 Aerodynamic Flow Measurement – Probe Set-up Instructions

Aerodynamic flow measurements were performed at different stages within the turbine to quantify the flow at different rotational speeds. Five-hole probes calibrated for ±20° in pitch and yaw were traversed radially from hub to tip at an interval of 1mm up to 5% of the blade near the hub and tip and 2mm in the central region to obtain accurate pressure, velocity and flow-angle distributions. The precise alignment of the five-hole probe with the direction of flow is necessary to ensure the accuracy of the data acquired. To enable proper probe alignment, a stepper motor along with a worm-gear arrangement was used to actively rotate and adjust the five-hole probe inside the turbine especially near the hub and the tip where the flow angles can change rapidly. To determine the precise rotational angle of 5-hole probe alignment along the blade length, the probe is first radially traversed in different regions till the magnitude of flow angles and velocities are reasonable. Once this is accomplished, the difference in this angle with the initial reference angle for each rotational speed is noted and is incorporated into the probe alignment during actual tests and also I the data analysis as described in Schobeiri et al. ([1] and [2]). The rotational stepper motors are

controlled using Intelligent Motion Systems© controller and the accompanying software to obtain high resolution angular positioning. Once the initial reference position of the probe is known, the probe alignment angle can be determined by a simple calculation.

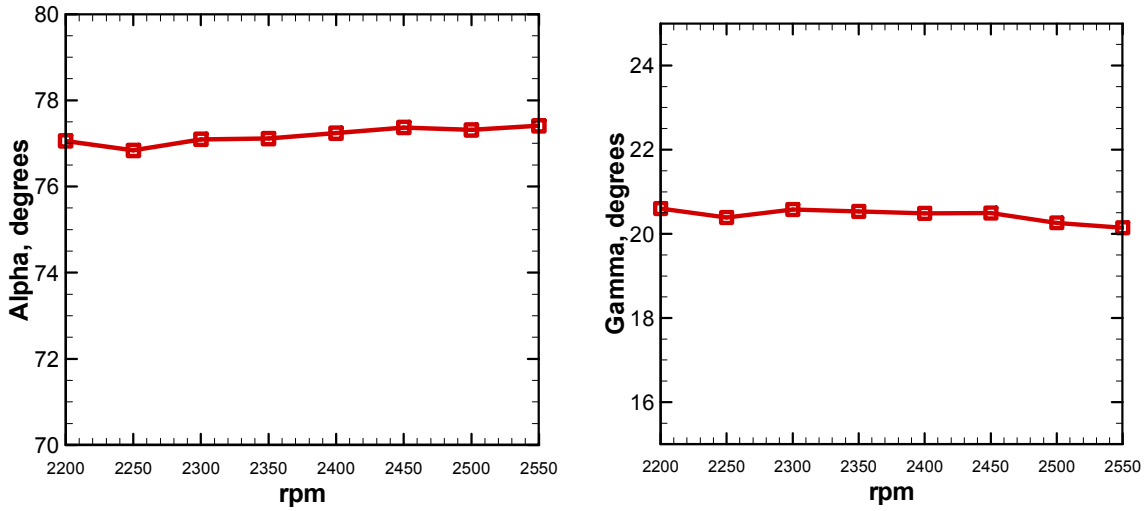

Figure 38: Variation of Absolute Flow Angle, Alpha, and Meridional Flow Angle, Gamma, with Rotor Speed at the Stator-Rotor Gap Exit, MFR=1.00%.

5.3.3 Aerodynamic Flow Measurement – Results and Discussion

Aerodynamic measurements were performed on the first stage stator exit using a 25° angular probe to measure the coolant flow out of the upstream stator rotor gap. As mentioned earlier, the slot width in the radial direction is 2.3 mm and since the probe head diameter is 1mm, only one data point could be acquired close to the endwall immediately after the slot. Also, the axial location of the probe head tip from the slot exit is approximately 2mm. The probe was aligned in the axial direction to the turbine and this angle was considered to be 90º, the reference angle. At zero rotational speed it was observed that the flow followed the stator rotor slot pitch angle of 25º and ejected out of the slot in the axial direction.

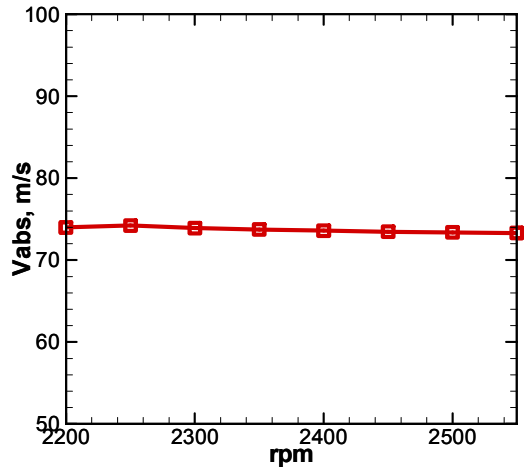

Figure 39: Variation of Absolute Flow Velocity with Rotor Speed at the Stator-Rotor Gap Exit, MFR=1.00%.

To study the effects of rotation on coolant flow exiting the stator rotor gap, the miniature angular 5-hole probe was positioned precisely at the slots entrance and aerodynamic measurements were performed for an MFR=1.0% and varying the rotor speed between 2200rpm and 2600rpm. Figure 38 shows the effects of rotation on the yaw (alpha) and pitch (gamma) angles of the coolant injected through the upstream slot on the platform immediately after the first stage stator exit at different rotor speeds. As seen from the graphs, at 2200rpm, the yaw angle is approximately 77º. The initiation of rotation draws the coolant tangentially in the direction of rotation by approximately 13º from the turbine axis. Increasing the rotation speed further up to 2600rpm changes alpha only slightly. This is due to the fact that the location of measurement is very close to the slot and the coolant flow has little time to be affected significantly with changes in rotational speeds. To be able to further accurately measure the rotational effects on the platform coolant flow, aerodynamic measurements need to be performed further downstream of the coolant slot. Introduction of rotation appears to suppress the pitch angle gamma of the coolant from a no rotation angle of 25 º to 22º with rotation over the entire measured speed range. The mainstream flow acts on the exiting coolant and lowers the angle at which the coolant ejects on to the platform. Figure 39 and Figure 40 show

the absolute and circumferential velocity variation at the stator-rotor gap exit for an MFR=1.0% and different rotor speeds.

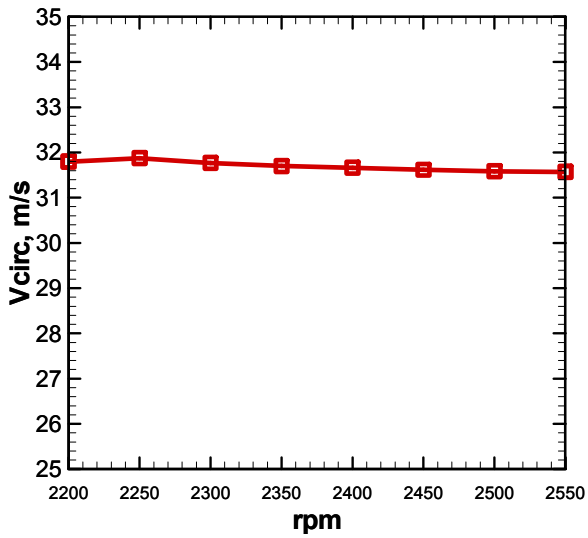

Figure 40: Variation of Circumferential Flow Velocity with Rotor Speed at the Stator-Rotor Gap Exit, MFR=1.00%.

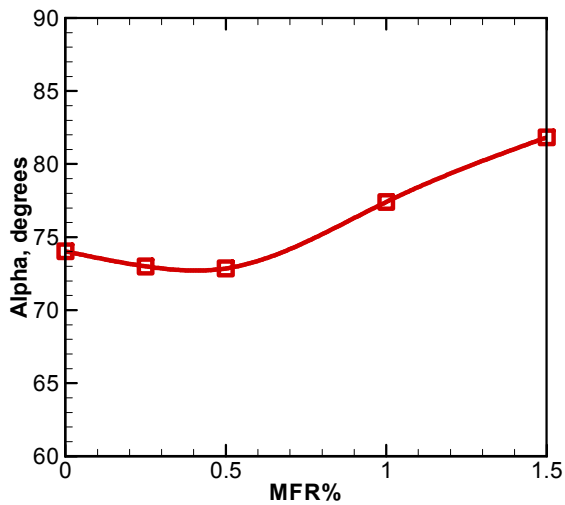

Figure 41: Variation of Absolute Flow Angle, Alpha, with MFR at the Stator-Rotor Gap Exit, 2550rpm.

It is clearly seen that the effect of rotation has little to no effect on the coolant velocity very close to the slot exit. The non dimensionalized circumferential velocity distribution of the coolant decreases a little with rotation but the change is very small. With no rotation, the absolute velocity of the coolant was determined to be around 7-8m/s for MFR=1.0%.

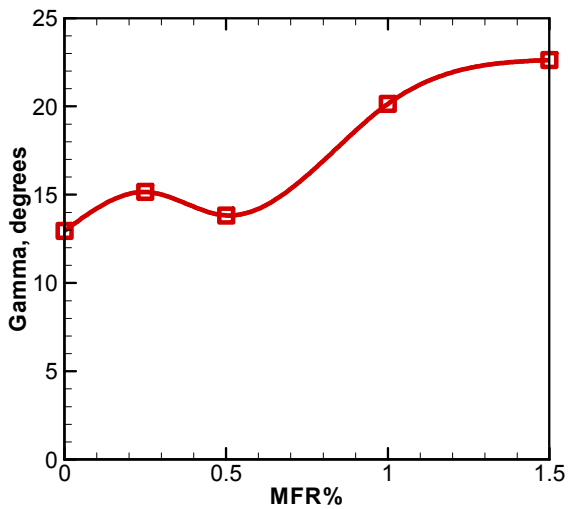

Figure 42: Variation of Meridional Flow Angle, Gamma, with MFR at the Stator-Rotor Gap Exit, 2550rpm.

To understand the effects of rotation on the mass flow ratios, aerodynamic measurements were performed at the gap exit at 2550rpm for MFR corresponding to 0%, 0.25%, 0.5%, 1.0% and 1.5%. As seen from Figure 41 at MFR=0%, alpha follows the solid angle of the stator following approximately the path of the mainstream flow. As the MFR is increased, the momentum of the coolant counteracts the effects of the mainstream flow and moves towards the turbine axis. At MFR=1.5, the coolant further moves towards the axial direction and the coolant yaw angle alpha for this MFR is approximately 80º. The gamma or the pitch angle (Figure 42) shows a general trend of increasing as the MFR increases and approaches the slot angle of 25º for an MFR=1.5%. Once again the momentum of the coolant at higher

MFR forces the coolant towards the metallic angle of the slot by negating to a certain extent the effects of the mainstream flow and rotation. The non dimensionalized circumferential velocity of the coolant increases a little at the exit of the slot as the MFR is increased (Figure 43).

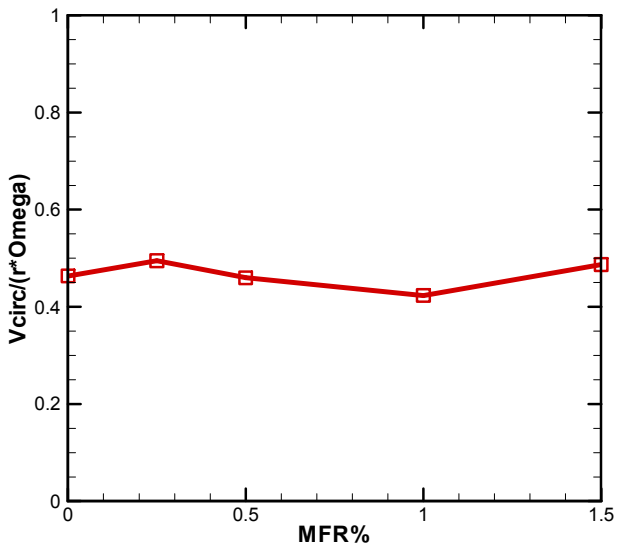

Figure 43: Variation of Non-Dimensionalized Circumferential Velocity, with MFR at the Stator-Rotor Gap Exit, 2550rpm.

Interstage measurements were conducted along the first stage rotor exit, second stage stator exit and the second stage rotor exit to demonstrate the usage and applicability of the little stepper motors. As explained earlier, prior to the main tests, radial aerodynamic measurements were performed till the appropriate angles for the 5-hole probe alignment were determined for each stage. It was found that the fluctuations near the hub and tip necessitated an angular re-adjustment between 4º-6º for each stage from that of the remaining 80% of the blade length. Figure 44 shows the absolute, relative and meridional flow angle at each of the three stations at 2550rpm. The absolute angle at the stator exit is approximately the

metal angle of the stator blade of 19º. The probes were aligned as accurately as possible to obtain smooth results near the hub and tip. The radial absolute velocity (Figure 44) at the stator exit was approximately equal to a Mach number of 0.1 while at the rotor exit it was 0.3.

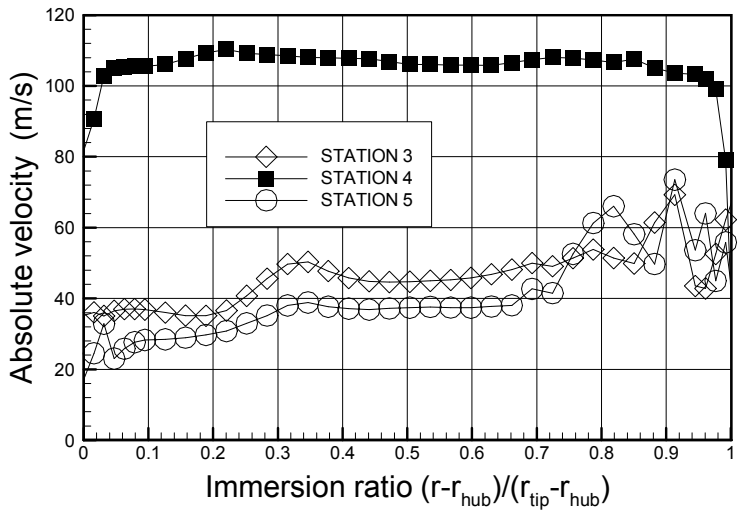

Figure 44: Radial Distribution of Absolute Flow Velocity, 2550rpm.

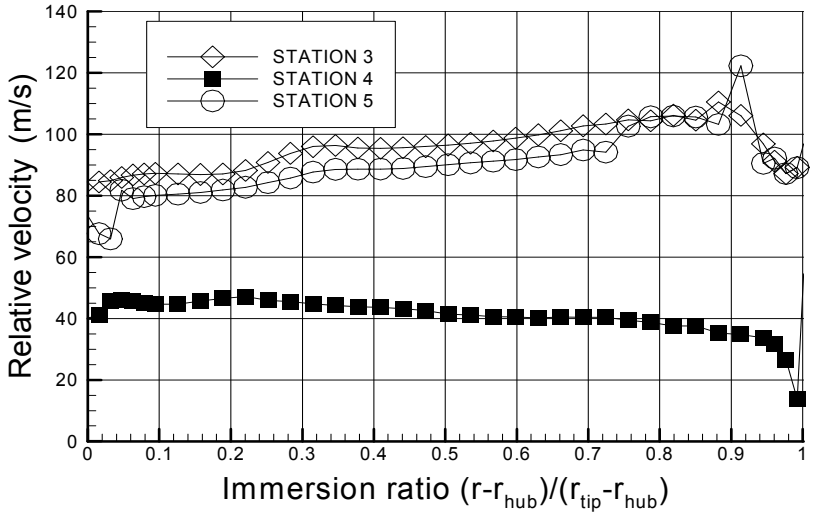

Figure 45: Radial Distribution of Relative Flow Velocity, 2550rpm.

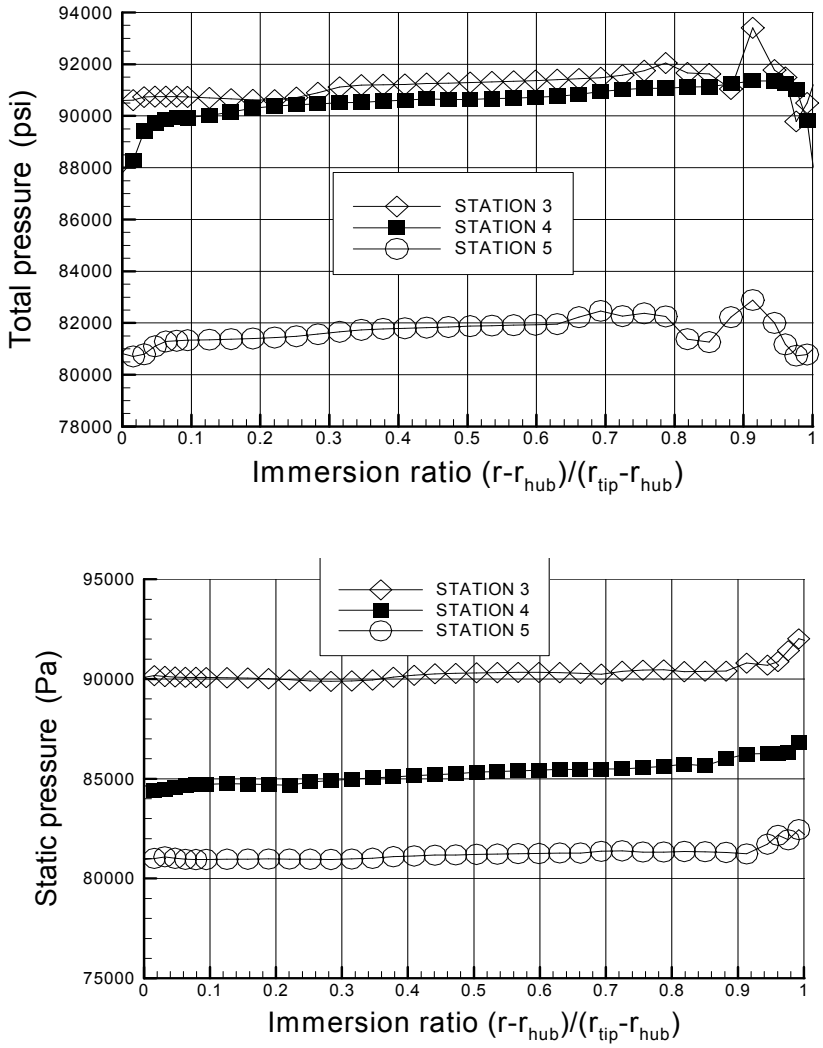

Figure 46: Radial Distribution of Total and Static Pressures, 2550rpm.

The velocity distribution for the rotor near the hub and the tip show more fluctuations than for the stator due to the complexity of flow which is further accentuated by the rotation. Figure 45 shows the radial relative velocity distribution for mainstream flow at 2550rpm. The profile is uniform between 5% and 95% of the blade length. Close to the hub and tip higher variations are observed than in the blade mid-

section. The total and static pressure along the radial direction along the three turbine stations are shown in Figure 46. The pressures are lower than atmospheric as expected in a turbine stage and the fluctuations near the hub and tip have been measured more accurately than previously obtained on the same facility due to the presence of the angular stepper motors. To eliminate this completely, instantaneous aerodynamic measurements using either hot film probes or piezoelectric fast response probes need to be utilized.

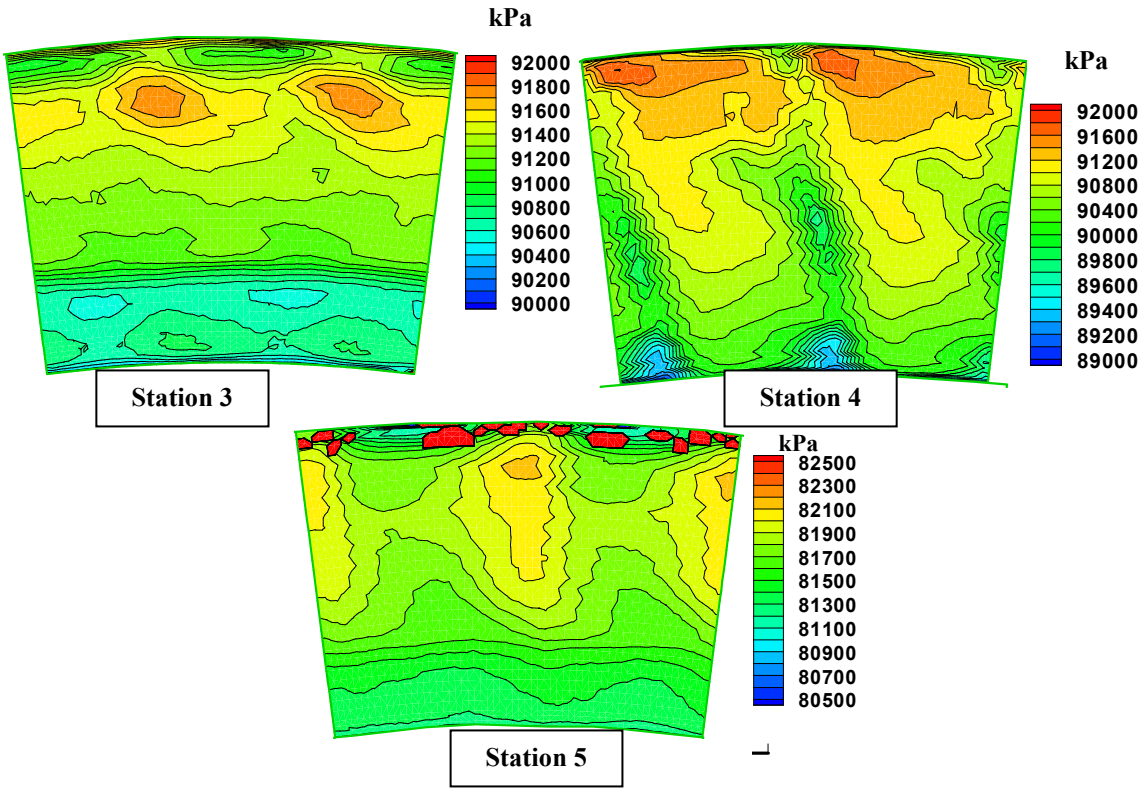

Figure 47: Contour Plots of Total Pressure Distribution, 2550rpm.

Contour plots of the absolute total pressures for the combined radial and circumferential traverse at each of the stations for 2550rpm is as shown in Figure 47. The average of these pressures at each location

provides the radial distributions discussed in the previous section. The circumferential traverse covers two blade spans and can be seen in the contour plots. The blade trailing edge and the region in between can be discerned clearly on the contour plots by looking at the pressure variation as the blade passes by the 5-hole probe. Contour plots for static pressure distribution for the same stations are shown in Figure 48.

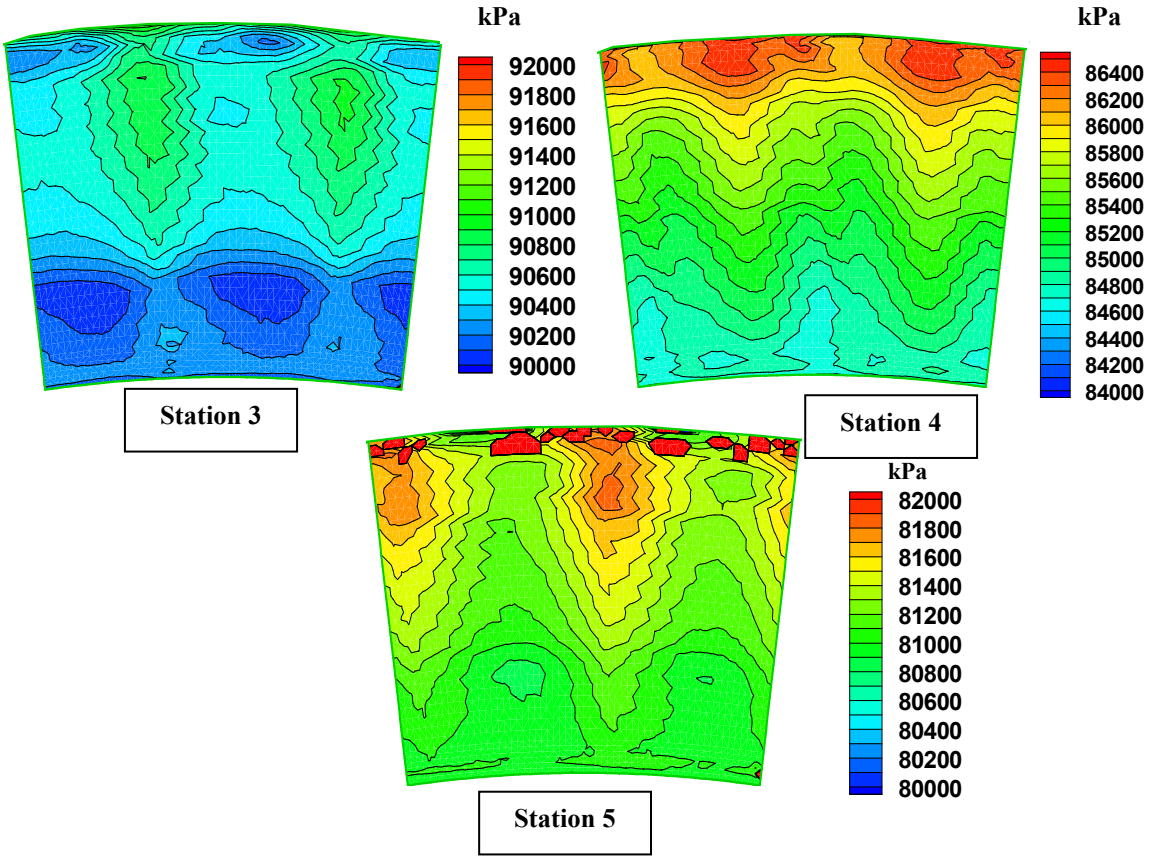

Figure 48: Contour Plot Distribution of Static Pressure Distribution, 2550rpm.

6. UNCERTAINTY ANALYSIS

6.1 Uncertainty Analysis for Aerodynamic Measurements Using 5-Hole Pitot Probes

Uncertainty analysis is performed for the 5-hole Pitot probes after calibration and data reduction based on the method suggested by Kline-McClintock [102]. This method outlines the procedure to calculate the total uncertainty on a variable by calculating the uncertainties on the individual components that constitute the calculation of the variable. The magnitude of error calculated by this process can also be described as the maximum error one can expect in the calculated variable. The results of this analysis along with the process of uncertainty determination are as shown below. Further details used in the determination of the individual uncertainties are presented in Appendix F.

As suggested by the adopted procedure, the uncertainties in each of the parameters measured were calculated using the following equation:

$$w_R = \sqrt{\left[\frac{\partial R}{\partial x_1} w_1\right]^2 + \left[\frac{\partial R}{\partial x_2} w_2\right]^2 \ldots + \left[\frac{\partial R}{\partial x_n} w_n\right]^2} \tag{16}$$

where R is the equation used to calculate the magnitude of the variables x_i. Hence, $R=f(x_1,x_2,x_3,x_4,\ldots,x_n)$ and the measurement uncertainty in each independent variable x_n is given by w_n. Equation 16 modified to apply to our calibration is as shown in equation 17.

$$w_v = \sqrt{\left[\frac{\partial V}{\partial P} w_P\right]^2 + \left[\frac{\partial V}{\partial \rho} w_\rho\right]^2 + \left[\frac{\partial V}{\partial D_{in}} w_{Dni}\right]^2 + \left[\frac{\partial V}{\partial D_{ou}} w_{Dou}\right]^2} \tag{17}$$

where, wp is the uncertainty in the pressures measured by the 5-hole probe through the PSI pressure transducer, w_ρ is the uncertainty in the calculation of flow density, $w_{D_{in}}$ and $w_{D_{ou}}$ are the uncertainty in the measurement of the nozzle inside and outside diameters using a Vernier caliper. The velocity of the

flow in the calibration facility is calculated from simplified Bernoulli's principle and is as shown in equation 18.

$$V = \sqrt{\frac{2P}{\rho\left[1-\left(\frac{D_{ou}}{D_{in}}\right)^2\right]}} \tag{18}$$

Now to calculate the uncertainties on the actual experimental velocity results, the calibration error is added to the velocities calculated from the experimental pressure measurements from the five hole probes. Thus the equation shown in 16 is applied to each of the equations ([93]) used to calculate the two flow angles, total and static pressures and the absolute velocity using a previously used MathCAD® program to obtain the actual experimental uncertainty. The experimental variation in pressure measurement is approximately 0.5 Pa from the pressure transducers and 1°C for temperature measurements, these values are then utilized in the uncertainty equations of the corresponding parameters to obtain the uncertainties in the parameters measured using the five hole probes. The maximum uncertainties of all the independent parameters measured are thus calculated and are as shown in table 2.

Table 2: Uncertainty analysis for the miniature 5-hole probes.

Probe Number	% Uncertainty in Pitch	% Uncertainty in Yaw	% Uncertainty in Total Pressure	% Uncertainty in Static Pressure	% Uncertainty in Absolute Velocity
Probe 1	2.72	2.44	1.23	1.57	2.47
Probe 2	1.95	1.88	0.96	1.11	2.33
Probe 3	2.83	3.01	1.46	1.49	2.65

6.2 Uncertainty Analysis for Film Cooling Effectiveness Measurements Using PSP

The primary reasons for any PSP measurements like in any other experiments are again due to the individual errors from the instruments used in the calibration and in data acquisition. To minimize such errors, the calibration set up was as closely replicated to the main test set-up including the instruments and the wiring. In addition, things beyond control like dust, paint deterioration and error in reference image measurement, however minimal they might be, can contribute to an increase in the uncertainty of the data. Kline McClintok's [102] uncertainty calculation can again be modified for error calculation for PSP and the corresponding equation with the significant terms is as shown below:

$$w_p = \sqrt{w_{cal}^2 + \left[w_I \frac{\partial P}{\partial I} \right]^2 + \left[w_T \frac{\partial P}{\partial T} \right]^2} \tag{19}$$

where, w_{cal} is the error in calibration while maintaining the vacuum and temperatures in the vacuum chamber, w_I is the error in image intensity measurement associated with the optical setup and the electronics of the data acquisition system and w_T is the error in temperature measurement during data acquisition. Here, the errors associated with temperature effects of PSP can be neglected due to the following reasoning. Error in PSP measurements can be significantly enhanced if the reference temperature during calibration is different from the temperature at which reference image is acquired during actual data collection. This is minimised by acquiring the reference image immediately after data collection which should be the same as the reference temperature used during calibration analysis. Hence, the uncertainty in PSP for the current experiments depends on the calibration uncertainty and intensity measurements during experimentation. Uncertainty calculations for all PSP measurements were performed based on a confidence level of 95% and are based on the uncertainty analysis method suggested by Kline McClintock [102] and Coleman and Steele [104]. Lower effectiveness magnitudes have higher uncertainties. For an effectiveness magnitude of 0.8, uncertainty was around 1% while for effectiveness magnitude of 0.07, uncertainty was as high as 10.3%. This uncertainty is the cumulative result of uncertainties in calibration and data acquisition. Uncertainties for very low effectiveness magnitudes are

higher as the magnitude of noise from the camera and the system start approaching the actual intensity of data. Uncertainty for the average blowing ratio calculations is estimated to be approximately 3.5 % and is discussed in detail by Holman [103]. The relevant programs and further details are provided in Appendix F.

6.3 Uncertainty Analysis for Heat Transfer Measurements Using TSP

TSP measurements are significantly affected by the same parameters which introduce uncertainties in PSP, except that TSP is not sensitive to pressure changes like PSP is to temperature changes, implying that the reference image can be acquired at atmospheric pressures. Once again, the same set optical setup used for calibration is used for image acquisition during actual experiments. Thermocouples at different locations on the platform surface monitor and assist in maintaining the required surface and coolant temperatures and thereby decreasing the actual experimental errors. Kline-McClintock's [102] equation modified for TSP analysis is as shown below:

$$w_T = \sqrt{w_{cal}^2 + \left[w_I \frac{\partial T}{\partial I} \right]^2} \tag{20}$$

w_T is the total uncertainty in temperature measurements using TSP, w_{cal} is uncertainty during calibration and is dependent on the uncertainty of the thermocouples which is 0.5ºC. Calibration error is also dependent on the uncertainty in the high accuracy digital power supply used to power the heater. w_I is the uncertainty in the intensity measurements during actual experiments. Uncertainty calculations for all TSP measurements was also performed based on a confidence level of 95% using the method suggested by Coleman and Steele [104] and was determined to be around 6.3% on the temperature arising out of calibration and image uncertainties. As mentioned earlier in the PSP section, the blowing ratio and had uncertainties of 3.5% arising from the flow measurements using the rotameter and hole diameter measurements using a digital Vernier calipers.

7. SUMMARY AND CONCLUSIONS

Experiments were performed for film cooling effectiveness obtained from purging of coolant through the wheel space cavity on the first stage of a rotating platform of a three stage model turbine facility. Film cooling effectiveness results were obtained for 4 different coolant-to-mainstream mass flow ratios. Engine operation at reference and lower rotational speeds was investigated for all mass flow ratios. The main conclusions from this study are summarized below:

7.1 Film Cooling Effectiveness Measurements Using PSP

7.1.1 Stator- Rotor Gap Coolant Injection

1. The new research turbine facility provides the basic features to extract information relevant to gas turbine design community. These features are (a) stator-rotor unsteady interaction, (b) blade and platform rotation including the relative blade circulation and the exposure of the platform boundary layer to centrifugal and coriolis forces, and (c) the flow acceleration. Except for the last feature (c), none of the above features can be simulated in a cascade investigation.
2. Film cooling effectiveness due to coolant injection from the stator-rotor gap increases with increasing coolant-to-mainstream mass flow ratio.
3. Complete coverage of the passage platform cannot be obtained by using coolant injection from the stator-rotor gap. The passage vortex over the platform has an adverse impact on film adherence.
4. Film coolant traces are reoriented more towards the suction side for lower speeds than that observed for reference condition due to the stagnation region shift towards the pressure side.
5. Film cooling effectiveness increases with rotational speed for all the considered coolant mass flow ratios.

6. The film cooling effectiveness on the blade platform decays much more rapidly than that observed in studies with film cooling on a flat stationary surface, primarily due to the presence of the passage vortex.

7.1.2 Downstream Discrete Hole Coolant Injection

Film cooling effectiveness measurements were performed on a rotating platform using PSP technique. Rotational speeds of 2400rpm, 2550rpm and 3000rpm were considered for the experiments to determine the effects of rotation on platform film cooling. Film cooling effectiveness was quantified for downstream discrete hole film cooling for M_{holes}=0.5, 0.75, 1.00, 1.25, 1.50, 1.75 and 2.00. Film cooling effectiveness and coolant coverage on the rotor platform due to coolant ejection through downstream holes is maximum for the reference speed of 2550rpm.

1. M_{holes} between 0.75 and 1.25 provided the best protection on the rotor platform for all three rotational speeds. Coolant coverage and effectiveness magnitudes were highest at these blowing ratios than the others tested. This result confirms that the M_{holes} one not only provides the best film coverage, but also minimizes the aerodynamic losses due to mixing of the cooling jets with the main flow.
2. Two downstream film cooling holes (1 and 4 in Fig. 7) were affected more by the passage vortex than the other cooling holes owing to their position on the rotor platform.
3. Secondary flow from the blade pressure surface to the suction surface is strongly affected by the rotational motion causing the coolant traces from the holes to clearly flow towards the suction surface.
4. Complete film cooling protection on a rotating platform can be provided with combined upstream stator-rotor gap ejection and discrete hole ejection. Positioning the holes with angles oriented more towards the pressure surface will help reduce the effects of passage vortex and cross flow.

7.1.3 Combined Upstream Stator-Rotor Gap and Downstream Discrete Hole Coolant Injection

Further, combined film cooling tests were performed for an upstream stator-rotor gap purge flow ejection and downstream discrete hole coolant ejection at MFR=1.00% and M_{holes}=0.75, 1.00 and 1.25. The results of this research work are summarized as follows:

1. To optimize coolant usage, maintaining the stator-rotor gap injection close to MFR=1% and increasing the number of holes on the platform without compromising the structural integrity is the way forward in providing proper film protection on the platform.
2. The upstream and downstream injection provided good coolant coverage on the rotor platform for an MFR=1.00% and M_{holes} close to one.
3. The film cooling effectiveness magnitudes reflected the results shown due to individual coolant injection cases, hence, can be concluded that for the cases tested, there was minimal interaction between the two injection forms.

7.2 Heat Transfer Coefficients Measurement Using TSP

Heat transfer measurements using temperature sensitive paint was performed for rotor platform for MFR corresponding to 0%, 0.5%, 1.5% and 2.0% upstream injection for rotational speed of 2400rpm and reference speed of 2550rpm. For the downstream coolant hole case M_{holes}= 0.75, 1.00 and 1.25 were considered at the same rotational speed. The following are the results of those experiments:

1. Heat transfer coefficient distribution on the rotor platform increases with rotor frequency for upstream coolant injection.
2. The heat transfer magnitudes for MFR=2% is the highest and in the range of 400-600W/m^2-K
3. 'h' also tends to increase for higher coolant injection rates through downstream discrete holes.
4. The coefficients appear to be maximum along the coolant flow path as they flow towards the trailing edge.

7.3 Aerodynamic Measurements

Aerodynamic measurements were performed to compliment the heat transfer and film cooling experiments at the first stage stator exit along the stator rotor gap plane. Effects of rotation on the coolant

flow angles very close to the gap were studied to analyze the coolant distribution on the rotor platform. Also interstage measurements were conducted to quantify the velocity, flow angles and pressure distributions in the radial and circumferential direction. The results of those experiments have been summarized below:

1. With no rotation, the coolant ejects out of the stator rotor gap along the rotor axis.
2. Introduction of rotation causes the coolant flow close to the stator-rotor gap to reorient in the direction of flow by approximately 13º from the turbine axis.
3. Beyond the initial reorientation, the change in coolant direction with rotational speeds up to 2600 is negligible.
4. For zero rotation, the coolant also follows the solid angle (25 º) of the stator-rotor gap.
5. At 2550rpm, the angle at which coolant comes out of the gap are lower for the lower injection rates and approaches the solid angle of 25º as the MFR if closer to 1.5%.
6. A system for probe fine alignment for all the aerodynamic measurements was established using a worm gear arrangement and controlled stepper motor in addition to the already existing 6 axes traverse system. The system enabled precise positioning of the 5 hole Pitot probe close to the rotor hub and tip for accurate velocity, flow angle and pressure measurements.

Essentially, this work provides detailed data on aerodynamics, film cooling and heat transfer performance on a rotating platform for the first time in open literature. It has also been established that with accurate adjustment of the 5-hole probes using the stepper motor-controller set-up, more reliable and accurate data can be acquired. By utilizing these results for film cooling, heat transfer and aerodynamics, turbine researchers and designers will be better equipped with knowledge for providing efficient cooling and protection to the rotor platform.

7.4 Future Investigation

Using the pressure sensitive paint technique, the film cooling effectiveness has been measured on the rotating platform with coolant flow from the stator-rotor seal. Film effectiveness has also been measured with coolant from discrete film cooling holes. To complement the above test cases, a combined case with simultaneous stator-rotor gap and discrete hole injection has also been experimented with to determine the interaction between the two methods of cooling and to best provide for platform cooling. This will provide engineers with detailed film cooling effectiveness distributions under more realistic coolant flow conditions. Heat transfer under rotation has been studied for upstream stator-rotor seal injection and downstream hole injection. In all the above cases, it has been noticed rotation significantly affects the coolant distribution and the heat transfer from the mainstream flow to the platform due to its effects on the platform secondary flow. Contouring of the platform is found to alter the secondary flow and also minimize the aerodynamic losses.

In the future, the effects of such contouring on platform heat transfer and film cooling with different configurations of the contours and coolant holes can be studied extensively with the already established PSP and TSP techniques with some changes to the existing rotor. Also, with the available equipment and measurement techniques, similar aerodynamic, film cooling effectiveness and heat transfer measurements can be performed for rotor blade tip with different tip configurations. Also, to capture the turbulence effects within the turbine, aerodynamic study with hot films is recommended.

REFERENCES

[1] Schobeiri, M. T., 1999, "Efficiency, Performance and Flow Measurement of Siemens-Westinghouse HP-Turbine Blades," Final Report Westinghouse, Series 9600 and 5600.

[2] Schobeiri, M. T., Gilarranz, J.L, Johansen, E.S., 2000, "Aerodynamic and Performance Studies of a Three Stage High Pressure Research Turbine with 3-D Blades, Design Points and Off-Design Experimental Investigations," ASME Paper No. 2000-GT-484.

[3] Schobeiri, M.T., Suryanarayanan A., Jermann, C., and Neuenschwander, T., 2004, "A Comparative Aerodynamic and Performance Study of a Three-Stage High Pressure Turbine with 3-D Bowed Blades and Cylindrical Blades," ASME Paper No. GT-2004-53650.

[4] Wright, L., Schobeiri, M.T., 1999, "Effect of Periodic Unsteady Flow on Boundary Layer and Heat Transfer on a Curved Surface," ASME Transactions, Journal of Heat Transfer, **120**, pp. 22-33.

[5] Ristic, B., Lakshminarayana, B., and Chu, S., 1998, "Three Dimensional Flow Field Downstream of an Axial-Flow Turbine Rotor," AIAA Paper No. 98-3572.

[6] Lakshminarayana, B., 1996, *Fluid Dynamics and Heat Transfer of Turbomachinery*, John Wiley & Sons, New York.

[7] Schobeiri, M., 2005, *Turbomachinery Flow Physics and Dynamic Performance*, Springer-Verlag, New York.

[8] Denton, J. D., 1993, "Loss Mechanisms in Turbomachines," ASME J. of Turbomachinery, **115**, pp. 621–656.

[9] Langston, L.S., 1980, "Crossflow in a Turbine Cascade Passage," ASME J. of Engineering & Power, **102**, pp. 866-874.

[10] Goldstein, R.J., and Spores, R.A., 1988, "Turbulent Transport on the Endwall in the Region between Adjacent Turbine Blades," ASME J. of Heat Transfer, **110**, pp. 862-869.

[11] Takeishi, K., Matsuura, M., Aoki, S., and Sato, T., 1990, "An Experimental Study of Heat Transfer and Film Cooling on Low Aspect Ratio Turbine Nozzles," ASME J. of Turbomachinery, **112**, pp. 488-496.

[12] Sieverding, C.H., 1985, "Recent progress in the Understanding of Basic Aspects of Secondary Flows in Turbine Blade Passages"' J. for Engineering for Gas Turbines and Power, **107**, pp.248-257

[13] Herzig, H. Z., Hansen, A. G. and Costello, G. R., Feb. 1953, "A Visualisation Study of Secondary Flows in Cascades," NACA Report No. 1163.

[14] Wang, H. P., Olson, S. J., Goldstein, R. J. and Eckert E. G., 1995, "Flow Visualization in a Linear Turbine Cascade of High Performance Turbine Blades," ASME Paper no. 95-GT-7.

[15] Reid, K., Denton, J., Pullan, G., Curtis, E., and Longley, J., 2005, "The Interaction of Turbine Inter-platform Leakage Flow with the Mainstream Flow," ASME Paper No. GT2005-68151.

[16] Bindon, J.P., 1989," The Measurement and Formation of Tip Clearance Loss," ASME, Journal of Turbomachinery, **111**, pp. 257-263.

[17] Han, J.C., Dutta, S., and Ekkad, S. V., 2000, *Gas Turbine Heat Transfer and Cooling Technology*, Taylor & Francis, New York.

[18] Simon, T. W. and Piggush, J. D., 2006, "Turbine Endwall Aerodynamics and Heat Transfer," AIAA J. of Propulsion and Power, **22**, (2), pp. 301-312.

[19] Bogard, D. G. and Thole, K. A., 2006, "Gas Turbine Film Cooling," AIAA J. of Propulsion and Power, **22**, (2), pp. 249-270.

[20] Paniagua, G., Denos, R., Almeida, S., 2004, "Effect of the Hub Endwall Cavity Flow on the Flow-Field of a Transonic High Pressure Turbine," J. of Turbomachinery, **128**, pp. 578-586.

[21] Urbassik, R. M., Wolff, M. J., Polanka, M. D., 2006, "Unsteady Aerodynamics and Interactions between a High Pressure Turbine Vane and Rotor," J. of Turbomachinery, **128**, pp. 35-42.

[22] Han, S., Goldstein, R. J., 2006, "Influence of Blade Leading Edge Geometry on Turbine Endwall Heat (Mass) Transfer," J. of Turbomachinery, **128**, pp. 798-813.

[23] Praisner, T. J., Smith, C. R., 2006, "The Dynamics of the Horseshoe Vortex and Associated Endwall Heat Transfer-Part I: Temporal Behaviour," J. of Turbomachinery, **128**, pp. 741-754.

[24] Praisner, T. J., Smith, C. R., 2006, "The Dynamics of the Horseshoe Vortex and Associated Endwall Heat Transfer-Part II: Time –Mean Results," J. of Turbomachinery, **128**, pp. 755-762.

[25] Rehder, H. J., Dannhauer, A., 2007, "Experimental Investigation of Turbine Leakage Flows on The Three-Dimensional Flow Field and Endwall Heat Transfer," J. of Turbomachinery, **129**, pp. 608-618.

[26] Piggush, J. D., Simon, T. W., 2007, "Heat Transfer Measurements in a First Stage Nozzle Cascade having Endwall Contouring: Misalignment and Leakage Studies," J. of Turbomachinery, **129**, pp. 782-789.

[27] Reid, K., Denton, J., Pullman, G., Curtis, E., Longley, J., 2007, "The Interaction of Turbine Inter-Platform Leakage Flow with Mainstream Flow," J. of Turbomachinery, **129**, pp. 303-310.

[28] Leishman, B. A., Cumpsty, N. A., Denton, J. D., 2007, "Effects of Bleed Rate and Endwall Location on the Aerodynamic Behavior of a Circular Hole Bleed Off-Take," J. of Turbomachinery, **129**, pp. 645-658.

[29] Priddy, W. J., Bayley, F. J., 1985, "Effects of Free Stream Turbulence on the Distribution of Heat Transfer around Turbine Blade Sections," Int. J. Heat and Fluid Flow, **6**, (3), pp. 181-192.

[30] Martin, B. W., Brown, .A, 1979, "Factors Influencing Heat Transfer to the Pressure Surfaces of Gas Turbine Blades," Int. J. Heat and Fluid Flow, **1**, (3), pp. 107-114.

[31] Liu, Y., 2007, "Aerodynamics and Heat Transfer Predictions in a Highly Loaded Turbine Blade," Int. J. of Heat and Fluid Flow, **28**, pp. 932-937.

[32] Thakur, S., Wright, J., Shyy, W., 1998, "Convetive Film Cooling over a Representative Turbine Blade Leading Edge," Int. J. of Heat and Mass Transfer, **42**, pp. 2269-2285.

[33] Pasinato, H. D., Squires, K. D., Roy, R. P., 2004, "Measurements and Modelling of the Flow and Heat Transfer in a Contoured Vane-Endwall Passage," Int. J. Heat and Mass Transfer, **47**, pp. 5685-5702.

[34] Schook, R., De Lange, H. C., Van Steenhoven, A. A., 2000, "Heat Transfer Measurements in Transitional Boundary Layers," Int. J. of Heat and Mass Transfer, **44**, pp. 1019-1030.

[35] Liu, X., Rodi, W., 1991, "Experiments on Transition Boudary Layers with Wake Induced Unsteadiness," J. of Fluid Mechanics, **231**, pp. 229-256.

[36] Al-Hamadi, A. K., Jubran, B. A., Theodoridis, G., 1998, "Turbulence Intensity Effects on Film Cooling and Heat Transfer from Compound Angle Holes with Particular Application to Gas Turbine Blades," Energy Convers. Mgmt., **39**, (14), pp. 1449-1457.

[37] Mehendale, A. B., Ekkad, S. V., Han, J. C., 1994, "Mainstream Turbulence Effect on Film Effectiveness and Heat Transfer Coefficient of a Gas Turbine Blade with Air and Co_2 Film Injection," Int. J. of Heat and Mass Transfer, **37**, (17), pp. 2707-2714.

[38] Butler, R. J., Byerley, A. R., Van Treuren, K., Baughn, J. W., 2000, "The Effect of Turbulence Intensity and Length Scale on Low Pressure Turbine Blade Aerodynamics," Int. J. Heat and Fluid Flow, **22**, pp. 123-133.

[39] Han, J. C., Zhang, L., Ou, S., 1993, "Influence of Unsteady Wake on Heat Transfer Coefficient from a Gas Turbine," J. of Heat Transfer, **115**, pp. 904-911.

[40] Jenkins, S., Varadarajan, K., Bogard, D. G., 2004, "The Effects of Mainstream Turbulence and Turbine Vane Film Cooling on the Dispersion of a Simulated Hot Streak," J. of Turbomachinery, **126**, pp. 203-211.

[41] Giel, P. W., Boyle, R. J., Bunker, R. S., 2004, "Measurements and Predictions of Heat Transfer on Rotor Blades in a Transonic Turbine Cascade," J. of Turbomachinery, **126**, pp. 110-121.

[42] Nasir, H., Ekkad, S. V., Kontrovitz, D. M., Bunker, R. S., Prakash, C., 2004, "Effect of Tip Gap and Squealer Geometry on Detailed Heat Transfer Measurements Over a High Pressure Turbine Rotor Blade Tip," J. of Turbomachinery, **126**, pp. 221-228.

[43] Kohli, A., Bogard, D. G., 2008, "Improving Film Cooling Performance Using Airfoil Contouring," J. of Turbomachinery, **130**, in publication.

[44] Ligrani, P. M., Hedlund, C. R., 2004, " Experimental Surface Heat Transfer and Flow Structure in a Curved Channel with Laminar, Transitional and Turbulent Flows," J. of Turbomachinery, **126**, pp. 414-423.

[45] Bernsdorf, S., Rose, M. G., Abhari, R. S., 2006, "Modeling of Film Cooling – Part1: Experimental Study of Flow Structure," J. of Turbomachinery, **128**, pp. 141-149.

[46] Blair, M.F., 1974, "An Experimental Study of Heat Transfer and Film Cooling on Large-Scale Turbine Endwalls," ASME J. of Heat Transfer, **96**, pp. 524-529.

[47] Harasgama, S.P., and Burton, C.D., 1992, "Film Cooling Research on the Endwall of a Turbine Nozzle Guide Vane in a Short Duration Annular Cascade: Part 1 – Experimental Technique and Results," ASME J. of Turbomachinery, **114**, pp.734-740.

[48] Friedrichs, S., Hodson, H.P., Dawes, W.N., 1996, "Distribution of Film-Cooling Effectiveness on a Turbine Endwall Measured Using Ammonia and Diazo Technique," ASME J. of Turbomachinery, **118**, pp.613-621.

[49] Friedrichs, S., Hodson, H.P., Dawes, W.N., 1997, "Aerodynamic Aspects of Endwall Film-Cooling," ASME J. of Turbomachinery, **119**, pp.786-793.

[50] Chyu, M.K., 2001, "Heat Transfer near Turbine Nozzle Endwall," Annals of the New York Academy of Sciences, **934**, pp. 27-36.

[51] Zhang, L.J., and Jaiswal, R.S., 2001, "Turbine Nozzle Endwall Film Cooling Study Using Pressure Sensitive Paint," ASME J. of Turbomachinery, **123**, pp.730-738.

[52] Kost, F., and Nicklas, M., 2001, "Film-Cooled Turbine Endwall in a Transonic Flow Field: Part 1 – Aerodynamic Measurements," ASME J. of Turbomachinery, **123**, pp.709-719.

[53] Nicklas, M., 2001, "Film-Cooled Turbine Endwall in a Transonic Flow Field: Part 2 – Heat Transfer and Film-Cooling Effectiveness," ASME J. of Turbomachinery, **123**, pp.720-728.

[54] Kost, F., and Mullaert, A., May 8-11, 2006, "Migration of Film-Coolant from Slot and Hole Ejection at a Turbine Vane Endwall," ASME Paper No. GT2006-90355.

[55] Oke, R.A., Simon, T.W., Burd, S.W., and Wahlberg, R., 2000, "Measurements in a Turbine Cascade over a Contoured Endwall: Discrete Hole Injection of Bleed Flow," ASME Paper No. 2000-GT-214.

[56] Oke, R.A., Simon, T.W., Shih, T., Zhu, B., Ling, Y.L., Chyu, M., 2001, "Measurements Over a Film-Cooled Contoured Endwall with Various Injection Rates," ASME Paper No. 2001-GT-140.

[57] Oke, R.A., and Simon, T.W., 2002, "Film Cooling Experiments with Flow Introduced Upstream of a First Stage Nozzle Guide Vane Through Slots of Various Geometries," ASME Paper No. GT-2002-30169.

[58] Knost, D.G., and Thole, K.A., 2004, "Adiabatic Effectiveness Measurements of Endwall Film-Cooling for a First Stage Vane," J. of Turbomachinery, **127**, pp. 297-305.

[59] Zhang, L., and Moon, H.K., 2003, "Turbine Nozzle Endwall Inlet Film Cooling – The Effect of a Back-Facing Step," ASME Paper No. GT-2003-38319.

[60] Piggush, J.D., and Simon, T.W., 2005, "Flow Measurements in a First Stage Nozzle Cascade Having Endwall Contouring, Leakage and Assembly Features," ASME Paper No. GT-2005-68340.

[61] Cardwell, N.D., Sundaram, N., and Thole, K.A., 2005, "Effects of Mid-Passage Gap, Endwall Misalignment and Roughness on Endwall Film-Cooling," ASME Paper No. GT-2005-68900.

[62] Hada, S. and Thole, K. A., "Computational Study of a Mid Passage Gap and Upstream Slot on Vane Endwall Film Cooling," ASME Paper No. GT-2006-91067.

[63] Barigozzi, G., Franchini, G., and Perdichizzi, A., 2006, "Endwall Film Cooling through Fan-Shaped Holes with Different Area Ratios," ASME Paper No. GT-2006-90684.

[64] Nasir, H., Acharya, S., Ekkad, S., 2003, "Improved Film Cooling form Cylindrical Angled Holes with Triangular Tabs: Effect of Tab Orientations," Int. J. of Heat and Fluid Flow, **24**, pp. 657-668.

[65] Yuen, C. H. N., Martinez-Botas, R. F., 2003, "Film Cooling Characteristics of Rows of Round Holes at Various Streamwise Angles in a Crossflow: PartII. Heat Transfer Coefficients," Int. J. of Heat and Mass Transfer, **48**, pp. 5017-5035.

[66] Rozati, A., Tafti, D. K., 2007, "Large Eddy Simulations of Leading Edge Film Cooling: Analysis of Flow Structures, Effectiveness, and Heat Transfer Coefficient," Int. J. of Heat and Fluid Flow, **29**, pp. 1-17.

[67] Guo, S. M., Lai, C. C., Oldfield, M. L. G., Lock, G. D., Rawlinson, A. J., 1998, " The Application of Thin-Film Technology to Measure Turbine-Vane Heat Transfer and Effectiveness in a Film-Cooled , Engine-Simulated Environment," Int. J. of Heat and Fluid Flow, **19**, pp. 594-600.

[68] Garg, V. K., Abhari, R. S., 1997, "Comparison of Predicted and Experimental Nusselt Number for a Film Cooled Rotating Blade," Int. J. of Heat and Fluid Flow, **18**, pp. 452-460.

[69] Papa, M., Goldstein, R. J., Gori, F., 2007, "Numerical Heat Transfer Predictions and Mass/Heat Transfer Measurements in a Linear Turbine Cascade," Applied Thermal Engineering, **27**, pp. 771-778.

[70] Wright, L.M., Gao, Z., Varvel, T.A., and Han, J.C., 2005, "Assessment of Steady State PSP, TSP and IR Measurement Techniques for Flat Plate Film Cooling," ASME Paper No. HT-2005-72363.

[71] Gao, Z., Wright, L.M., and Han, J.C., 2005, "Assessment of Steady State PSP and Transient IR Measurement Techniques for Leading Edge Film Cooling," ASME Paper No. IMECE-2005-80146.

[72] Wright, L. M., Gao, Z., Yang, H. and Han, J. C., 2006, "Film Cooling Effectiveness Distribution on a Gas Turbine Blade Platform with Inclined Slot Leakage and Discrete Hole Flows," ASME Paper No. GT-2006-90375.

[73] Ahn, J., Mhetras, S.P., and Han, J.C., 2004, "Film-Cooling Effectiveness on a Gas Turbine Blade Tip," ASME Paper No. GT-2004-53249.

[74] Mhetras, S.M., Yang, H., Gao, Z., and Han, J.C., 2005, "Film Cooling Effectiveness on Squealer Rim Walls and Squealer Cavity Floor of a Gas Turbine Blade Tip Using Pressure Sensitive Paint," ASME Paper No. GT-2005-68387.

[75] Saumweber, C., Schulz, A., 2004, "Interaction of Film Cooling Rows: Effects of Hole Geometry and Row Spacing on the Cooling Performance Downstream of the Second Row of Holes," J. of Turbomachinery, **126**, pp. 237-246.

[76] Bons, J. P., McClain, S. T., 2004, "The Effect of Real Turbine Roughness with Pressure Gradient on Heat Transfer," J. of Turbomachinery, **126**, pp. 385-394.

[77] Rutledge, J. L., Robertson, D., Bogard, D. G., 2006,"Degradation of Film Cooling Performance on a Turbine Vane Suction Side due to Surface Roughness," J. of Turbomachinery, **126**, pp. 547-554.

[78] Dring, R. P., Blair, M. F., and Hoslyn, H. D., 1980, "An Experimental Investigation of Film Cooling on a Turbine Rotor Blade," ASME J. of Engineering for Power, **102**, pp. 81-87.

[79] Takeishi, M., Aoki, S., Sato, T., and Tsukagoshi, K., 1992, "Film Cooling on a Gas Turbine Rotor Blade," ASME J. of Turbomachinery, **114**, pp. 828-834.

[80] Abhari, R.S., and Epstein, A.H., 1994, "An Experimental Study of Film Cooling in a Rotating Transonic Turbine," ASME J. of Turbomachinery, **116**, pp. 63-70.

[81] Garg, V. K., 1998, "Heat Transfer on a Film-Cooled Rotating Blade using different Turbulence Models," Int. J. of Heat and Mass Transfer, **42**, pp. 789-802.

[82] Haldeman, C. W., Dunn, M. G., 2004, "Heat-Transfer Measurements and Predictions for the Vane and Blade of a Rotating High-Pressure Turbine Stage," J. of Turbomachinery, **126**, pp. 101-109.

[83] Ahn, J., Schobeiri, M.T., Han, J.C., and Moon, H.K., 2004, "Film Cooling Effectiveness on the Leading Edge of a Rotating Turbine Blade," ASME Paper No. IMECE 2004-59852.

[84] Ahn, J., Schobeiri, M.T., Han, J.C., and Moon, H.K., 2005, "Film cooling effectiveness on the leading edge of a rotating Film-Cooled Blade Using Pressure Sensitive Paint," ASME Paper No. GT-2005-68344.

[85] Fu, W. L., Wright, L. M., Han, J. C., 2005. "Heat Transfer in Two Pass Rotating Rectangular Channels (AR=1:2 and AR=1:4) with 45º Angled Rib Turbulators," J. of Turbomachinery, **126**, pp. 164-174.

[86] Liou, T. M., Dai, G. Y., "Pressure and Flow Characteristics in a Rotating Two-Pass Square Duct with 45° Angled Ribs," J. of Turbomachinery, **126**, pp. 212-219.

[87] Lacovides, H., Kounadis, D., Launder, B. E., 2005, " Experimental Study of the Flow and Thermal Development of a Row of Cooling Jets Impinging on a Rotating Concave Surface," J. of Turbomachinery, **127**, pp. 222-229.

[88] Wright, L. M., Fu, W. L., Han, J. C., 2004, "Thermal Performance of Angled, V-Shaped and W-Shaped Rib Turbulators in Rotating Rectangular Cooling Channels (AR=4:1)," J. of Turbomachinery, **126**, pp. 604-614.

[89] Acharya, S., Zhou, F., Mahmood, G., Bunker, R. S., 2005, "Latticework (Vortex) Cooling Effectiveness: Rotating Channel Experiments," J. of Turbomachinery, **127**, pp. 471-410.

[90] Sleiti, A. K., Kapat, J. S., 2005, "Fluid Flow and Heat Transfer in Rotating Curved Duct at High Rotation and Density Ratios," J. of Turbomachinery, **127**, pp. 659-667.

[91] Blair, M.F., 1994, "An Experimental Study of Heat Transfer in a Large-Scale Turbine Rotor Passage," ASME J. of Turbomachinery, **116**, pp. 1-13.

[92] Karabay, H., Wilson, M., Owen, J. M., 2000, "Predictions of Effect of Swirl on Flow and Heat Transfer in a Rotating Cavity," Int. J. Heat and Fluid Flow, **22**, pp. 143-155.

[93] Sharef Aly Kadry Abdel-Fattah, 2003, "Blade Tip Clearance Effect on the Performance and Flow Field of a Three Stage Axial Turbine," Master's Thesis, Texas A&M University, College Station, TX.

[94] Schobeiri, M. T., 1989, "Optimum Trailing Edge Ejection for Cooled Gas Turbine Blades," ASME J. of Turbomachinery, **111**, (4), pp.510-514.

[95] Schobeiri, M. T., Pappu, K. R., 1999, "Optimization of Trailing Edge Ejection Mixing Losses Downstream of Cooled Turbine Blades: A Theoretical and Experimental Study," ASME J. of Fluids Engineering, **121**, pp. 118-125.

[96] Morrison, G. L., Schobeiri, M. T., Pappu, K. R., 1998, "Five-Hole Pressure Probe Analysis Technique," Flow Measurement and Instrumentation, **9**, pp. 153-158.

[97] McLachlan, B., and Bell, J., 1995, "Pressure-Sensitive Paint in Aerodynamic Testing," Exp. Therm. Fluid Sci., **10**, pp. 470–485.

[98] Goldstein, R.J., 1971, "Film Cooling - Advances in Heat Transfer, 7, pp. 321-379, Academic Press.

[99] Suryanarayanan, A., Mhetras, S., Schobeiri, M. T. and Han, J. C., "Film Cooling Effectiveness on a Rotating Turbine Platform using Pressure Sensitive Paint Technique," ASME Paper No. GT-2006-90034.

[100] Yang, H., Chen, H.C., and Han, J.C., 2006, "Numerical Study of a Rotating Blade Platform with Film Cooling from Cavity Purge Flow in a 1-1/2 Turbine Stage," ASME Paper No. GT-2006-90322.

[101] Yang, H., Gao, Z., Chen, H.C., Han, J.C., and Schobeiri, M.T., 2007, "Prediction Film Cooling and Heat Transfer on a Rotating Blade Platform with Stator-Rotor Purge and Discrete Film-Hole Flows in a 1-1/2 Turbine Stage," ASME Paper No. GT-2007-27069.

[102] Kline, S.J. and McClintock, F.A., 1953, "Describing Uncertainties in Single-Sample Experiments," Mech. Engr., **75**, pp. 3-8.

[103] Holman, J. P., 2000, Experimental Methods for Engineers, McGraw Hill, New York.

[104] Coleman, H.W., and Steele, W.G., 1989, Experimentation and Uncertainty Analysis for Engineers, John Wiley & Sons, New York.

APPENDIX A

This appendix presents a detailed user's guide to operation of PSI-Pressure sensor system, Fluke temperature sensor system and turbine engine traversing system via the LabVIEW© interface and data acquisition system. All software described as found on the data acquisition computer that contains the National Instruments data acquisition board. This information is also provided in [93]. Any changes made since then with extra details have been added for better clarity.

PSI-Pressure System Guide:

Before the use of the pressure scanners for pressure acquisition the 8 individual scanners (7 gauge pressure sensors and 1 ambient pressure sensor) must be zeroed. The pressure scanner system is connected to the computer through the use of a local network system which assigns each scanner a separate internet protocol (IP) number. Each IP number is preset by the manufacturer and should not be changed. The IP address of each pressure scanner can be read off of the labels attached to them. To zero each scanner a program Setzero.exe found as an icon on the user desktop is run. Make sure all the required connections from the computer to the scanner port are made before the zeroing. A window pops up and clicking on the "Set Zero" button, zeros each scanner individually. This procedure should always be applied before running the main LabVIEW© acquisition system. Running the Setzero.exe program while the LabVIEW© acquisition software is run may cause a system crash. Additionally the zeroing program should not be run when the engine is running.

The pressure scanners after zeroing require an initialisation procedure which is automatically performed by the LabVIEW© data acquisition program. To activate the LabVIEW© program, click on the turbo.vi shortcut on the desktop of the data acquisition computer. Prior to activation of the LabVIEW© application, one must ensure that power to the traversing controllers, the Fluke temperature system and the PSI pressure system must be on. After the initial pop-up screen select the I/O Config option in the edit menu. A initialisation window is opened. To initialise the pressure sensor channels click on the 8 buttons

beside each scanner module on the right side of the screen, the initialisation assigns each channel its predetermined IP address. The red colour of the button implies that the scanners are online and ready to use while brown means offline. Make sure all the buttons are red while clicking the config pressure button. Additionally make sure that the pressure ratio is calculated using module number 2, transducer number 2 at the inlet and module number 6, transducer number 12 at the exit or the exact physical location on the machine as set by the operator.

Each of the pressure scanners have sixteen transducers connecting to different locations on the turbine. Identify each transducer connection physically on the turbine and name them correspondingly using the green button on the pressure module section shown in Figure A1. This will assist later in the data analysis stage where it is required to know which column in the data file corresponds to what location on the turbine. Note down the identity of each connection accurately.

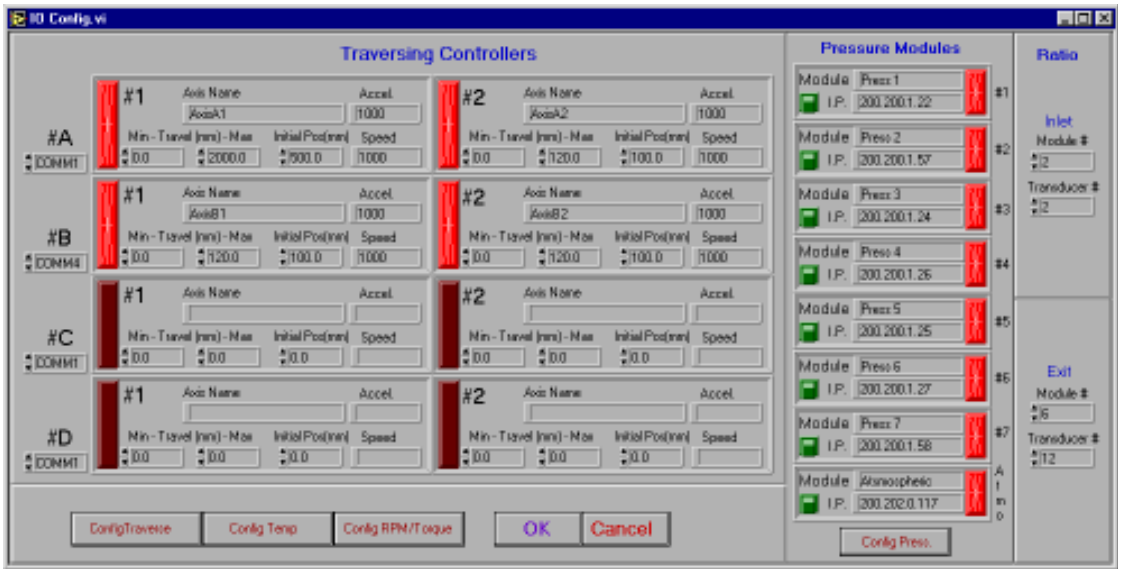

Figure A1: Shows the I/O config menu of the data acquisition program.

Figure A1 shows the I/O config menu, the IP addresses assigned to each pressure modules or sensors are shown in the table below:

Table A1: Pressure sensor IP addresses.

Scanner No.	IP Address
1	200.200.1.22
2	200.200.1.57
3	200.200.1.24
4	200.200.1.26
5	200.200.1.25
6	200.200.1.27
7	200.200.1.58
8	200.202.0.117

To ensure the operation of the pressure sensors after initialisation, press OK at the I/O Config window, and click on the “Auto Collect On” button, read outs from the pressure sensors will be shown in the main LabVIEW© window of turbo.vi. The pressure sensor system may also be accessed using software provided by the sensor manufacturer. The software is accessed by pressing the start menu button and is run by selecting the “NetScanner Start V1.04" shortcut. A window pops up, and to initialise the pressure scanners the “Init” and then “Netscanner Modules” option must be selected from the menu bar. When selected a secondary window props up which gives the option of typing in the IP addresses of each pressure sensor. All the IP addresses may be typed in at this point or a single IP address may also be typed in. After typing in the required IP addresses of the pressure sensors, press F1 or the “OK” button. The software can only display pressure read outs from the sixteen channels of one pressure sensor at a time, so if the user entered more then one sensor to move to the next sensor the “next module” option on the menu bar must be

selected. To begin acquiring or showing pressure data from the sixteen channels of one sensor, the keys Ctrl-D must be selected to begin displaying pressures.

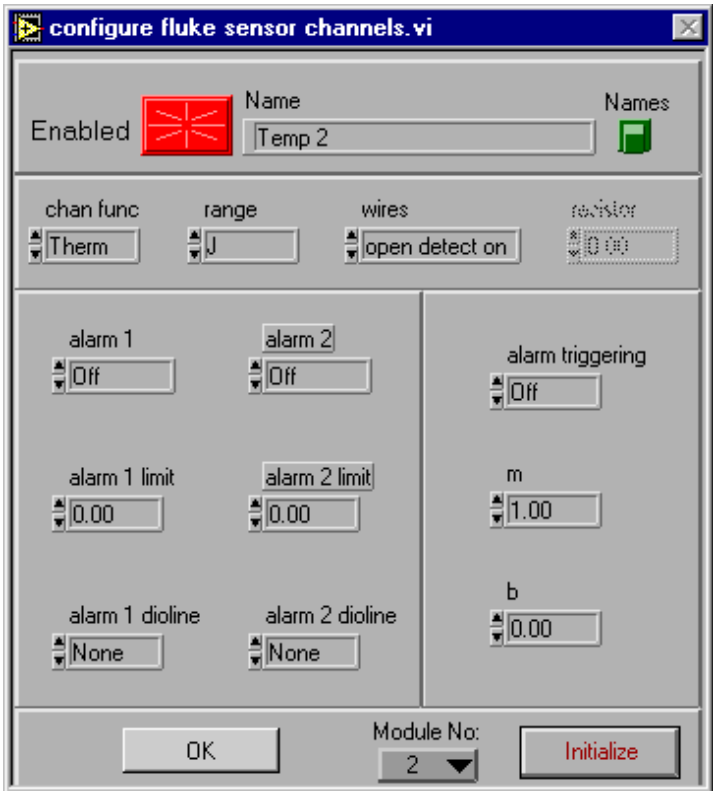

A2: Fluke Temperature Sensor System.

The Fluke sensor system is initialised in a similar manner to the pressure sensor system via the LabVIEW© interface. At the Config window shown in figure F1, click the "Config Temp" button, which produces the temperature configuration window. The Fluke temperature system uses two temperature modules each capable of acquiring 20 thermocouple channels. The temperature configuration window is

shown in figure A2. To initialize the Fluke system, make sure the module is set to number 2, and the enabled indicator is on, clicking on the “Initialize” button starts up both modules. A message window will pop up to inform of each unit’s initialisation status. If only one of the units are initialised, repeat the process again. It is worth noting that if the unit is left inactive for a considerable amount of time the temperature sensors will require initialisation again.

After the Fluke system is initialised, the temperature can be simultaneously scanned by clicking the “Auto Collect On” button from the main menu. Additionally the temperatures can be scanned manually from the read out at each Fluke temperature module; this is done by pressing the “MON” button and then clicking the up and down scanning arrows. If the thermocouples are not functioning or are disconnected, the Fluke module readout will produce an “OTC” or open thermocouple connection message. On the LabVIEW© display, a disconnected or malfunctioning thermocouple will produce a zero temperature.

The Fluke temperature system is set to recognising that all thermocouples used are J-type thermocouples, and therefore the voltages are automatically displayed as degrees centigrade. Calibrated thermocouple curves cannot be invoked into the data acquisition however they maybe included into the data analysis FORTRAN© program.

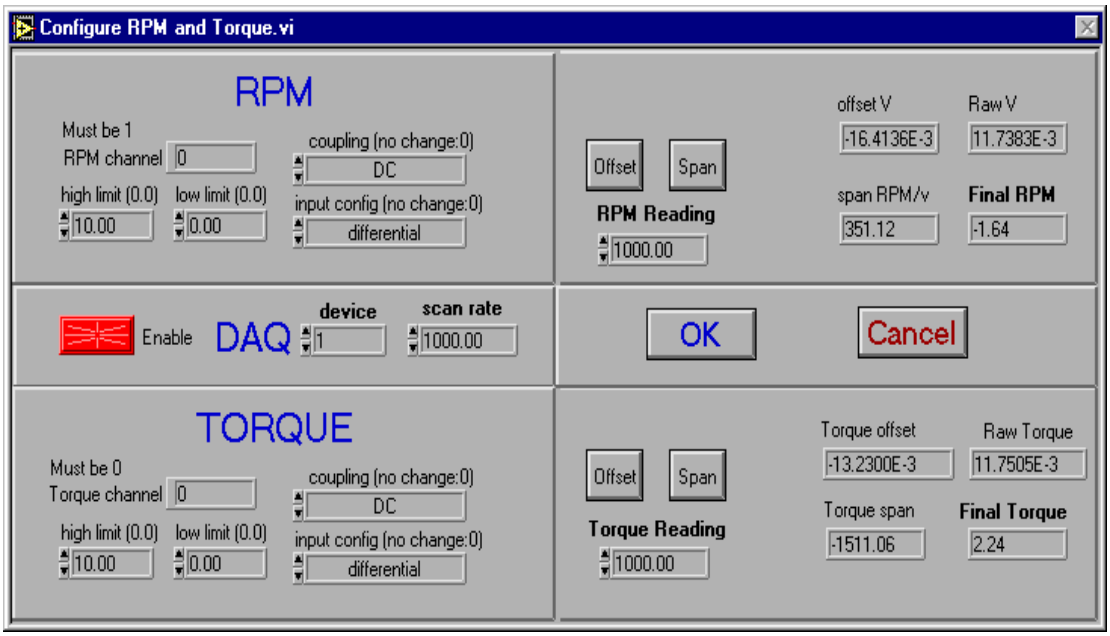

A3: Torque and Engine Frequency Acquisition.

The torque read out from the Himmelstein torquemeter and the engine speed readout from the Froude Consine dynamometer controller are both used to calibrate and initialise the readouts from the LabVIEW© data acquisition software. At the I/O Config window clicking the "Config RPM/Torque", produces the RPM and torque configuration window shown in figure A3. The "Offset" buttons for both RPM and torque are used to set the zero point, the "Span" buttons are used to set the slope of the calibration curve in RPM per volt or torque in lb.in per volt. Therefore the "Span" buttons should not be pressed when the torque and engine rpm are zero, but must be used when the engine is running at the required design point.

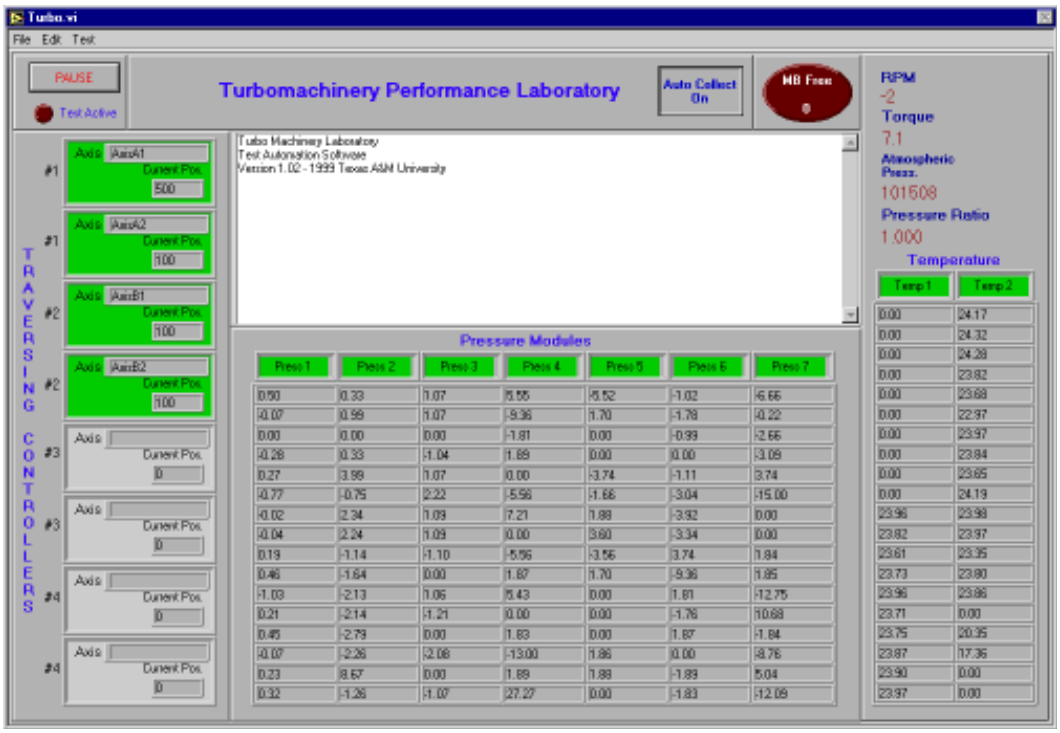

A4: Main window of LabVIEW© interface turbo.vi.

The traversing system controls four channels, three of which are used to control the three probe radial positions, and the fourth channel is used to control the circumferential position of all three probes. The position of each channel is displayed as a linear measurement in millimetres. The circumferential centre position is at a distance of 500 mm. The maximum circumferential positions are 350 mm, and 800 mm. For the radial channels, the hub position is at 100 mm, and the tip position is at 34 mm, which allows for a 66 mm radial displacement. Before initialisation of the traversing unit, the circumferential position should be set at the centre position (500 mm), and the three radial stations placed at the hub positions (100mm) as a default starting position. However the starting position may be set however the user wishes but the positions keyed into the LabVIEW© software must match the actual positions of the traversing channels. The initialisation is performed by enabling the channels A1, A2, B1, and B2 as shown in figure A1, making sure the positions keyed into the unit match the actual positions and then pressing the “Config

Traverse" button. The movement schedule for all the four traverses are dictated by the script file, which is a text file that specifies the movement for each channel, the number of data points to be collected and the time each channel is allowed for acquisition. The format of the script file is as follows:

<traversing device or channel>,<position>,<data points>,<waiting time in milliseconds>

The a,1 traverse device is the circumferential unit and the a,2 b,1 and b,2 channels are the radial traverses corresponding to stations 3, 4 and 5. The script files can be automatically generated using the "Genfile.exe" program available on the data acquisition computer desktop. An example of a script file is shown below: A line beginning with an asterisk (*) is a line which is ignored by the LabVIEW© software and that movement is not executed.

```
*Demonstration script file
a,1,350,0,0
b,1,100,10,2000
b,2,100,10,2000
a,2,100,10,2000
b,1,99,10,2000
b,2,99,10,2000
a,2,99,10,2000
b,1,98,10,2000
b,2,98,10,2000
a,2,98,10,2000
b,1,97,10,2000
b,2,97,10,2000
a,2,97,10,2000
……..
b,1,34,10,2000
b,2,34,10,2000
a,2,34,10,2000
a,1,360,0,0
b,1,34,10,2000
```

b,2,34,10,2000
a,2,34,10,2000
b,1,37,10,2000
b,2,37,10,2000
a,2,37,10,2000
...

A point taken includes all pressure channels, temperatures channels and traverse positions which are initialised and saved to the final data file. Note down the column numbers of the relevant data column by opening the data text file in excel.

F.5 Machine Startup Procedure:

1. Zero pressure transducers before start up (program SetZero.exe).
2. Check bearing oil level on the compressor (both sides).
3. Turn on outside switch for the compressor.
4. Open the garage door (use anchoring rope to secure the door).
5. Turn on water for dynamometer. Pressure gauge should read 20 psi.
6. Turn on in-cell dynamometer box. Make sure stop button is disabled.
7. Turn on inlet heater. Check heater is pre-set to zero degrees (green LCD is pre-set temperature and red LCD is actual temperature).
8. Check the dynamometer controller in the control room by pressing the green button.
9. Put the controller in constant rpm mode.
10. Set rpm demand to 600 rpm.
11. Set compressor out frequency at the compressor controller in the test cell between 30-35 Hz and press the start button.
12. The turbine starts running and the rpm should stabilise at 600 rpm.
13. Turn on the heater to an inlet temperature of 57ºC to produce a inlet temperature of 45 ºC to50ºC. Adjust the inlet temperature to produces a temperature that is just above 21ºC at the venturi inlet to avoid condensation.

14. Set the rpm demand at the dynamometer controller to the required rpm. The rotating speed will increase and the critical speed for the velocimeter on the torquemeter stand was observed to be around 2800rpm to 2900rpm. Please note that the rpm will slightly overshoot by about 50-100rpm before stabilizing in the next 20-30s.
15. Monitor venturi inlet temperature, make sure it does not go below 21ºC. Additionally monitor bearing temperatures, they should not go above 70ºC.
16. Monitor the velocimeters mounted on the bearing housing and torquemeter support. Stop the machine if the reading goes above 0.55in/s.
17. For film cooling and heat transfer measurements, in addition to the above, turn on the coolant supply loop provided at the rear of the turbine.
18. Once, the coolant is flowing as per the required flowrate, turn the coolant supply heater on and set the coolant temperature to be the same as the turbine inlet temperature using the PID controller.
19. Turn on the power supply to the rotor surface mounted heater such that the rotor surface temperature is roughly 10ºC to 20ºC greater than the inlet temperature for accurate TSP measurements. This step is not needed for the film cooling effectiveness measurement using PSP.
20. For film cooling and heat transfer experiments, turn on the camera, the probe light and the trigger which activates them both at the area of interest on the rotor.

Notes:

Make sure that everybody who is present in the testing area knows where the emergency compressor shutdown button is located (red button next to the office area entrance door). Do not leave control room while the turbine is running. Record the test in the Run Log. If Emergency shutdown is performed, make sure the inlet heater is switched off.

Machine Shutdown Procedure:

1. If you are running film cooling or heat transfer experiments, shut down the heaters related to the coolant loop first. This is very important as failure to do this will burn the heaters up.

2. Allow the coolant to flow through the turbine for a few minutes and then shut the coolant loop down.
3. Turn off the camera, probe light and the trigger.
4. Set the compressor demand at the compressor controller in the test area to 30 Hz. Note that the compressor has a slow deceleration rate and it takes a few minutes to reach 30 Hz.
5. When the compressor has reached 30Hz, set the heater temperature to 0 ºC.
6. Set the dynamometer demand to 600 rpm. This will ensure rapid passing of the critical speed.
7. Set the compressor demand to 0Hz and decrease the rotor speed completely.
8. Allow the turbine and compressor slow down. This will take a few minutes.
9. Wait for the turbine rpm to reach zero.
10. Turn off the compressor switch at the compressor controller in the test cell area.
11. Turn off the compressor power switch on the outside.
12. Check bearing oil level on the compressor (both sides).
13. Shut the garage door.
14. Turn off the inlet heater.
15. Turn off the in cell dynamometer box.
16. Turn off water supply to dynamometer.

APPENDIX B

The calibration facility used to calibrate the five hole pressure probes is shown in figure below Schobeiri et al. ([1] and [2]). A two axis fully automated traverse unit was used to move the probe -15º to +15º in pitch and yaw angles with one degree increments. At each point the five port pressures as well as total and static pressures were acquired through the use of a multi-channel pressure transducer system.

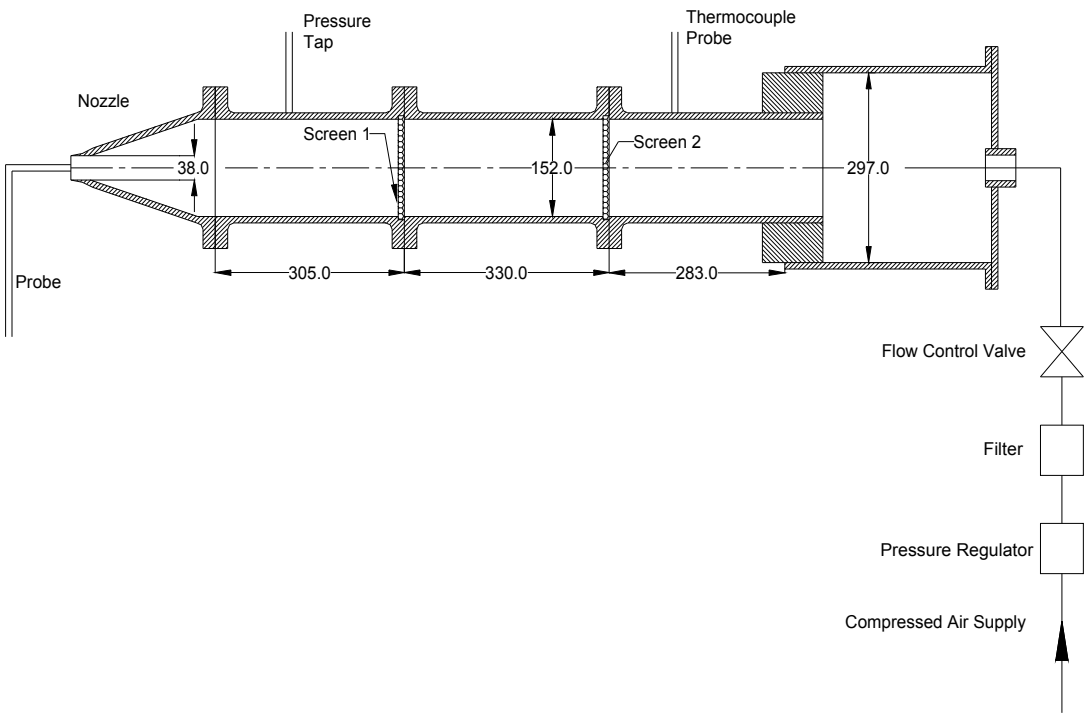

Figure B1: Schematic of calibration facility used to calibrate five hole pressure probes (dimensions in mm) Schobeiri et al. ([1] and [2]).

The following figures are the calibration curves obtained after plotting each 5-hole probe data as per Bohn's method. Calibration data acquisition is simple and a program called turboprobe is used after the initialization of the pressure scanners. The coefficients Q1 to Q5 are described in the main section as well as in Bohn's paper. The location of the calibration files and the corresponding names are also seen in the plots.

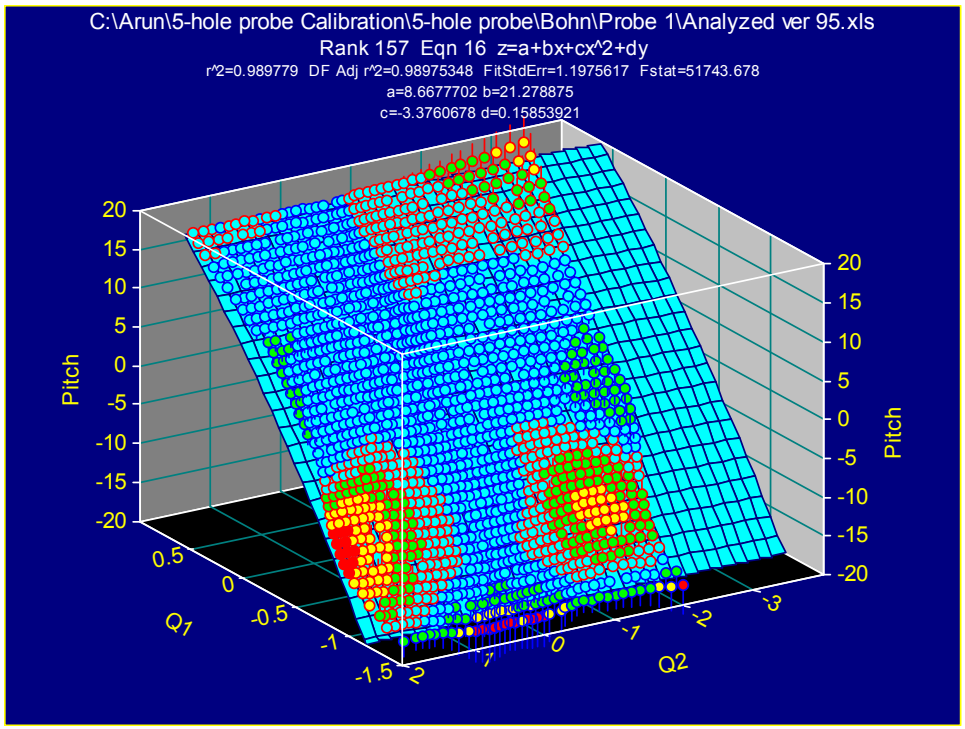
C:\Arun\5-hole probe Calibration\5-hole probe\Bohn\Probe 1\Analyzed ver 95.xls
Rank 157 Eqn 16 z=a+bx+cx^2+dy
r^2=0.989779 DF Adj r^2=0.98975348 FitStdErr=1.1975617 Fstat=51743.678
a=8.6677702 b=21.278875
c=-3.3760678 d=0.15853921
Pitch
Q1
Q2
Pitch

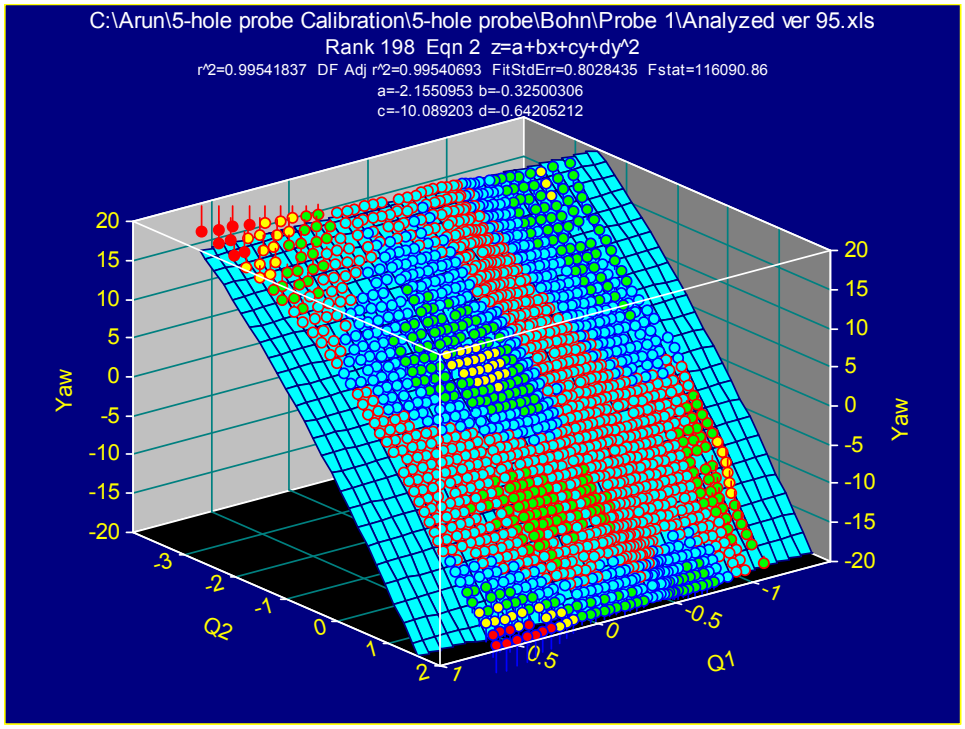
C:\Arun\5-hole probe Calibration\5-hole probe\Bohn\Probe 1\Analyzed ver 95.xls
Rank 198 Eqn 2 z=a+bx+cy+dy^2
r^2=0.99541837 DF Adj r^2=0.99540693 FitStdErr=0.8028435 Fstat=116090.86
a=-2.1550953 b=-0.32500306
c=-10.089203 d=-0.64205212
Yaw
Q2
Q1
Yaw

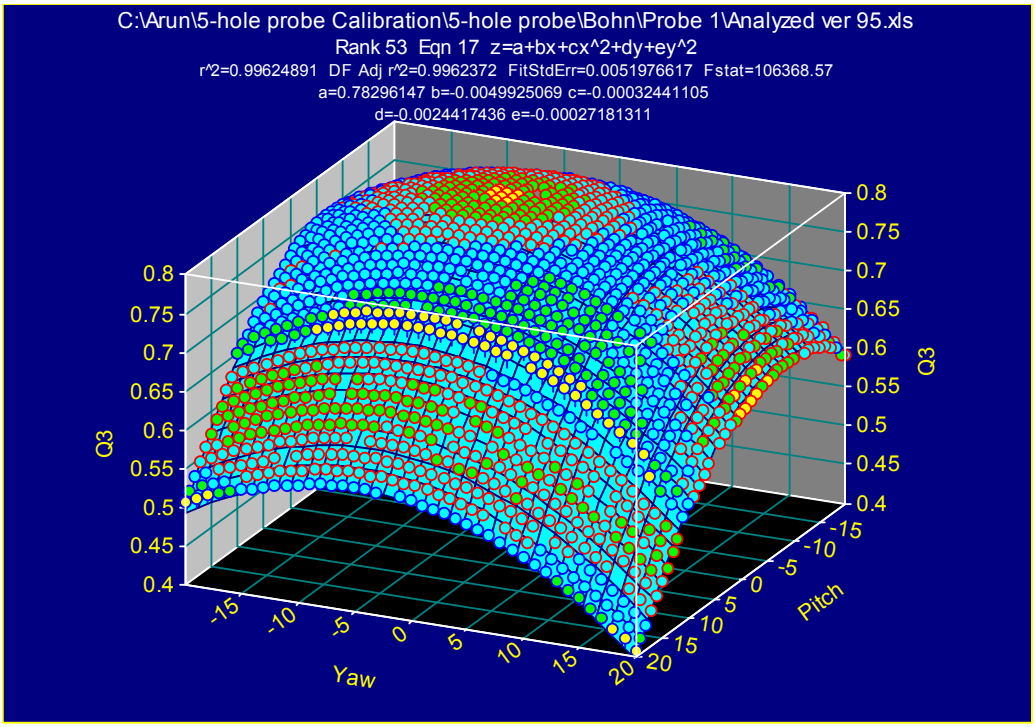
C:\Arun\5-hole probe Calibration\5-hole probe\Bohn\Probe 1\Analyzed ver 95.xls
Rank 53 Eqn 17 z=a+bx+cx^2+dy+ey^2
r^2=0.99624891 DF Adj r^2=0.9962372 FitStdErr=0.0051976617 Fstat=106368.57
a=0.78296147 b=-0.0049925069 c=-0.00032441105
d=-0.0024417436 e=-0.00027181311
Q3
Yaw
Pitch

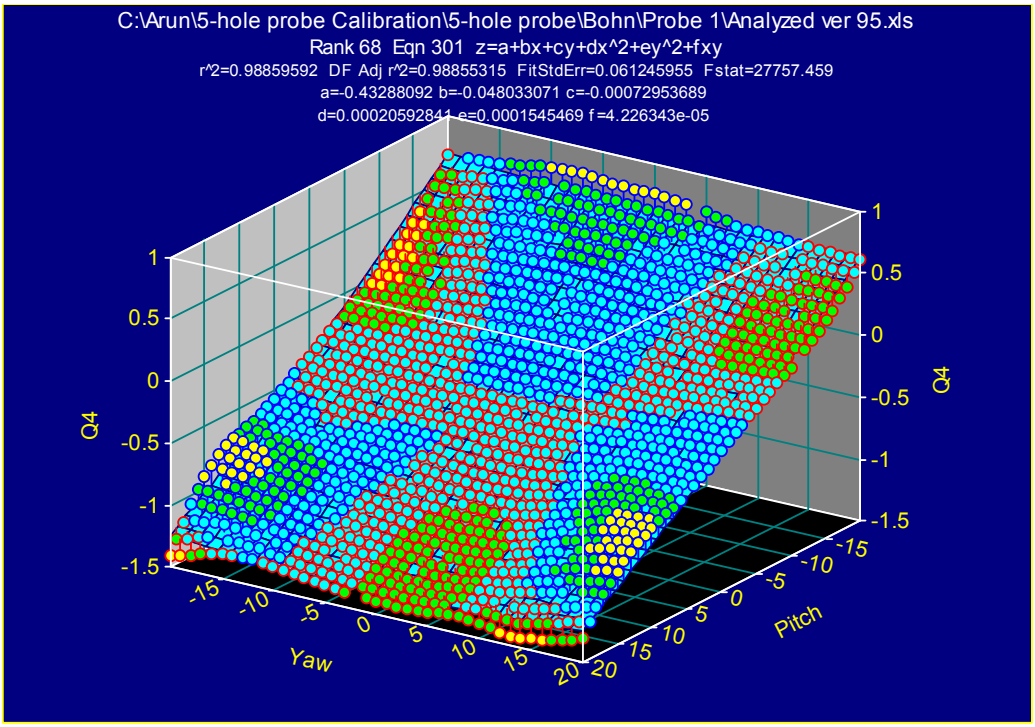
C:\Arun\5-hole probe Calibration\5-hole probe\Bohn\Probe 1\Analyzed ver 95.xls
Rank 68 Eqn 301 z=a+bx+cy+dx^2+ey^2+fxy
r^2=0.98859592 DF Adj r^2=0.98855315 FitStdErr=0.061245955 Fstat=27757.459
a=-0.43288092 b=-0.048033071 c=-0.00072953689
d=0.00020592841 e=0.0001545469 f=4.226343e-05
Q4
Yaw
Pitch

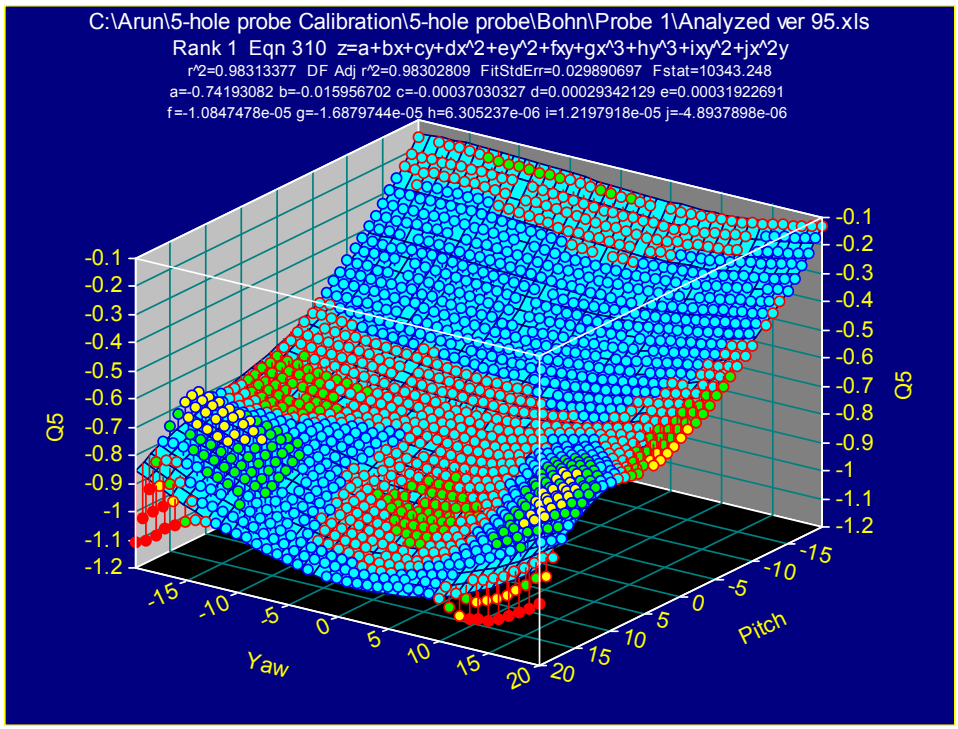
C:\Arun\5-hole probe Calibration\5-hole probe\Bohn\Probe 1\Analyzed ver 95.xls
Rank 1 Eqn 310 z=a+bx+cy+dx^2+ey^2+fxy+gx^3+hy^3+ixy^2+jx^2y
r^2=0.98313377 DF Adj r^2=0.98302809 FitStdErr=0.029890697 Fstat=10343.248
a=-0.74193082 b=-0.015956702 c=-0.00037030327 d=0.00029342129 e=0.00031922691
f=-1.0847478e-05 g=-1.6879744e-05 h=6.305237e-06 i=1.2197918e-05 j=-4.8937898e-06
Q5
Yaw
Pitch

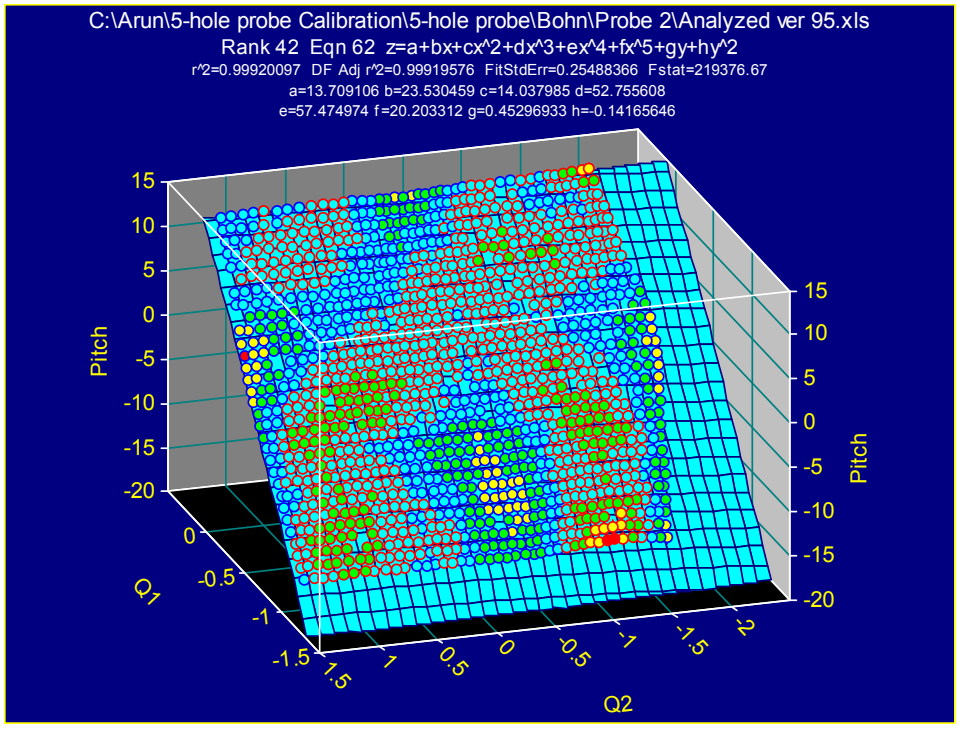
C:\Arun\5-hole probe Calibration\5-hole probe\Bohn\Probe 2\Analyzed ver 95.xls
Rank 42 Eqn 62 z=a+bx+cx^2+dx^3+ex^4+fx^5+gy+hy^2
r^2=0.99920097 DF Adj r^2=0.99919576 FitStdErr=0.25488366 Fstat=219376.67
a=13.709106 b=23.530459 c=14.037985 d=52.755608
e=57.474974 f=20.203312 g=0.45296933 h=-0.14165646
Pitch
Q1
Q2

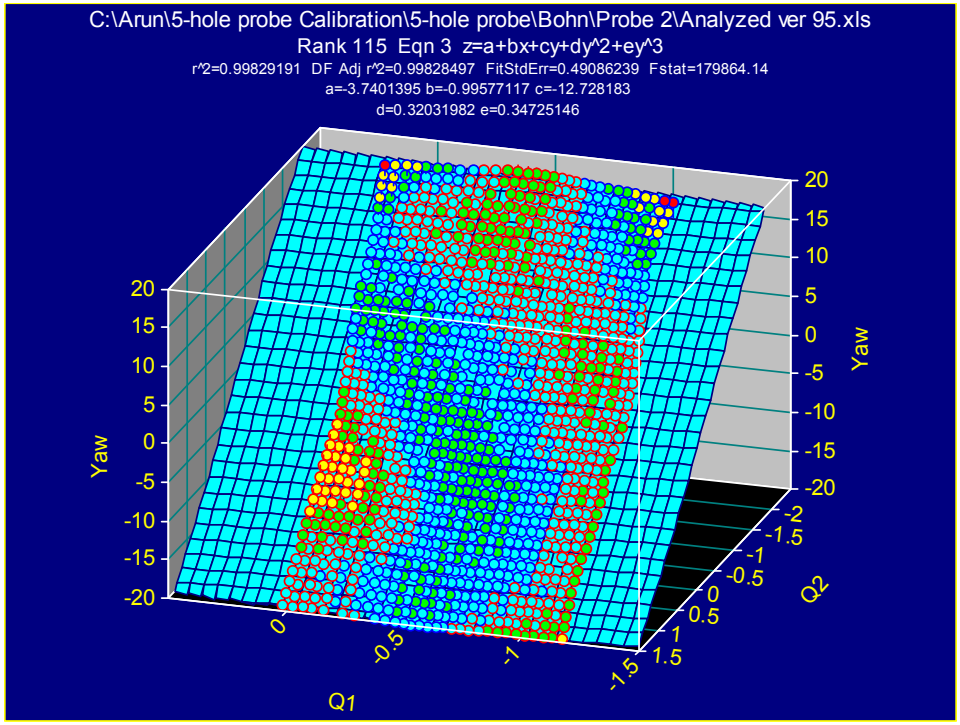
C:\Arun\5-hole probe Calibration\5-hole probe\Bohn\Probe 2\Analyzed ver 95.xls
Rank 115 Eqn 3 z=a+bx+cy+dy^2+ey^3
r^2=0.99829191 DF Adj r^2=0.99828497 FitStdErr=0.49086239 Fstat=179864.14
a=-3.7401395 b=-0.99577117 c=-12.728183
d=0.32031982 e=0.34725146
Yaw
Q1
Q2

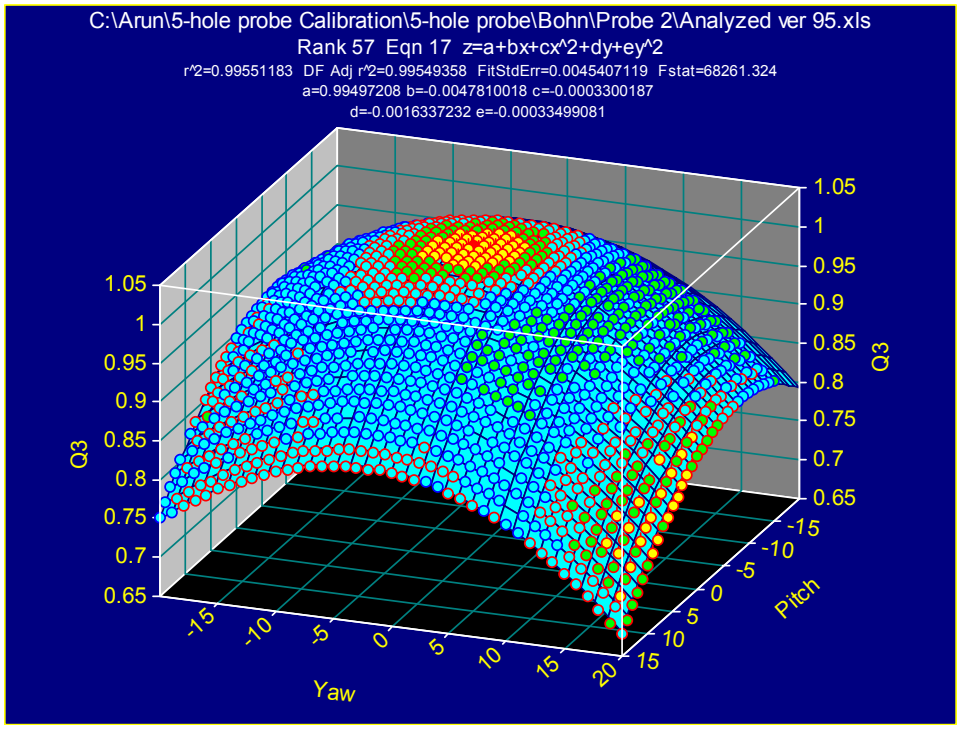
C:\Arun\5-hole probe Calibration\5-hole probe\Bohn\Probe 2\Analyzed ver 95.xls
Rank 57 Eqn 17 z=a+bx+cx^2+dy+ey^2
r^2=0.99551183 DF Adj r^2=0.99549358 FitStdErr=0.0045407119 Fstat=68261.324
a=0.99497208 b=-0.0047810018 c=-0.0003300187
d=-0.0016337232 e=-0.00033499081
Q3
Yaw
Pitch

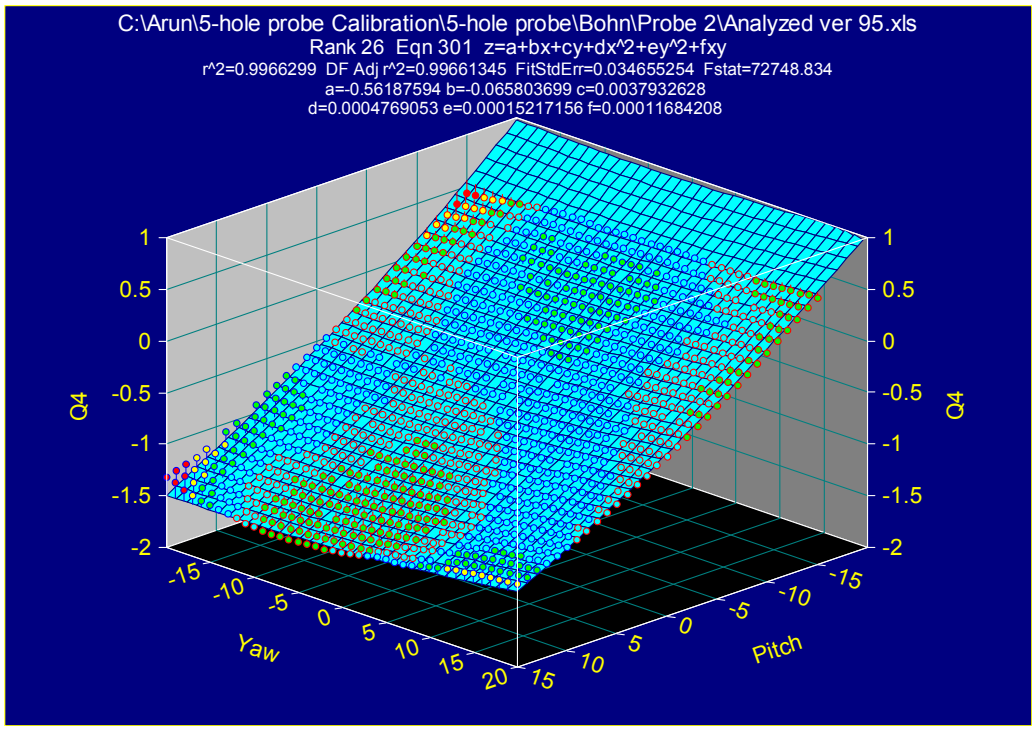
C:\Arun\5-hole probe Calibration\5-hole probe\Bohn\Probe 2\Analyzed ver 95.xls
Rank 26 Eqn 301 z=a+bx+cy+dx^2+ey^2+fxy
r^2=0.9966299 DF Adj r^2=0.99661345 FitStdErr=0.034655254 Fstat=72748.834
a=-0.56187594 b=-0.065803699 c=0.0037932628
d=0.0004769053 e=0.00015217156 f=0.00011684208
Q4
Yaw
Pitch

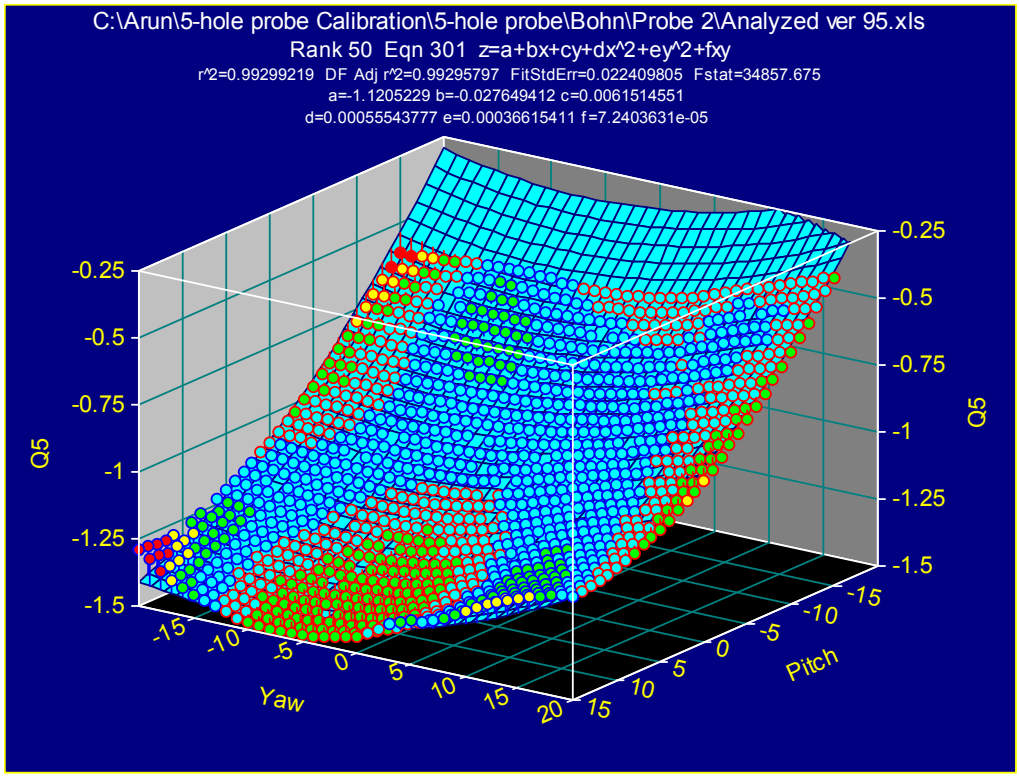
C:\Arun\5-hole probe Calibration\5-hole probe\Bohn\Probe 2\Analyzed ver 95.xls
Rank 50 Eqn 301 z=a+bx+cy+dx^2+ey^2+fxy
r^2=0.99299219 DF Adj r^2=0.99295797 FitStdErr=0.022409805 Fstat=34857.675
a=-1.1205229 b=-0.027649412 c=0.0061514551
d=0.00055543777 e=0.00036615411 f=7.2403631e-05
Q5
Yaw
Pitch

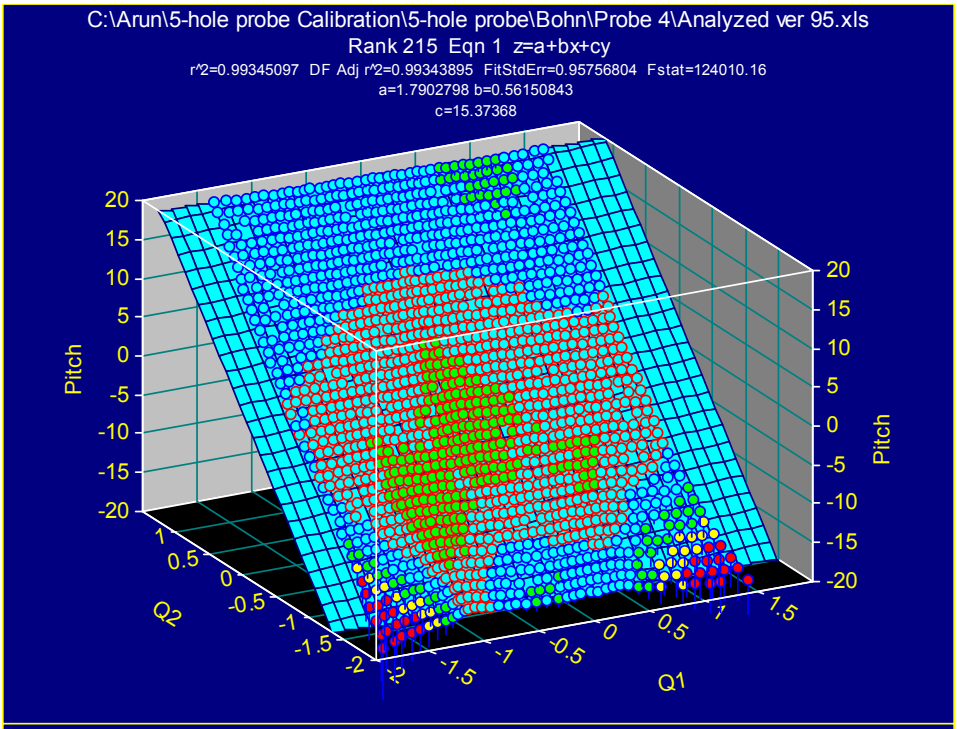
C:\Arun\5-hole probe Calibration\5-hole probe\Bohn\Probe 4\Analyzed ver 95.xls
Rank 215 Eqn 1 z=a+bx+cy
r^2=0.99345097 DF Adj r^2=0.99343895 FitStdErr=0.95756804 Fstat=124010.16
a=1.7902798 b=0.56150843
c=15.37368
Pitch
Pitch
Q2
Q1

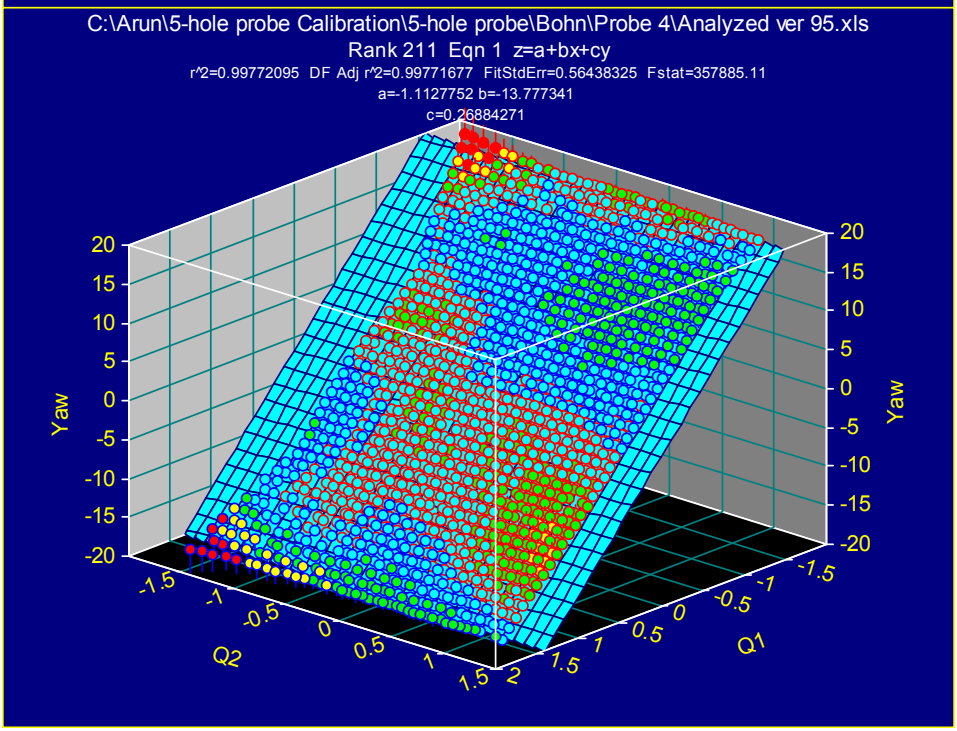
C:\Arun\5-hole probe Calibration\5-hole probe\Bohn\Probe 4\Analyzed ver 95.xls
Rank 211 Eqn 1 z=a+bx+cy
r^2=0.99772095 DF Adj r^2=0.99771677 FitStdErr=0.56438325 Fstat=357885.11
a=-1.1127752 b=-13.777341
c=0.26884271
Yaw
Yaw
Q2
Q1

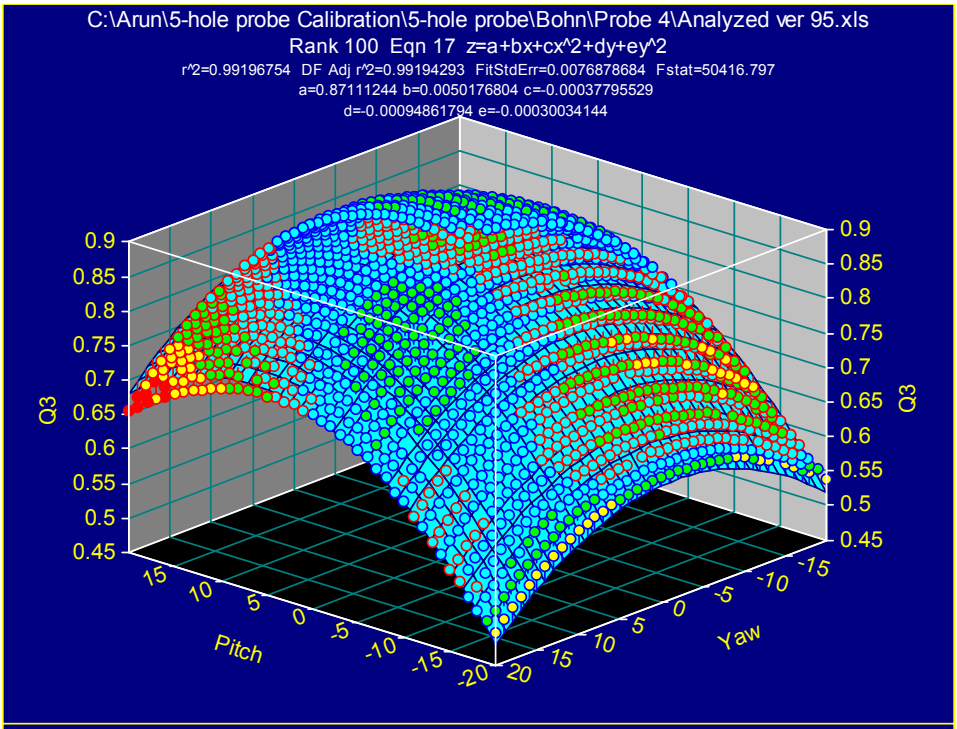
C:\Arun\5-hole probe Calibration\5-hole probe\Bohn\Probe 4\Analyzed ver 95.xls
Rank 100 Eqn 17 z=a+bx+cx^2+dy+ey^2
r^2=0.99196754 DF Adj r^2=0.99194293 FitStdErr=0.0076878684 Fstat=50416.797
a=0.87111244 b=0.0050176804 c=-0.00037795529
d=-0.00094861794 e=-0.00030034144
Q3
Pitch
Yaw

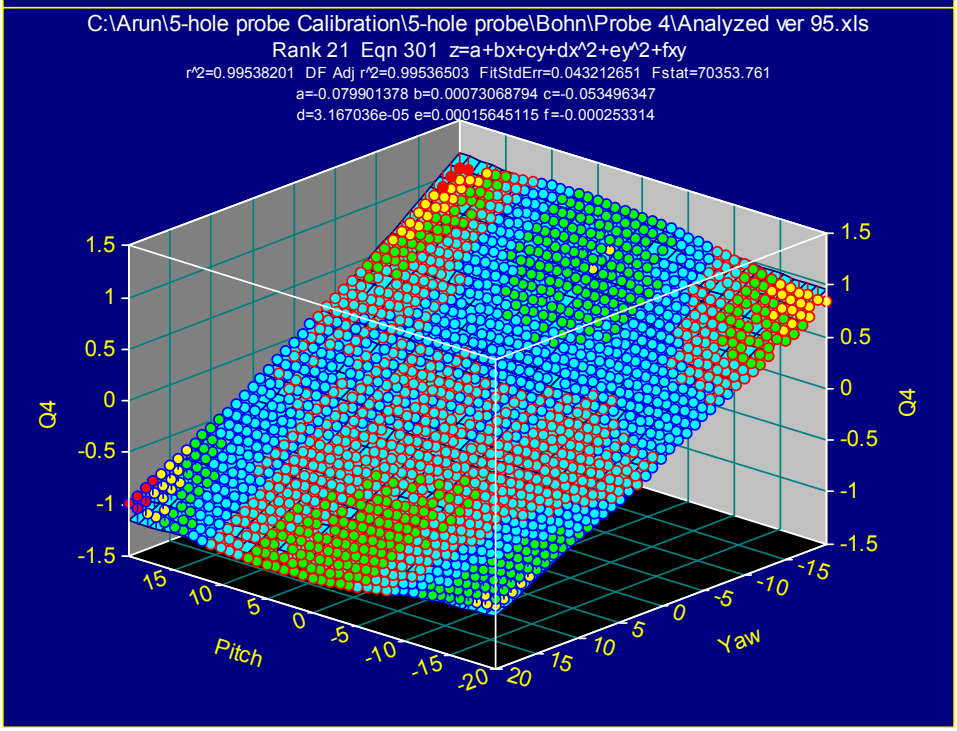
C:\Arun\5-hole probe Calibration\5-hole probe\Bohn\Probe 4\Analyzed ver 95.xls
Rank 21 Eqn 301 z=a+bx+cy+dx^2+ey^2+fxy
r^2=0.99538201 DF Adj r^2=0.99536503 FitStdErr=0.043212651 Fstat=70353.761
a=-0.079901378 b=0.00073068794 c=-0.053496347
d=3.167036e-05 e=0.00015645115 f=-0.000253314
Q4
Pitch
Yaw

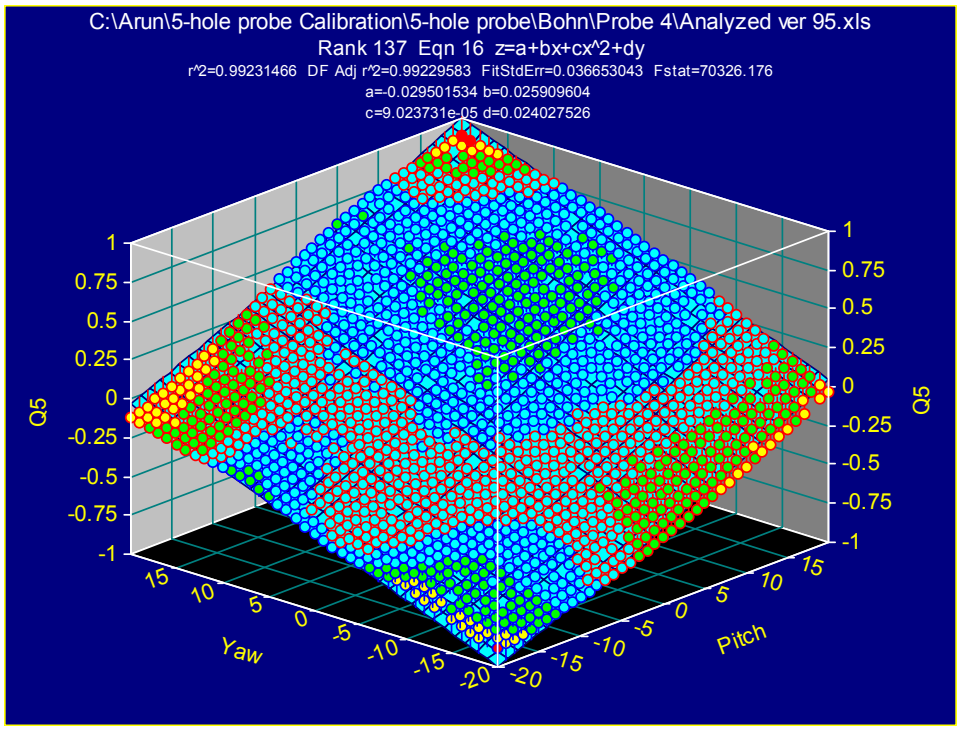

The following spreadsheet is a sample of a typical calibration sheet with the angle , 5 pressures from the 5-hole Pitot probe, the total and the static pressures from the calibration facility. Columns Q1 to Q5 are the coefficients calculated as described earlier based on Bohn's. Also in all the graphs above, x-axis corresponds to pitch and y-axis to yaw.

	Pitch	Yaw	P1	P2	P3	P4	P5	Ptot	Psta	Pm-Psta	Pt-Psta	Q1	Q2	Q3	Q4
1	-20	-20	4470.753	4036.389	-1318.222	-3399.369	3362.881	6470.43	-302.361	4773.114	6772.791	1.557842	-0.980723	0.704748	0.85474
2	-20	-18	4568.71	3753.303	-1281.919	-2939.207	3456.133	6469.328	-301.03	4869.74	6770.358	1.374305	-0.972958	0.719274	0.864154
3	-20	-17	4610.624	3590.775	-1282.385	-2675.351	3496.656	6465.712	-306.529	4917.153	6772.241	1.27434	-0.971912	0.726075	0.870171
4	-20	-16	4645.181	3426.13	-1301.425	-2408.365	3529.381	6459.761	-305.287	4950.468	6765.048	1.178574	-0.975828	0.731771	0.879019
5	-20	-15	4676.986	3267.338	-1314.943	-2160.96	3549.096	6458.591	-304.733	4981.719	6763.324	1.089644	-0.976378	0.736578	0.885944
6	-20	-14	4706.165	3082.885	-1368.296	-1895.729	3554.029	6463.022	-308.192	5014.357	6771.214	0.992872	-0.981646	0.74054	0.897101
7	-20	-13	4735.713	2889.344	-1447.223	-1631.183	3554.071	6467.676	-308.258	5043.971	6775.934	0.896224	-0.991539	0.744395	0.912485
8	-20	-12	4747.012	2693.912	-1537.843	-1387.236	3555.364	6455.088	-306.373	5053.385	6761.461	0.807607	-1.00788	0.747381	0.929511
9	-20	-11	4765.777	2481.866	-1646.412	-1137.983	3554.073	6458.262	-308.103	5073.88	6766.365	0.713428	-1.024952	0.749868	0.947656
10	-20	-10	4783.08	2260.9	-1719.128	-900.524	3553.512	6457.161	-305.909	5088.989	6763.07	0.621228	-1.036088	0.752467	0.961428
11	-20	-9	4793.862	2049.878	-1747.383	-687.398	3559.328	6455.46	-307.394	5101.256	6762.854	0.536589	-1.040275	0.754305	0.967231
12	-20	-8	4802.298	1829.016	-1772.995	-461.437	3559.307	6454.56	-308.569	5110.867	6763.129	0.448154	-1.043326	0.755696	0.972226
13	-20	-7	4808.755	1606.854	-1753.432	-238.65	3556.097	6453.654	-308.79	5117.545	6762.444	0.360623	-1.037515	0.75676	0.970387
14	-20	-6	4812.544	1393.858	-1723.357	-27.399	3551.616	6451.539	-309.19	5121.734	6760.729	0.277495	-1.029919	0.757571	0.966745
15	-20	-5	4815.922	1175.142	-1694.424	185.725	3546.014	6452.089	-310.897	5126.819	6762.986	0.192988	-1.022162	0.75807	0.962644
16	-20	-4	4820.354	959.368	-1664.898	399.73	3529.081	6455.044	-310.719	5131.073	6765.763	0.109068	-1.01226	0.758388	0.95854
17	-20	-3	4814.674	771.926	-1668.113	593.479	3515.291	6451.275	-308.347	5123.021	6759.622	0.034832	-1.011787	0.757886	0.959046
18	-20	-2	4814.588	571.793	-1651.552	802.33	3481.684	6460.422	-310.231	5124.819	6770.653	-0.044984	-1.001642	0.756917	0.955025
19	-20	-1	4804.752	388.707	-1665.491	1007.114	3460.313	6460.071	-310.963	5115.715	6771.034	-0.120884	-1.001972	0.755529	0.955577

APPENDIX C

The following section deals with the data acquisition procedure for PSP and TSP system using a software called Camware© available on the desktop of the PSP and TSP data acquisition computer. A series of pictures showing the sequence from starting the program to data acquisition is given below. This is common for PSP and TSP data and calibration measurements.

Figure C1: Snapshot of the data acquisition computer's desktop.

1. Click on the icon which says Camware© to start the program which interfaces the camera with the computer and enables acquisition of picture data.
2. This will open a window as shown in C2. The software allocates system memory for the camera to operate. Allow a few minutes for the camera and the system to stabilize.
3. Once the software is up, click on the options on the screen and familiarize yourself with them as they help you monitor the data during acquisition.

4. Before taking any data, click on the option shown in C3 and set the number of images you want to acquire.
5. Once this is done, the software is ready to acquire data and the image acquisition can be enabled by clicking the option shown in C4.
6. Care must be taken to acquire data when there is minimum light in the test room, preferably a dark environment. The camera will now acquire data every time the trigger activates data acquisition.
7. Save the data in tif format.

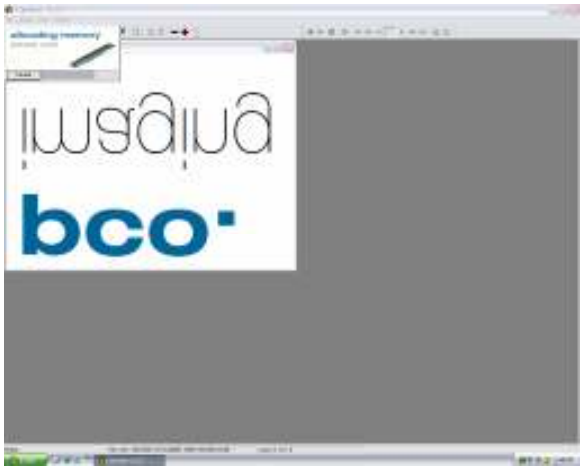

Figure C2: Window which pops up after clicking the camware icon.

Figure C3: This picture shows the option to set the number of images for data acquisition.

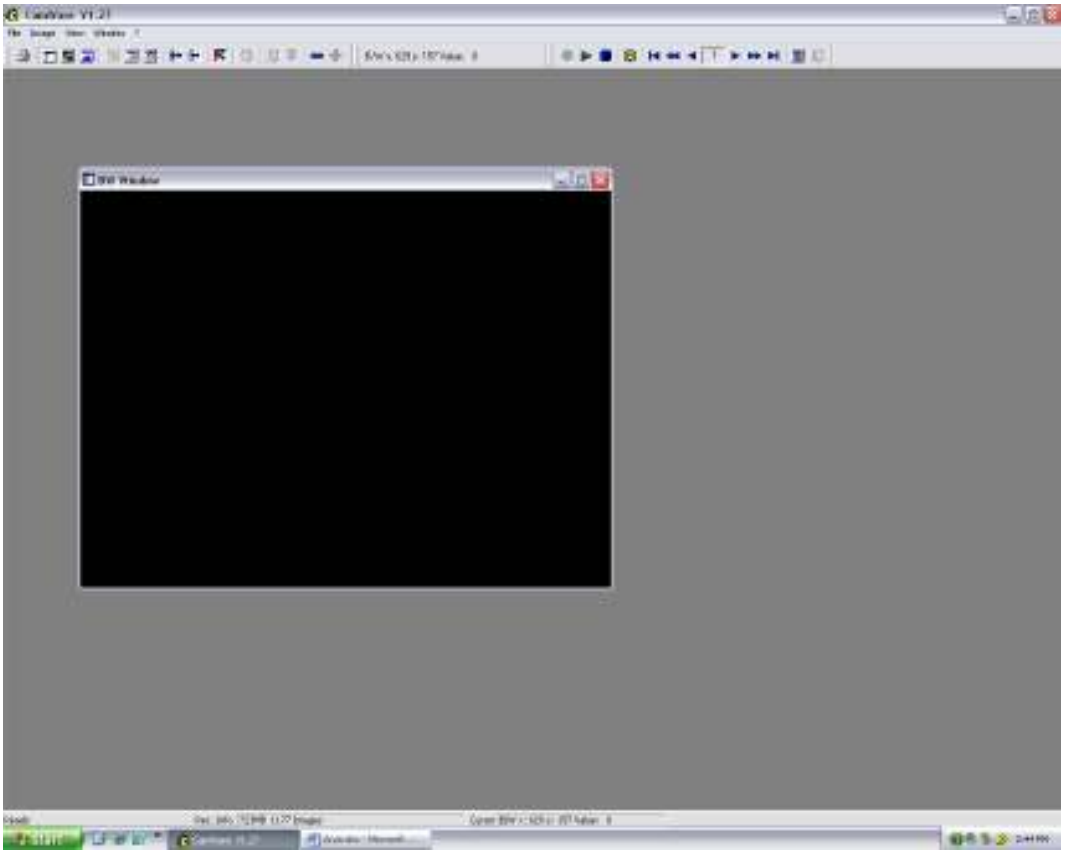

Figure C4: This picture shows the black and white window where the image can be seen during data acquisition.

To start data acquisition, click on the circular icon to the left of the green play button in the main window. Adjust the binning setting depending on the intensity observed on the acquired image. This can be done through the window which pop-ups when the penultimate icon from the right on the menu bar is clicked.

APPENDIX D

The following information provides details regarding the programs needed for analysing calibration data and experimental data for PSP measurements. It consists of one MATLAB® and three FORTRAN© programs. The MATLAB® program (cal.m) is used to convert the digital image taken by the camera to the corresponding intensity values. It is the same program used to analyze both calibration and experimental data files. The input for this file is the tif image acquired by the camera. This program will average all the data images acquired and provide a single text file as output. The only modification required in the program itself is the data file name and the image size in pixels depending on the binning setting on the camera. If the file is modified, a new executable file is created after compilation and the executable is copied into the data folder and run to obtain the processed output. The output is in the form a *.dat or any similar text file depending on how one wants it. The output file will contain the pixel number in x and y directions and pixel intensity along the z-axis. This program is also used to analyze the black and reference images acquired by the camera. For calibration, this file is further averaged using a simple MS-EXCEL spreadsheet to obtain one intensity value for every pressure setting in the calibration chamber and the ratio of calibration pressures and intensities are plotted as shown to obtain the calibration curve. Reference image is acquired at temperatures (~46°C) similar to that seen during actual experiments and P_{atm} is considered P_{ref}. Calibration is complete once the plotted pressure versus intensity curves are curve fitted and the corresponding equation is obtained.

- Once this is performed, the first of the FORTRAN© files called a1p.f or n1p.f is used for converting the intensities from the MATLAB® output to pressures after applying the calibration function.
- The inputs (3 files) for this program are the intensity data, *.dat files, either air or nitrogen data, the black and the reference files from the MATLAB® program. This FORTRAN© program is run separately for nitrogen data and oxygen data in the same folder containing all the data and input files.

- Output from this file will be a single file with pressure distribution due to either air injection or nitrogen injection, whichever case it was run for.
- A pixel shift program can be used to make the image acquired during actual tests correspond with the reference image acquired immediately after the rotor is stopped.
- The second FORTRAN© called effect.f is used to determine the final effectiveness distribution as follows:
- Input to the files are n1p.dat and a1p.dat corresponding to the pressure distributions on the platform surface for nitrogen and air injection respectively.
- A profile.dat file corresponding to the flow passage profile and as obtained from drawing the platform profile using AutoCAD© is also needed for this program to function. This profile simplifies the process of marking the flow passage manually after the effectiveness data has been calculated.
- Running this program will provide the final effectiveness distribution on the platform along with the boundary.
- The final FORTRAN© program called ave_eta.for provides the average chordwise effectiveness distribution for the rotor platform. It is important to note down the pixel number of interest from the output of the previous program for this case. The input data for this program is the effectiveness distribution output file from effect.f.
- Data analysis for PSP measurements is complete once the average chordwise effectiveness is obtained. This effectiveness average and the distribution on the platform are eventually plotted using TECHPLOT® to obtain the final graphs.

Location of all Programs:

MATLAB® =c:\Arun\doe\data2006\gap cooling\2400rpm\analysis with profile\

Or c:\Arun\doe\data2006\gap cooling\2550rpm\analysis with profile\

Or c:\Arun\doe\data2006\gap cooling\3000rpm\analysis with profile\

And in similar folders containing PSP data for hole and combined injection.

FORTRAN© (all the three remaining i.e. aip.f, effect.f and ave_eta.f):
= c:\arun\doe\data2006 \Data-2006\Gap Cooling\Program 4-4-binning\
Or c:\arun\doe\data2006 \Data-2006\hole Cooling\Program\
Or c:\arun\doe\data2006 \Data-2006\gap-hole Cooling\Program\

The location of all the experimental data for PSP programs are listed in the following folders:
c:\Arun\doe\data2006\gap cooling\2400rpm\analysis with profile\
c:\Arun\doe\data2006\gap cooling\2550rpm\analysis with profile\
c:\Arun\doe\data2006\gap cooling\3000rpm\analysis with profile\

The final effectiveness files are named:
Effect.dat for contour plot distribution and average.dat for the chordwise averaged effectiveness.

Sample Experimental data sheet for each step of data acquisition is as follows:
Data output from cal.m, n1p.f or aip.f and effect.f will look like what is shown below. Column 1 and 2 are pixel locations in x and y directions while column 3 is the intensity at each pixel location. Zone j and I correspond to the pixel resolution of the camera during data acquisition.
zone j=60 i=80

1.00	1.00	52.16
2.00	1.00	50.52
3.00	1.00	49.98
4.00	1.00	49.24
5.00	1.00	49.10
6.00	1.00	49.24
7.00	1.00	49.31
8.00	1.00	50.37
9.00	1.00	51.58
10.00	1.00	56.08
11.00	1.00	56.98
12.00	1.00	57.22
13.00	1.00	57.48
14.00	1.00	57.87
15.00	1.00	57.19
16.00	1.00	57.73
17.00	1.00	56.48

```
18.00    1.00        51.53
19.00    1.00        51.87
```

The ave_eta.f output file will look as shown below:

```
ZONE T="Average eta along axial chord"
 0.0000000E+00  0.1748539
 0.0000000E+00  0.1748539
 4.1666668E-02  4.7683168E-02
 4.1666668E-02  4.7683168E-02
 8.3333336E-02  6.2460892E-02
 8.3333336E-02  6.2460892E-02
 0.1250000      7.1295686E-02
 0.1250000      7.1295686E-02
 0.1666667      6.1686646E-02
 0.1666667      6.1686646E-02
 0.2083333      5.3668242E-02
 0.2083333      5.3668242E-02
 0.2500000      4.8669264E-02
 0.2500000      4.8669264E-02
 0.2916667      4.6691611E-02
 0.2916667      4.6691611E-02
 0.3333333      4.0005341E-02
 0.3333333      4.0005341E-02
 0.3750000      3.6817040E-02
 0.3750000      3.6817040E-02
 0.4166667      3.4643199E-02
 0.4166667      3.4643199E-02
 0.4583333      2.6215306E-02
 0.4583333      2.6215306E-02
 0.5000000      2.6122063E-02
 0.5000000      2.6122063E-02
 0.5416667      2.9814955E-02
 0.5416667      2.9814955E-02
 0.5833333      2.1382395E-02
 0.5833333      2.1382395E-02
```

0.6250000	2.0048432E-02
0.6250000	2.0048432E-02
0.6666667	1.9376004E-02
0.6666667	1.9376004E-02
0.7083333	1.5263919E-02
0.7083333	1.5263919E-02
0.7500000	1.0377718E-02
0.7500000	1.0377718E-02
0.7916667	1.5225942E-02
0.7916667	1.5225942E-02
0.8333333	9.9040223E-03
0.8333333	9.9040223E-03
0.8750000	1.2714732E-02
0.8750000	1.2714732E-02
AVERAGE=	4.2231787E-02

where column 1 is the chordwise distance from the blade leading edge to the trailing edge or it can be the length of the area of interest along the axis of the turbine. The 2nd column is the chordwise averaged effectiveness magnitude. This data can be once again plotted using commercially available plotting software like TECHPLOT®.

MATLAB® for image to data conversion (cal.m):

```
clear all
close all

tic

X0 = 1;
Y0 = 1;

W       = 160;
H       = 120;
```

```
Start=1
End=200


'a'
name = 'windon_';
sum=zeros(H,W);


for i = Start:End

   if( ~mod(i,10) )
      fprintf('%d\n',End-i)
   end

   num = sprintf('%04d',i);
   ifile = strcat( name,num,'.tif');

   I = imread( ifile, 'tif' );
   I = I(Y0:Y0+H-1,X0:X0+W-1);
   inten=double(I);
   sum=sum+inten;


end
%%%%% write intensity values to file %%%%%%%%

  ofile = strcat( 'windon.dat');
  fid = fopen(ofile,'w');

  fprintf(fid,'zone j=120 i=160\n');
  for ii = 1:H
    for jj = 1:W
%         ave=ave/(End-Start+1);
```

```
        fprintf(fid, '%6.2f  %6.2f    %12.2f',jj,ii,sum(ii,jj)/(End-Start+1));
%         fprintf(fid, '%12.2f',sum(ii,jj));
        fprintf(fid, '\n');
    end

  end

  fprintf(fid, '\n');
  fclose(fid);

  toc
```

Sample FORTRAN© Programs: PSP

Sample A1P.f

```
          DIMENSION P(200,200)
     OPEN (1,FILE='Black.DAT')
          OPEN (2,FILE='NEWREF.DAT')
          OPEN (3,FILE='a1.DAT')
          open (5,FILE='a1P.dat')
c         open (6,file='air.dat')
c         open (7,file='gas.dat')

          READ(1,*)
          READ(2,*)
          READ(3,*)
c         read(*,*)
c         Calculate Nx and Ny based on binning

          NX=160
          NY=120
```

```
      NCUTOFF=45
c     NCUTOFFMAX=180

      WRITE(5,*) 'ZONE J=',NY,'  I=',NX

      sum=0.0

C     WRITE(*,*) 'OK'
C     READ(*,*)

      DO 100 I=1,NX
      DO 101 J=1,NY
      READ(1,*) A,B,DARK
      READ(2,*) A,B,WINDOFF
      READ(3,*) A,B,WINDON


      IF(WINDON .LE. DARK) THEN
C     WRITE(*,*) 'DIVIDED BY ZERO'
      RI=0.0
   ELSE
      RI=(WINDOFF-dark)/(WINDON-dark)
      ENDIF

      IF(WINDON .LE. NCUTOFF) RI=0.0
      IF((RI.le.0.0).or.(RI.ge.1.0)) then
      RI=0.0
      endif


c     IF(WINDON .GE. NCUTOFFMAX) RI=0.0
c     IF(WINDOFF .GE. 150) RI=0.0
```

```
      a0 =    4.039133056885E-001
      a1 =   -6.030004417414E+000
      a2 =    3.690545577213E+001
      a3 =   -9.699909626772E+001
      a4 =    1.358575746787E+002
      a5 =   -9.588733466192E+001
      a6 =    2.674944804871E+001


      P(I,J)=a0 + a1*ri + a2*ri**2. + ri**3.*a3 + ri**4.*a4
     +       + ri**5.*a5 + ri**6.*a6



c     WRITE(5,*) A,B,P(I,J)
      WRITE(5,*) B,REAL(NX)-A+1.0,P(I,J)

101   CONTINUE
c     WRITE(*,*) I
100   CONTINUE



      CLOSE(5)
      CLOSE(3)
      CLOSE(2)
      CLOSE(1)

      STOP
      END
```

Sample Effect.f

```
      DIMENSION XT(200),YT(200),XB(200),YB(200)
```

```
     +                    ,YSS(200),YBB(200)
      OPEN (1,FILE='a1p.DAT')
            OPEN (2,FILE='n1p.DAT')
            OPEN (3,FILE='PROFILE.DAT')
            open (4,FILE='effect.dat')
            open (5,FILE='Y.dat')


            READ(1,*)
            READ(2,*)
c           read(*,*)

            NX=120
            NY=160

c           PRO1 corresponds to number of points in autocad profile on suction side
c           PRO1 corresponds to number of points in autocad profile on pressure side

            PRO1 = 19
            PRO2 = 14


            WRITE(4,*)'ZONE I=2, J=',PRO1
            C=0.

            READ(3,*)

            DO I=1,PRO1
            READ(3,*) A,B
            XT(I)=A
            YT(I)=B

            WRITE(4,*) A,B,C
            WRITE(4,*) A,B,C
```

```
      ENDDO

c     *************************
c     profiles
      WRITE(4,*)'ZONE I=2, J=',PRO2
      C=0.

      READ(3,*)

      DO I=1,PRO2
      READ(3,*) A,B
      XB(I)=A
      YB(I)=B

      WRITE(4,*) A,B,C
      WRITE(4,*) A,B,C

      ENDDO

c     *************************



      WRITE(4,*) 'ZONE J=',NX,'  I=',NY



      DO I=1,NX
      X=REAL(I)

C     ******* TIP
      DO J=1,PRO1-1
            IF(X.GE.XT(J).AND.X.LE.XT(J+1)) THEN
            YSS(I)=( YT(J+1)-YT(J))/(XT(J+1)-XT(J))*(X-XT(J))+YT(J)
C           WRITE(5,*) X,YSS(I)
            GOTO 1105
```

```
            ENDIF
        ENDDO
1105    CONTINUE




C       ***** BASE LINE

        DO J=1,PRO2-1

            IF(X.GE.XB(J).AND.X.LE.XB(J+1)) THEN
            YBB(I)=( YB(J+1)-YB(J))/(XB(J+1)-XB(J))*(X-XB(J))+YB(J)
C           WRITE(5,*) X,YBB(I)
            GOTO 1106
            ENDIF
        ENDDO
1106    CONTINUE

        ENDDO


        DO 100 I=1,NX
        DO 101 J=1,NY
        READ(1,*) A,B,air
        READ(2,*) A,B,gas
c       WRITE(*,*) 'OK'
c       READ(*,*)

        IF(((AIR .LE. 0.0) .OR. (GAS .LE. 0.0)) .OR. ((AIR .GE. 7.0)
   +     .OR. (GAS .GE. 7.0))) THEN
        EFFECT=-0.1
        ELSE
        effect=abs((air-gas))/air
        ENDIF
```

```
        IF((A .GE. XB(1) .AND. A .LE. XB(PRO2-1)  )
   +.AND. (B .LE. YBB(A) .AND. B .GE. YSS(A)) ) THEN

        WRITE(4,*) A,B,effect
        WRITE(5,*) I,J

        ELSE
        WRITE(4,*) A,B,-0.1
        ENDIF



101   CONTINUE

100   CONTINUE

        CLOSE(4)
        CLOSE(2)
        CLOSE(1)

        STOP
        END
```

Sample ave_eta.for

```
     DIMENSION H(250,250),

    &YSO(250),YSI(250),AX(250),

    &XSMI(250),YSMI(250),XSMO(250),YSMO(250),XPMI(250),YPMI(250),
C    &XPMO(250),YPMO(250),YPO(250),YPI(250),

    &IMSI1(250,250)!, IMSI2(250,250),IMSI3(250,250)
```

```
      OPEN(8,FILE='EFFECT.DAT')
      OPEN(9,FILE='PROFILE.DAT')                    ! BLADE PROFILE

C     OPEN(10,FILE='TEST.DAT')
      OPEN(14,FILE='AVERAGE.DAT')
      OPEN(11,FILE='TEST2.DAT')
c     OPEN(12,FILE='TEST3.DAT')



C     ********** MATERIAL PROPERTIES & OTHER VALUES ***********

      NX=120
      NY=160                  ! SIZE OF INTERESTING REGION
                                      ! ##### MUST BE CHANGED #####

c     XMAX = 98                !UNROTATED MAX PIXEL NO.
c     XMIN = 43                        !UNROTATED MIN PIXEL NO.

      XMAX = 78
      XMIN = 28


C     ************************************************************************

C     ***** READ BLADE PROFILE *****
C     ***** SUCTION SIDE *****



      NPO=19                            !POINTS IN PROFILE - sn. and pr. side
respectively
```

```
      NPB=14

c     NPO=24
c     NPB=29

c     NMAX=46                          !Ending PIXELS No. of profile IN AXIAL CHORD
DIRECTION
c     NMIN=19                          !STARTING PIXEL NO. of profile FOR
AXIAL CHORD

      NMAX=78
      NMIN=28


c     NMAX=98
c     NMIN=43

      NSTEP=1

C     WRITE(10,*)'ZONE i=2, j=',NPO
      C=0

c     suction surface

      READ(9,*)

      DO I=1,NPO
      READ(9,*) A,B

      XSMO(I)=A
      YSMO(I)=B
      X1=A
      Y1=B
C     WRITE(10,*) X1,Y1,C
C     WRITE(10,*) X1,Y1,C
```

```
      ENDDO



      WRITE(10,*)'ZONE i=2, j=',NPB
      C=0
c     pressure surface

      READ(9,*)

      DO I=1,NPB
      READ(9,*) A,B
      XSMI(I)=A
      YSMI(I)=B
      X1=A
      Y1=B
C     WRITE(10,*) X1,Y1,C
C     WRITE(10,*) X1,Y1,C
      ENDDO



      WRITE(10,*)'ZONE i=',NY,', j=',NX

C     ***** READ EFFECTIVENESS *****
      DO I=1,69  ! 113 REPRESENTS THE ROW WHERE THE HEADING FOR DATA IN
            ! EFFECT.DAT STARTS. I.E. ZONE 3 STARTING ROW
            ! ZONE 1 AND 2 FOR PRESSURE AND SUCTION SIDE INFO
                              !CHANGES FOR EVERY DIFFERENT PROFLIE
```

```
c       DO I=1,109
        READ(8,*)
        ENDDO

        DO I=1,NX
        DO J=NY,1,-1
        READ(8,*) A,B,H(I,J)
        X1=A
        Y1=B
C       WRITE(10,*) X1,Y1,H(I,J)
        ENDDO
        ENDDO





C       ***** MAKE BLADE PROFILE ******



        DO I=1,NX


        X=FLOAT(I)




C       ***** PRESSURE OUTSIDE

        DO J=1,NPO-1

                IF(X.GE.XSMO(J).AND.X.LE.XSMO(J+1)) THEN
```

```
                YSO(I)=( YSMO(J+1)-YSMO(J))/(XSMO(J+1)-XSMO(J))*(X-XSMO(J))
   &      +YSMO(J)
C               WRITE(10,*) X,YSO(I),C

                GOTO 1101
                ENDIF
        ENDDO
1101    CONTINUE



C       ***** PRESSURE BOTTOM

        DO J=1,NPB-1

                IF(X.GE.XSMI(J).AND.X.LE.XSMI(J+1)) THEN
                YSI(I)=( YSMI(J+1)-YSMI(J))/(XSMI(J+1)-XSMI(J))*(X-XSMI(J))
   &      +YSMI(J)

C               WRITE(10,*) X,YSI(I)
                GOTO 1102
                ENDIF
        ENDDO
1102    CONTINUE


        ENDDO



        DO I=1,NX
        DO J=1,NY

        IF( (FLOAT(J).GE.(YSO(I))).AND.(FLOAT(J).LE.(YSI(I))) )
```

```
&IMSI1(I,J)=1
                                                    ! IMSI1: PRESSURE SIDE

      ENDDO
      ENDDO


 WRITE(11,*)'ZONE i=',NX,', j=',NY
      DO I=1,NY
      DO J=1,NX
      WRITE(11,*) J,I,IMSI1(J,I)
      ENDDO
      ENDDO



C     ****** ROTATE

C     ****** BLADE PROFILE


      SUMT=0.
      CT=0.


      WRITE(14,*) 'ZONE T="Average eta along axial chord"'

C     UNROTATED AVERAGE - AVERAGE ALONG CHORD

      SUM=0.
      C=0.

      DO I=1,NX
      X=FLOAT(I)
      SUM=0.
```

```
        C=0.
        DO J=1,NY

        IF ( IMSI1(I,J).EQ.1) THEN
        Y=FLOAT(J)
        IF( (H(I,J).GT.0.).AND.(H(I,J).LT.1))THEN
C               WRITE(*,*) X, H(I,J), C
                C=C+1
                SUM=SUM+H(I,J)
        ENDIF

        ENDIF

        ENDDO

        SUMT=SUMT+SUM
        CT=CT+C



    Z=0.
        IF(C.EQ.Z) THEN
        AVE=0.
        GOTO 101
        ENDIF

        AVE=SUM/C
c       WRITE(12,*) X, AVE
101     CONTINUE


        IF (AVE.EQ.Z) GOTO 2101
        IF (X.GT.XMAX) GOTO 2101
```

```
C       WRITE(*,*) X,X1
        XX = (X-NMIN)/FLOAT(NMAX-NMIN)

        WRITE(14,*) XX,AVE

C       XX = (X - XMIN)/(XMAX - XMIN)

        WRITE(14,*) XX,AVE
2101    CONTINUE

        ENDDO




1000    CONTINUE

        AVERAGE=SUMT/CT
        WRITE(*,*) 'AVERAGE=',AVERAGE
        WRITE(14,*) 'AVERAGE=',AVERAGE


        WRITE(*,*) 'PRESS ENTER'
        READ(*,*)




        STOP
        END
```

APPENDIX E

Calibration for TSP uses the same instrument set-up as shown for the PSP calibration but in this case all measurements are performed at atmospheric pressure and with appropriate filters mentioned in the experimental set-up section. A copper specimen previously coated with PSP is now coated with TSP and heated to different pre-set temperatures using an external power supply. Images are captured of the test specimen at these different temperatures and monitored against an accurate T-type thermocouple. A black and a reference image are also captured ~46ºC. Once again like in PSP, the cal.m program is used to average all the images acquired for each temperature and the same procedure is used to plot the ratio of (Iref/I vs T). After plotting this graph, a curve is fit against this calibration data and the function defining the relation between intensities and the temperatures is determined (use TECHPLOT® or TABLECURVE2d® to curve fit).

Experimental data acquisition and processing:

Obtained intensity data from TSP coated surfaces is in *.tif format with a picture resolution dependent on the binning setting on the camera during data acquisition. About 200 images per test case are acquired. This set of data is run though cal.m to obtain an averaged single data file for each test case. The output from this file will have the pixel location in the first column and intensity magnitude in the third column. The file is named windon.dat or can be named anything the user prefers.

Three FORTRAN© programs are further used to process this intensity data to obtain the final heat transfer coefficients. The first program called the temperature.f processes the output file of cal.m. This program contains the TSP calibration data which when applied to the intensity values provides us with the temperature distribution on the platform surface. Also, it is important to remember that for this program to function correctly, the cal.m processed black and the reference image acquired immediately after data was collected is necessary in the same folder as windon.dat. The output of this program (temperature.dat) is also three columned with the third column now containing the temperature distribution on the platform.

The next program “haw with prof.f ” processes temperature.dat and converts temperatures into heat transfer coefficients. The constant.dat file is important for the proper calculation of heat transfer coefficients and the losses associated with conduction and radiation. I should be modified appropriately based on experimental temperatures and physical constants for the heater and insulation material. The ouput of this program again is h.dat file and a sample portion of a large data file is as shown below with the same column sequence as earlier.

```
ZONE I=2, J=   21.00000
  35.06740      107.5594      0.0000000E+00
  35.06740      107.5594      0.0000000E+00
  35.37360      80.10460      0.0000000E+00
  35.37360      80.10460      0.0000000E+00
  38.84440      82.24790      0.0000000E+00
  38.84440      82.24790      0.0000000E+00
  40.98810      83.06440      0.0000000E+00
  40.98810      83.06440      0.0000000E+00
  43.02970      83.88090      0.0000000E+00
  43.02970      83.88090      0.0000000E+00
  44.92230      84.23100      0.0000000E+00
  44.92230      84.23100      0.0000000E+00
  47.01090      84.39130      0.0000000E+00
  47.01090      84.39130      0.0000000E+00
  50.07340      83.88090      0.0000000E+00
  50.07340      83.88090      0.0000000E+00
  53.23790      82.55410      0.0000000E+00
  53.23790      82.55410      0.0000000E+00
  55.48370      81.02320      0.0000000E+00
  55.48370      81.02320      0.0000000E+00
  58.34200      78.67580      0.0000000E+00
  58.34200      78.67580      0.0000000E+00
  60.34460      76.75200      0.0000000E+00
  60.34460      76.75200      0.0000000E+00
  62.89470      73.69120      0.0000000E+00
```

62.89470	73.69120	0.0000000E+00
64.89620	71.03680	0.0000000E+00
64.89620	71.03680	0.0000000E+00
66.90190	67.96610	0.0000000E+00
66.90190	67.96610	0.0000000E+00
69.30510	63.73380	0.0000000E+00
69.30510	63.73380	0.0000000E+00
70.75980	60.92880	0.0000000E+00
70.75980	60.92880	0.0000000E+00
72.08100	57.92060	0.0000000E+00
72.08100	57.92060	0.0000000E+00
73.41310	55.91960	0.0000000E+00
73.41310	55.91960	0.0000000E+00
73.41310	55.91960	0.0000000E+00
73.41310	55.91960	0.0000000E+00
73.86460	83.31340	0.0000000E+00
73.86460	83.31340	0.0000000E+00

ZONE I=2, J= 18.00000

35.06740	107.5594	0.0000000E+00
35.06740	107.5594	0.0000000E+00
39.15060	106.6408	0.0000000E+00
39.15060	106.6408	0.0000000E+00
41.28640	106.4130	0.0000000E+00
41.28640	106.4130	0.0000000E+00
43.79100	105.8296	0.0000000E+00
43.79100	105.8296	0.0000000E+00
46.55490	105.1201	0.0000000E+00
46.55490	105.1201	0.0000000E+00
49.74580	103.9379	0.0000000E+00
49.74580	103.9379	0.0000000E+00
52.55580	102.8233	0.0000000E+00
52.55580	102.8233	0.0000000E+00
54.94530	101.8061	0.0000000E+00
54.94530	101.8061	0.0000000E+00
56.95790	100.8413	0.0000000E+00

56.95790	100.8413	0.0000000E+00
59.14930	99.52400	0.0000000E+00
59.14930	99.52400	0.0000000E+00
61.14580	97.97140	0.0000000E+00
61.14580	97.97140	0.0000000E+00
63.49740	96.19700	0.0000000E+00
63.49740	96.19700	0.0000000E+00
65.67140	94.06770	0.0000000E+00
65.67140	94.06770	0.0000000E+00
67.79170	91.85170	0.0000000E+00
67.79170	91.85170	0.0000000E+00
69.74840	89.60040	0.0000000E+00
69.74840	89.60040	0.0000000E+00
71.84030	86.22270	0.0000000E+00
71.84030	86.22270	0.0000000E+00
73.86460	83.31340	0.0000000E+00
73.86460	83.31340	0.0000000E+00
73.86460	83.31340	0.0000000E+00
73.86460	83.31340	0.0000000E+00
ZONE J=	120 I=	160
1.000000	160.0000	-0.1000000
1.000000	159.0000	-0.1000000
1.000000	158.0000	-0.1000000
1.000000	157.0000	-0.1000000
1.000000	156.0000	-0.1000000
1.000000	155.0000	-0.1000000
1.000000	154.0000	-0.1000000
1.000000	153.0000	-0.1000000
1.000000	152.0000	-0.1000000
1.000000	151.0000	-0.1000000
1.000000	150.0000	-0.1000000
1.000000	149.0000	-0.1000000
1.000000	148.0000	-0.1000000
1.000000	147.0000	-0.1000000
1.000000	146.0000	-0.1000000

1.000000	145.0000	-0.1000000
1.000000	144.0000	-0.1000000
1.000000	143.0000	-0.1000000
1.000000	142.0000	-0.1000000
1.000000	141.0000	-0.1000000
1.000000	140.0000	-0.1000000
1.000000	139.0000	-0.1000000
1.000000	138.0000	-0.1000000
1.000000	137.0000	-0.1000000
1.000000	136.0000	-0.1000000
1.000000	135.0000	-0.1000000
1.000000	134.0000	-0.1000000
1.000000	133.0000	-0.1000000
1.000000	132.0000	-0.1000000
1.000000	131.0000	-0.1000000

ZONE I=2, J=21.00000 and ZONE I=2, J=18.00000 represent the corresponding profile.dat file obtained like earlier from AutoCAD© used in marking the platform boundary. ZONE J=120, I=160 is where the actual data begins.

The next step would be to use ave_eta.f to determine the chordwise heat transfer coefficient exactly like it was explained for PSP.

Location of all Programs:
MATLAB® =c:\Arun\doe Data-2006\TSP\Gap\2400rpm\
Or c:\Arun\doe Data-2006\TSP\Gap\2550rpm\
And in similar folders containing TSP data for hole and combined injection.

FORTRAN© (all the three remaining i.e. aip.f, effect.f and ave_eta.f):
= c:\arun\doe\data2006 \ TSP\Gap\Program 4-4-binning\Temperature
c:\arun\doe\data2006 \ TSP\Gap\Program 4-4-binning\HT with Taw and Profile
c:\arun\doe\data2006 \ TSP\Gap\Program 4-4-binning\average

The location of all the experimental data for TSP programs are listed in the following folders:
c:\Arun\doe\data2006\TSP\gap cooling\2400rpm\

c:\Arun\doe\data2006\gap cooling\2550rpm\

All output data from the MATLAB® and FORTRAN© programs are of the *.dat file form with three columns representing the x, y coordinates of the pixels and the data whether it may be intensities, pressures, effectiveness, temperatures or heat transfer coefficients.

Sample Programs used for analyzing PSP and TSP data and calibration files (in addition to cal.m):

Extra Programs for TSP:

Temperature .f

```
      DIMENSION T(200,200)
  OPEN (1,FILE='Black.DAT')
      OPEN (2,FILE='NEWREF.DAT')
      OPEN (3,FILE='WINDON.DAT')
      open (5,FILE='Temperature.dat')
c     open (6,file='air.dat')
c     open (7,file='gas.dat')

      READ(1,*)
      READ(2,*)
      READ(3,*)
c     read(*,*)
c     Calculate Nx and Ny based on binning

      NX=160
      NY=120

      NCUTOFF=45
c     NCUTOFFMAX=180

      WRITE(5,*) 'ZONE J=',NY,'  I=',NX


C     WRITE(*,*) 'OK'
```

```
C       READ(*,*)

        DO 100 I=1,NX
        DO 101 J=1,NY
        READ(1,*) A,B,BLACK
        READ(2,*) A,B,REFERENCE
        READ(3,*) A,B,WINDON


        IF(WINDON .LE. BLACK) THEN
C       WRITE(*,*) 'DIVIDED BY ZERO'
        RI=0.0
    ELSE
        RI=(WINDON-dark)/(REFERENCE-dark)
        ENDIF

        IF(WINDON .LE. NCUTOFF) RI=0.0
        IF((RI.le.0.0).or.(RI.ge.1.0)) then
        RI=0.0
        endif


        IF(WINDON .LE. NCUTOFF) RI=0.0
c       IF(WINDOFF .GE. 150) RI=0.0


        a0 =    117.51
        a1 =   -125.84
        a2 =    34.005


        T(I,J)=a0 + a1*ri + ri**2.*a2

c       WRITE(5,*) A,B,P(I,J)
        WRITE(5,*) B,REAL(NX)-A+1.0,T(I,J)
```

```
101   CONTINUE
c          WRITE(*,*) I
100   CONTINUE



          CLOSE(5)
          CLOSE(3)
          CLOSE(2)
          CLOSE(1)

          STOP
          END
```

Sample program for heat transfer coefficient calculation:

```
          DIMENSION XT(200),YT(200),XB(200),YB(200)
   +                ,YSS(200),YBB(200)

          open (1,FILE='temperature.DAT')
          open (2,FILE='Tair.DAT')
          open (3,FILE='PROFILE.DAT')
          open (4,FILE='h.dat')
          open (5,FILE='constants.dat')
          open (6,FILE='qnet.dat')
          open (7,FILE='nusselt.dat')
          open (8,FILE='DeltaT.dat')


          READ(1,*)
          READ(2,*)
```

```
      NX=120
      NY=160


c     PRO1 corresponds to number of points in autocad profile on suction side
c     PRO1 corresponds to number of points in autocad profile on pressure side

      PRO1 = 21
      PRO2 = 18

c     Writing profiles in file unit 4 (h.dat)

      WRITE(4,*)'ZONE I=2, J=',PRO1
      C=0.

      READ(3,*)

      DO I=1,PRO1
      READ(3,*) A,B
      XT(I)=A
      YT(I)=B

      WRITE(4,*) A,B,C
      WRITE(4,*) A,B,C

      ENDDO

c     *************************
c     profiles
      WRITE(4,*)'ZONE I=2, J=',PRO2
      C=0.

      READ(3,*)

      DO I=1,PRO2
```

```
      READ(3,*) A,B
      XB(I)=A
      YB(I)=B

      WRITE(4,*) A,B,C
      WRITE(4,*) A,B,C

      ENDDO

c     *************************

      WRITE(4,*) 'ZONE J=',NX,'  I=',NY


      DO I=1,NX
      X=REAL(I)

C     ******* TIP
      DO J=1,PRO1-1
            IF(X.GE.XT(J).AND.X.LE.XT(J+1)) THEN
            YSS(I)=( YT(J+1)-YT(J))/(XT(J+1)-XT(J))*(X-XT(J))+YT(J)
C           WRITE(5,*) X,YSS(I)
            GOTO 1105
            ENDIF
      ENDDO
1105  CONTINUE




C     ***** BASE LINE

      DO J=1,PRO2-1

            IF(X.GE.XB(J).AND.X.LE.XB(J+1)) THEN
```

```
                YBB(I)=( YB(J+1)-YB(J))/(XB(J+1)-XB(J))*(X-XB(J))+YB(J)
C               WRITE(5,*) X,YBB(I)
                GOTO 1106
                ENDIF
        ENDDO
1106    CONTINUE

        ENDDO



        read(5,*)tmainstream
        read(5,*)sso
    read(5,*)Area
        read(5,*)E
        read(5,*)h
        read(5,*)R
        read(5,*)kcon
        read(5,*)th
        read(5,*)ti
    read(5,*)DThb
        read(5,*)DTib
        read(5,*)kh
        read(5,*)ki

        write(*,*)'Enter the voltage in V'
        read(*,*)V
        write(*,*)'Enter the current in A'
        read(*,*)A

    Qfoil=(V*A)/Area



        DO 100 I=1,NX
        DO 101 J=1,NY
```

```
      READ(1,*) A,B,temperature
      READ(2,*) A,B,tair

            Qloss=h*E*(((temperature+273.15)**4)-((tair+273.15)
&           **4))

         Qloss=Qloss+((kh*DThb)/th)+((ki*DTib)/ti)

         Qnet=Qfoil-Qloss

            DeltaT=(temperature-tair)

      If (DeltaT.le.0.0) then

            ht=-0.1
c           nusselt=-0.1

c     goto 102

c           WRITE(8,*) A,B,DeltaT
c           WRITE(7,*) A,B,nusselt
c           WRITE(6,*) A,B,Qfoil,Qloss,Qnet
c           WRITE(4,*) A,B,ht

      else

            ht=Qnet/(DeltaT)

      endif

      If (ht.ge.1000.0) then

            ht=-0.1
c           nusselt=-0.1
```

```
      endif

      IF((A .GE. XB(1) .AND. A .LE. XB(PRO2-1)  )
     +.AND. (B .LE. YBB(A) .AND. B .GE. YSS(A)) ) THEN

      WRITE(8,*) A,B,DeltaT
c     WRITE(7,*) A,B,nusselt
      WRITE(6,*) A,B,Qfoil,Qloss,Qnet
      WRITE(4,*) A,B,ht

      else

      WRITE(4,*) A,B,-0.1

      endif

101   CONTINUE

100   CONTINUE

      CLOSE(8)
      CLOSE(7)
      CLOSE(6)
      CLOSE(5)
      CLOSE(4)
      CLOSE(2)
      CLOSE(1)

      STOP
      END
```

All the above mentioned programs and the corresponding data files (Calibration and Experimental data) can be found in the following folder:
C:\arun\data2006\TSP\

APPENDIX F

Interstage aerodynamic performance was measured along 1st stage rotor exit, 2nd stage stator exit and 2nd stage rotor exit. The flow angles, velocities and pressure were quantified along the radial and circumferential directions. Radial measurements were conducted at the stator-rotor gap plane to determine the effects of rotation on coolant injection through the gap and its spreading on the rotor platform. The results are all tabulated in the following folder along with the data acquisition program.

C:\arun\doe\data2007\

The LabVIEW©© program saves data in a *.dat format and the location of the saved data and the names can be altered as per the user's want in the LabVIEW©© user interface window. The locations of the pressure data from the three 5-hole probes and the monitoring temperatures can also be modified from a window similar to that shown in figure A1 in Appendix A in the LabVIEW©© code. Two programs are used for the purpose of analysing the data recorded by the LabVIEW©© system.

C:\arun\doe\data-2007\fortran1\Newgenesis\genesis.for

C:\arun\doe\data-2007\fortran\final\final.for

The same programs are also available in the C:\arun\doe\ or C:\arun\ folders under the folder name "Original Programs". The section of the original program which has the calibration section needs to be modified every time a probe is calibrated. In this case the following equations were replaced in the original programs and modified to accommodate Bohn's method of analysis. The equations used in calculation of individual velocities, pressures and flow angles are explained in detain in [93].

The first program averages the single data file from the LabVIEW©© code and creates three necessary input files consisting of averaged pressure data from the three 5-hole probes. As a second step, these files are now processed using final.for program after applying the new calibration equations given below, to obtain several output files explained in detail by Thomas Neuenschwander and Jerman Christensen in their report. The output files have all the information regarding the velocities, pressures and flow angles at each of the stations where the measurements were made. The calibration coefficients for each of the probes as

used in the FORTRAN analysis code final.for are as shown below. These equations can be used directly in future codes for the current set of probes as long as the pressure transducers are not re-calibrated.

```
! Calculation of the angles using function AL1 and BET1

AL2     =     AL1(J,Q2,Q1)

BET2    =     BET1(J,Q2,Q1)

Q3      =     CP51(J,AL2,BET2)

Q4      =     CPAVG1(J,AL2,BET2)

Q5      =     CPAVG2(J,AL2,BET2)
```

Probe 1:

```
AL1= -5.512319983759953+x*(-17.11543392651964+
1   x*(-1.298040809491938))+y*(0.2241142175247812)

BET1=-2.718717264745798+x*(0.8199478036058257)+
1         y*(-16.67654041023808+y*(-1.127445921223135))

CP51=1.009104614865544+x*(-0.004425444787712442+
1    x*(-0.0003394569419639734))+
1    y*(-0.003053282360168662+
1    y*(-0.0003218973111682963))

CPAVG1=0.9485927251228654+x*(-0.003568709539507006+
1      x*(-0.0003834157855173904))+
1            y*(0.01658397781341292+y*(-0.0002755939909962648))+
1            x*y*(-9.995698816520405E-05)

CPAVG2=0.7632956623155647+x*(-0.005242099724902170+
1      x*(-0.0003394033373811817))+
```

```
1      y*(-0.03721439331458725+y*(-0.0002293591747291200))
```

Probe 2:

```
AL1 = -8.188964057650064+x*(-13.78914194278253+
1            x*(0.6145039055028483+x*(0.4689422285801132+
1            x*(-0.3080744206055622+x*(-0.1496309643057025)))))
1          +y*(-0.5005278751038056+y*(-0.1334792991511408))

BET1=0.1997811942435538+x*(0.4691401072615720)+
1   y*(-13.16462897329833+
1   y*(-0.06375826157095292+y*(0.6503498150902935)))

CP51 =1.015220101196470+x*(-0.005323243460482455+
1     x*(-0.0003385301154613443))+
1     y*(-0.0002656617149876935+
1     y*(-0.0003330521625932724))

CPAVG1=0.9598539427228956+x*(-0.004098652968853929+
1            x*(-0.0003609428462679500))+
1            y*(0.03711967828031742+y*(-0.0001664334884193794))+
1            x*y*(-0.0002348891720108321)

CPAVG2=0.9576666607755363+x*(-0.008614741621418281+
1      x*(-0.0003622218616282675+x*(5.869469631430000E-06)))+
1      y*(-0.03926906810323694+y*(-0.0002081335300061541+
1            y*(-5.663869765284229E-07)))+x*y*(0.0002219286244152836+y*
1      (4.032837222616043E-06)+x*(1.978757358982856E-05))
```

Probe 4:

```
AL1 = -6.379411169456789+x*(-14.85942703259849)+
1          y*(0.7667061209486384)

BET1=-5.165865108394477+x*(-0.1645089917806040)+
```

```
1   y*(-18.13056021310048)

CP51=1.015735341870901+x*(-0.003748683124218612+
1     x*(-0.0003713739136215536))+
1     y*(-0.004256964676743704+
1     y*(-0.0003710276222985216))

CPAVG1=0.8985706469162790+x*(-0.002372043221930672+
1             x*(-0.0003309886202759218))+
1      y*(0.01305761922434033+y*(-0.0003332929596081366))+
1             x*y*(-7.036558380246632E-05)

CPAVG2=0.6142847441978816+x*(-0.0004840503546749991+
1             x*(-0.0002170332396303335))+y*(-0.03318508289987696)
```

These equations are representative of the five functions used by Rubner and Bohn to determine the interstage flow parameters. For more information, read the aerodynamic section in this dissertation or the original paper itself. CP51, CPAVG1 and CPAVG2 are Q3, Q4 and Q5 coefficients defined by Bohn. The probes were calibrated twice each. The equations as entered in the fortran© code form is from one set while the graphs are from the second set. Both are accurate and either one can be used to eventually analyze data. Samples of both are given for the sake of clarity and as a demonstration.

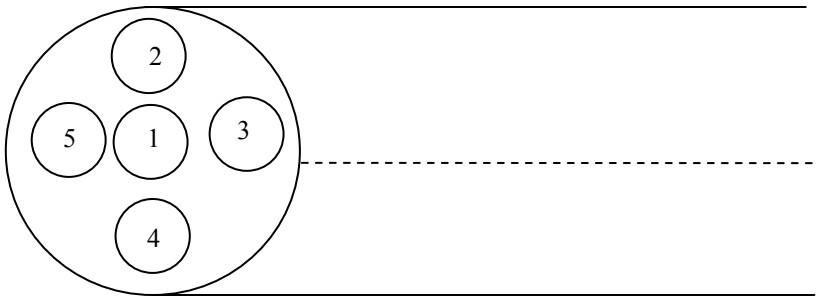

Fig F1: Hole Configuration of the 5-Hole Pitot Probes.

APPENDIX G

Sample Kline McClintock Uncertainty Analysis for uncertainty analysis of 5-hole probe calibration and data analysis:

$Pamb := 102000$

$input := READPRN("probe1.txt")$ - Input calibration file here, i.e have the calibration file in the same folder as the program.

$T := 23.5 + 273$

$pitch := input\langle 1 \rangle$

$yaw := input\langle 2 \rangle$

$P1 := input\langle 3 \rangle$

$P2 := input\langle 4 \rangle$

$P3 := input\langle 5 \rangle$

$P4 := input\langle 6 \rangle$

$P5 := input\langle 7 \rangle$

$Pstat := input\langle 8 \rangle$

$Ptot := input\langle 10 \rangle$

$n := 1 .. 2601$

$$Q1_n := \frac{\left(P3_n - P2_n\right)}{\left(P1_n - Pstat_n\right)}$$

$$Q2_n := \frac{\left(P5_n - P4_n\right)}{\left(P1_n - Pstat_n\right)}$$

$$Q3_n := \frac{\left(P1_n - Pstat_n\right)}{\left(Ptot_n - Pstat_n\right)}$$

$$Q4_n := \frac{\left(P1_n - P3_n\right)}{\left(Ptot_n - Pstat_n\right)}$$

$$Q5_n := \frac{\left(P1_n - P2_n\right)}{\left(Ptot_n - Pstat_n\right)}$$

From the collected calibration points

$$x_n := Q1_n$$

$$y_n := Q2_n$$

$$z_n := -5.5124 + -17.115 x_n + -1.3 \cdot \left(x_n\right)^2 + 0.224 \left(y_n\right)$$

$$pitchcalc_n := z_n$$

From the collected calibration points

$$x_n := Q1_n$$

$$y_n := Q2_n$$

$$z_n := -2.719 + 0.82 \cdot x_n + -16.677 \cdot y_n + -1.127 \cdot \left(y_n\right)^2$$

$$yawcalc_n := z_n$$

$$x_n := Q1_n$$

$$y_n := Q2_n$$

$$z_n := 1.009 - 0.004 x_n + \left(0.0003 x_n\right) - 0.003 \cdot y_n - 0.0003 \left(y_n\right)^2$$

$$Q3_n := z_n$$

$$z_n := \left[\left(0.94860 - 0.004 x_n\right) - 0.0004 \left(x_n\right)^2 + 0.0166 y_n\right] - 0.0003 \left(y_n\right)^2 + 9.9956 \left(y_n\right) \cdot \left(x_n\right)$$

$Q4_n := z_n$

$$Pstatcalc_n := \frac{Q3_n \cdot Q4_n - Q4_n \cdot P1_n}{Q3_n - Q4_n}$$

$$Ptotcalc_n := \left(\frac{P1_n - Pstatcalc_n}{Q3_n} \right) + Pstatcalc_n$$

$$pitcherror_n := \frac{\left| pitchcalc_n - pitch_n \right|}{pitchcalc_n} \cdot 10($$

$$yawerror_n := \frac{\left| yawcalc_n - yaw_n \right|}{\left| yawcalc_n \right|}$$

$$Ptoterror_n := \left| \frac{Ptotcalc_n - Ptot_n}{Ptot_n} \right| \cdot 10($$

$$Pstaterror_n := \left| \frac{Pstatcalc_n - Pstat_n}{Pstat_n} \right| \cdot 10($$

$pitchdiff_n := pitchcalc_n - pitch_n$

$yawdiff_n := yawcalc_n - yaw_n$

comp1 := augment(pitch, yaw, pitchdiff)

comp2 := augment(pitch, yaw, yawdiff)

WRITEPRN("compare1.dat") := comp1

WRITEPRN("compare2.dat") := comp2

Uncertainty in measurements:

wT := 0.5

R := 287.1

wP := 1

$$\rho := \frac{Pamb}{R \cdot T}$$

$\rho = 1.198$

$$d\rho dT := \frac{Pamb}{\left(R \cdot T^2\right)}$$

$$d\rho dPamb := \frac{1}{\left(R \cdot T^2\right)}$$

$$w\rho := \sqrt{d\rho dT^2 + d\rho dPamb^2}$$

$w\rho = 4.041 \times 10^{-3}$

$$\%\rho := \frac{w\rho}{\rho} \cdot 10$$

$\%\rho = 0.337$

$$V := \sqrt{2\frac{(Ptot - Pstat)}{\rho}}$$

$$wCpalpha_n := \left[\left[wP\left(\frac{1}{P1_n - Pstat_n}\right)\right]^2 + \left[wP\left(\frac{-1}{P1_n - Pstat_n}\right)\right]^2 + \left[-wP\frac{\left(P4_n - P5_n\right)}{\left(P1_n - Pstat_n\right)^2}\right]^2 + \left[wP\frac{\left(P4_n - P5_n\right)}{\left(P1_n - Pstat_n\right)^2}\right]^2\right]^{0.5}$$

$$wCpbeta_n := \left[\left[wP\left(\frac{1}{P1_n - Pstat_n}\right)\right]^2 + \left[wP\left(\frac{-1}{P1_n - Pstat_n}\right)\right]^2 + \left[-wP\frac{\left(P2_n - P3_n\right)}{\left(P1_n - Pstat_n\right)^2}\right]^2 + \left[wP\frac{\left(P2_n - P3_n\right)}{\left(P1_n - Pstat_n\right)^2}\right]^2\right]^{0.5}$$

$Cpalpha_n := Q3_n$

$$\%Cpalpha_n := \frac{wCpalpha_n}{Cpalpha_n} \cdot 10$$

$Cpbeta_n := Q4_n$

$$\%Cpbeta_n := \frac{wCpbeta_n}{Cpbeta_n} \cdot 10$$

Thus uncertainties for each of the flow parameters like alpha, beta the velocities and the pressures can be calculated using the Mathcad© code shown above.

APPENDIX H

Table H1: Rotor platform film cooling hole orientation.

	D,mm	β º	θ º
Hole 1	1.00	35º	47.39º
Hole 2	1.00	35º	34.50º
Hole 3	1.00	35º	25.31º
Hole 4	1.00	35º	49.58º
Hole 5	1.00	35º	42.29º
Hole 6	1.00	35º	32.62º
Hole 7	1.00	37º	57.46º
Hole 8	1.00	37º	40.25º
Hole 9	1.00	37º	33.83º

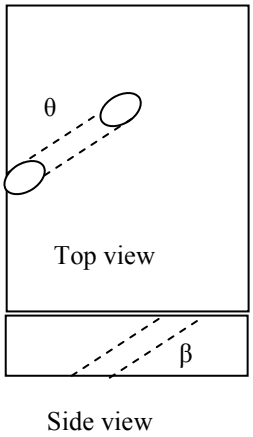

VITA

Arun Suryanarayanan was born in Madurai, Tamil Nadu, India. He attended primary and high school at Poorna Prajna Education Center, Bangalore, Karnataka, India. He attended Vijaya College, Basavangudi, between 1992 and 1994, for his pre-university education. He completed his undergraduate education in mechanical engineering at Bangalore University in 1998 receiving a B.E. He obtained his master's degree in mechanical engineering under the supervision of Dr. Gerald Morrison at Texas A&M University in 2003. He received his doctorate of Philosophy degree in mechanical engineering from Texas A&M University in 2009. He may be reached at: Texas A&M University, Department of Mechanical Engineering, 3123 TAMU, College Station, TX-77843-3123